Probing the Earth Matter Density Through INO-ICAL and Related Detector Development

By

Rajesh Ganai

Enrollment No. PHYS01201004015

Bhabha Atomic Research Centre, Mumbai

A thesis submitted to

The Board of Studies in Physical Sciences

In partial fulfillment of requirements for the Degree of

DOCTOR OF PHILOSOPHY

of

HOMI BHABHA NATIONAL INSTITUTE
Bhabha Atomic Research Centre
Mumbai-400085, India

January, 2017

Homi Bhabha National Institute[1]

Recommendations of the Viva Voce Committee

As members of the Viva Voce Committee, we certify that we have read the dissertation prepared by **Mr. Rajesh Ganai** entitled "**Probing the Earth Matter Density Through INO-ICAL and Related Detector Development**" and recommend that it may be accepted as fulfilling the thesis requirement for the award of Degree of Doctor of Philosophy.

Chairman - Dr. S. R. Banerjee	**Date:** 12/5/2017
Guide / Convener - Dr. S. Chattopadhyay	**Date:** 12/5/17
Examiner – Dr. B. Satyanarayana	**Date:** 12/5/17
Member 1- Dr. L. M. Pant	**Date:** 2/6/17
Member 2- Dr. S. Saha	**Date:** 12/5/2017

Final approval and acceptance of this thesis is contingent upon the candidate's submission of the final copies of the thesis to HBNI.

I/We hereby certify that I/we have read this thesis prepared under my/our direction and recommend that it may be accepted as fulfilling the thesis requirement.

Date: 12/5/17

Place: VECC-KOLKATA

Signature

Guide

[1] This page is to be included only for final submission after successful completion of viva voce.

STATEMENT BY AUTHOR

This dissertation has been submitted in partial fulfillment of requirements for an advanced degree at Homi Bhabha National Institute (HBNI) and is deposited in the Library to be made available to borrowers under rules of the HBNI.

Brief quotations from this dissertation are allowable without special permission, provided that accurate acknowledgement of the source is made. Requests for permission for extended quotation from or reproduction of this manuscript in whole or in part may be granted by the Competent Authority of HBNI, when, in his or her judgment, the proposed use of the material is in the interests of scholarship. In all other instances, however, permission must be obtained from the author.

Rajesh Ganai

DECLARATION

I, hereby declare that the investigation presented in the thesis has been carried out by me. The work is original and has not been submitted earlier as a whole or in part for a degree/diploma at this or any other Institution/University.

Rajesh Ganai

List of Publications arising from the thesis

In peer-reviewed Journal

1. *"Fabrication and Characterization of Oil-Free Large High Pressure Laminate Resistive Plate Chamber"*
   Rajesh Ganai, A. Roy, K. Agarwal , Z. Ahammed, S. Choudhury and S. Chattopadhyay.
   Journal of Instrumentation, (2016 JINST 11 P04026).
   DOI 10.1088/1748-0221/11/04/P04026

2. *"Long Term Performance Studies of Large Oil-Free Bakelite Resistive Plate Chamber"*
   Rajesh Ganai, A. Roy, M. K. Shiroya, K. Agarwal , Z. Ahammed, S. Choudhury and S. Chattopadhyay.
   Journal of Instrumentation, (2016 JINST 11 C09010).
   DOI 10.1088/1748-0221/11/09/C09010

Conferences and Symposia

1. *"Development of RPC using glued bakelite sheets"*
   Viwek Mertiya, **Rajesh Ganai**, S. Biswas, S. Chattopadhyay, G. Das, C. Marick, S. Saha and Y. P. Viyogi.
   Proceedings of the DAE Symp. on Nucl. Phys. 58 (2013)
   Bhabha Atomic Research Centre, Mumbai

2. *"Development and Characterization of Bakelite RPC"*
   Rajesh Ganai, K. Agarwal , B. N. Muduli, S. Chattopadhyay and Z. Ahammed.
   Proceedings of the DAE Symp. on Nucl. Phys. 59 (2014)
   Banaras Hindu University, Varanasi

3. *"Fabrication and Characterization of Large Size Bakelite Resistive Plate Chamber"*
   Rajesh Ganai, Arindam Roy, Kshitij Agarwal, Zubayer Ahammed and Subhasis Chattopadhyay
   Proceedings of the DAE Symp. on Nucl. Phys. 60 (2015)
   Sri Sathya Sai Institute of Higher Learning, Prasanthi Nilayam-515134, AP, India

4. *"Study of Electrical Properties of Glue Used in Fabrication of Large Bakelite Resistive Plate Chamber"*
   Rajesh Ganai, Arindam Roy, Kshitij Agarwal, Zubayer Ahammed and Subhasis Chattopadhyay
   Proceedings of the DAE Symp. on Nucl. Phys. 60 (2015)
   Sri Sathya Sai Institute of Higher Learning, Prasanthi Nilayam-515134, AP, India

5. *"Study of Performance of Bakelite Resistive Plate Chamber (RPC)"*
   Rajesh Ganai, A. Roy, K. Agarwal , B. N. Muduli, S. Chattopadhyay, Z. Ahammed, G. Das and S. Ramnarayan.
   Springer Proceedings in Physics 174 (2016)
   Indian Institute of Technology, Guwahati, India

6. *"Characterization of Prototype Oil-free Bakelite RPC for High Rate Experiments"*
   M.Mondal, **Rajesh Ganai**, Zubayer Ahmmed and Subhasis Chattopadhyay.
   Proceedings of the DAE Symp. on Nucl. Phys. 61 (2016)
   Saha Institute of Nuclear Physics, Kolkata, India.

7. *"Development of 5-gap Glass Multi-gap Resistive Plate Chamber for Time of Flight Positron Emission Tomography TOF-PET Imaging"*
   Rajesh Ganai, A. Roy, S. Mehta, M. Mondal, Zubayer Ahmmed and Subhasis Chattopadhyay.
   Proceedings of the DAE Symp. on Nucl. Phys. 61 (2016)
   Saha Institute of Nuclear Physics, Kolkata, India.

8. *"Preliminary Test of 5-gap Glass Multi-gap Resistive Plate Chamber for Photon Detection for Time of Flight Positron Emission Tomography TOF-PET Imaging"*
   Rajesh Ganai, M. Mondal, S. Mehta and Subhasis Chattopadhyay.
   Proceedings of the DAE Symp. on Nucl. Phys. 61 (2016)
   Saha Institute of Nuclear Physics, Kolkata, India.

9. *"Feasibility Study of Using RPCs in CBM Muon Chamber"*
   E. Nandy, M. Mondal, **Rajesh Ganai**, Z. Ahammed and Subhasis Chattopadhyay.
   Proceedings of the DAE Symp. on Nucl. Phys. 61 (2016)
   Saha Institute of Nuclear Physics, Kolkata, India.

Rajesh Ganai

Acknowledgement

I express my heartful gratitude and pleasure towards my supervisor, Prof. Subhasis Chattopadhyay for his excellent supervision, training and constant motivation. I thank you Sir, for your patience, enthusiasm and encouragement and being my source of motivation. I have been fortunate to have you as my supervisor. I am very much thankful to Prof. Amitava Raychaudhuri for guiding me in my work. I am thankful for your valuable guidance, suggestions and comments.

I would like to thank my doctoral committee members, Prof. S. R. Banerjee, Prof. Satyajit Saha and Prof. L. M. Pant for their insightful comments, timely advice and encouragement. It is my immense pleasure to have such a supportive committee overseeing my work and guiding me through.

I am thankful to Prof. Naba Kumar Mondal and Dr. B. Satyanarayana for your encouragement, guidance and support. I am thankful to my teachers in the phd courses, Prof. S. Uma Shankar, V. Nanal, Prof. V. M. Datar, Prof. M. Guchait, Prof. Gagan Mohanty, Prof. G. Majumder, Mr. S. S. Upadhya for offering beautiful insights of various fields. I have no words to thank Mr. P. Nagraj, Mr. P. Verma, Mr. S. Joshi, Dr. D. Samuel, Dr. Tarak Thakore, Dr. Kolahal Bhattacharaya, Mr. L.V Reddy, Mr. M. Saraf, Mr. M. Bhuyan, Mr. S. Lahamge, Ms. A. Redij, Ms. N. Srivastava, Mr. V. Asgolkar, Mr. S. Chavan and Mr. G. Ghodke for their support during my stay at TIFR, Mumbai. A very very special thanks to Mr. R. R. Shinde for teaching me about RPCs and electronics and guiding me through my course work and my PhD. I thank you for your valuable suggestions.

I am very much thankful to INO Graduate Training Program for providing me with such a nice opportunity. A heartfelt thanks to all the members of the INO collaboration. I thank my fellow INO colleagues, Raveendra, Varchaswi, Moon Moon, Animesh, Mathimalar, Neha, Meghna, Thirunavukarasu, Maulik, Lakshmi, Salim Bhai, Nitali di, Sumanta da, Vivek da, Sudeshna di, Anushree di, Ali, Abhik, Deepak, Chandan, Amina, Apoorva for their dynamic, comfortable and enthusiastic company.

My stay at VECC, Kolkata for my entire PhD work has been very memorable. I would like to thank Director, VECC to provide me with the opportunity to work here. It is my pleasure to thank Prof. Y. P. Viyogi to encourage me during my stay in VECC. Sir, your kind words and suggesions will always be there with me. I am very much indebted to Mr. Ganesh Das who always helped me in my detector development work. I am thankful to Jayant Ji, Nilima di, Nabarun da, Santu da, Bapari da, Sukumar da, Khokan das, Tirthankar da, Anjan da, Kamal da Sr., Sanat da, Bhaskar da for their help time to time.

My heartfelt thanks to Mr. S. Ramnarayan and Dr. Zubayer Ahammed for their valuable time, immense patience and his constant motivation and encouragement. I am grateful to

Prof. Tapan K. Nayak, Dr. Susanta Pal, Dr. Anand K. Dubey, Dr. Prithwish Tribedy, Dr. Partha Pratim Bhaduri, Dr. Sanjib Muhuri, Dr. Premomoy Ghosh, Mr. Jogendra Saini, Mr. Partha Bhaskar and Mr. Vikas Singhal for teaching me and for their valuable suggestions and discussions. My special thanks to Saikat da, Arnab da and Sanjay da for their constant encouragement, suggestions and comments. You were always around me as elder brothers. I would like to thank Mitali, Rajendra, Arghya, Debojit and all my seniors and juniors in VECC for their wonderful company during my PhD in and out of laboratory. I thank all my past and present lab mates - Kshitij, Biranchi, Ekata, Shaifali, Vivek ji, Mehul, Ritesh, Karimul, Nazibul, Sumina and Mitali. Special thanks to Kshitij, Mehul and Shaifali for your constant help, questions and discussions which helped to develop my knowledge. I acknowledge the computing facility of TIFR and grid-peer Kolkata at VECC.

I thank my post graduate friends Jayaprasath, Venkat, Ambuj, Joshya, Kani, Hemlin, Bhaskar, Prabhakar and Thiru. My friends from under-graduate (F.A.L.T.U - 15 members) are one of the most important members in my life. You guys have been my constant motivation. I would also like to thank my school friends. Thank you all.

I am highly indebted to my school teachers, my under-graduate teachers and post-graduate teachers. Without you I would not have come this far. Thank you sirs and madams. I express my regards and owe my gratitude to Dr. Alok Sharan and Dr. S. V. M. Satyanarayana. It's your teaching, encouragement and guidance that I started my carrer as a researcher. Thank you sirs.

I would like to acknowledge the financial and technical support of INO, DAE and DST without which my PhD. was not possible. Thanks to all the non-academic staff of VECC, TIFR and INO who are giving their best.

I do not know how to thank Basu Sumit, Choudhury Subikash, Dey Balaram and Roy Arindam. You guys have always been there specially during my hard times. You have always supported me emotionally, financially and in many other ways whenever I needed. Please always be there just like the way you always have been. Thanks to Silver Sands.

Last but not the least, I would like to thank my family, my parents (Mr. Ananda Gopal Ganai and Mrs. Anuradha Ganai), my in-laws(Mr. Rabindra Nath Das, Mrs. Sumitra Das and Mr. Pranay Das) for their unconditional support, love and encouragement. Thanks to my little brother, Arijit Ganai and elder sister Mrs Rina Kundu. Special thanks to my late grandfather Shri Balaram Ganai because of whom I am writing my thesis. Many many thanks to my grandmother (Mrs. Kalyani Ganai) and uncle (Mr. Dilip Ganai) for their love and support.

I have no words to thank my wife Mrs. Lopamudra Das. You always have been with me knowing that I am not an easy guy to be with. Your love, care, inspirational words and smile have always kept me going irrespective of our hard times. Your belief in me have always motivated me.

Thank you everybody for all your help and support on and off the court.

Contents

Chapter 1

Synopsis

Neutrino is an elementary particle proposed by Wolfgang Pauli in 1930 to explain β-decay. Since then studying the properties of neutrinos has been exciting in the field of particle physics. Neutrinos are the second most abundant particles in our universe after photons. Several experiments have given us interesting insights about these particles like a) they come in three flavours, even though it was predicted by Standard Model that they are massless, b) they oscillate during the course of their travel which implies that they are not massless, and so on. But at the same time many questions remain unanswered and many more emerged like, a) what are their exact masses, b) are they Dirac or Majorana particles, c) what can they say about the physics beyond Standard Model, d) can they explain the matter-antimatter asymmetry, e) are there sterile neutrinos and many more. In the context to these unanswered and open problems, India has taken an initiative to answer a few questions like (i) how the masses of neutrinos are arranged (ii) are they Dirac or Majorana particles (iii) are there sterile neutrinos (iv) are there Non Standard Interactions (NSI) in neutrino oscillations etc. This initiative has given birth to the India based Neutrino Observatory (INO). INO will be a multi-institutional underground neutrino laboratory which will accommodate several experiments like Iron CALorimeter (ICAL), Neutrino-less Double Beta Decay (NDBD) and Dark matter searches at INO (DINO). INO will be built within a large underground cavern with $\sim$1 km or more rock overburden situated under Bodi West Hills

near Pottipuram village, 110 km away from the city of Madurai,in Theni district of Tamil Nadu in Southern India. This thesis aims at the development of a detector proposed to be used in INO-ICAL experiment and a few physics aspects to be addressed by INO-ICAL.
The work done in this thesis can be divided into two broad categories as follows:-

- Development of large size Resistive Plate Chamber for the Iron Calorimeter (ICAL) in the India based Neutrino Observatory (INO)

  A large size (240 cm $\times$ 120 cm $\times$ 0.2 cm) oil-free single gap bakelite Resistive Plate Chamber (RPC) has been developed for INO-ICAL to detect muons for studying the oscillations of atmospheric neutrinos and characterized with cosmic rays. As a part of the R&D programme, several small size single gap and multi-gap resistive plate chambers have also been developed.

- Probing the earth matter density through INO-ICAL

  INO-ICAL has a unique feature that it can also be used to probe the matter density profile, especially that of the core of the earth, as the amount of oscillation depends on the matter density that the atmospheric neutrinos pass through. Studying the oscillation parameters of atmospheric neutrinos in INO-ICAL will help to scan the density profile of the earth's core. In this thesis, A model based study to estimate the sensitivity of INO-ICAL to this profiling has been done.

1.1 Probing The Earth-Matter Density Through INO-ICAL.

We have made use of widely used models to study the sensitivity of INO-ICAL to the density of the core of the earth. The models used are, a neutrino generator (GENIE), atmospheric neutrino flux (HONDA flux) at Theni, Southern India and ICAL detector response using GEANT4. The

neutrino oscillation has been used as the tool to profile the density of the core of the earth. During the course of their travel, neutrinos oscillate from one flavour to another. The probability of their oscillation gets enhanced when a neutrino passes through matter. As the neutrinos are weakly interacting, the whole earth is nearly transparent to them. Since the core of the earth is highly dense, the magnitude of oscillation of the neutrinos or anti-neutrinos passing through the core is higher than that of those passing through the mantle or the crust of the earth. Also the up-coming neutrinos or anti-neutrinos passing through the core oscillate more than that of down-going neutrinos or anti-neutrinos as the up-coming ones travel larger distance than that of down-going ones. With the help of RPCs as active detectors and magnetized iron plates for bending the muons produced by neutrinos interacting with these iron plates, INO-ICAL can distinguish between up-coming and down-going neutrinos (anti-neutrinos). The energy of a neutrino is obtained with the help of bending of the muon produced by the neutrino interaction with iron plates in INO-ICAL.

In this work, the variation of the ratio of the number of up-coming neutrinos to the number of down-going neutrinos at a particular time interval v/s "L/E", where "L" is the distance traveled by the neutrinos and "E" is the energy of the corresponding neutrinos, has been used as a tool. The final number of neutrinos, corrected for the response function of the ICAL was obtained by GEANT simulation. This variation gives us several "dips". The locations and values of these dips have been found to be sensitive to the neutrino oscillation parameters which are again sensitive to the density of matter through which the neutrinos pass. A comparison of the locations and strengths of these "dips" by tuning the density of the core of the earth while keeping the six oscillation parameters fixed, helps us in profiling the density of the core of the earth. From the comparison it has been seen that INO-ICAL is sensitive to $\geq$5% change in the density of the core of the earth from the Preliminary Reference Earth Model (PREM).

1.2 Development Of Resistive Plate Chambers (RPCs) For Neutrino Experiments

INO-ICAL[2] of dimension $\sim$ 48 m $\times$ 16 m $\times$ 14 m will consist of $\sim$ 50 kT magnetized iron plates stacked in 151 layers. About 30,000 single gap RPC[1] modules each of dimension $\sim$ 200 cm $\times$ 200 cm $\times$ 0.2 cm sandwiched between 151 layers of iron plates will be used as tracking layers. RPCs, because of very good time resolution, will be capable of differentiating between up and down going neutrinos in INO-ICAL. The RPC modules to be used in Deep Underground Neutrino Experiment (DUNE)[3] at Fermilab, USA, are of dimension 200 cm $\times$ 100 cm $\times$ 0.2 cm.

As a part of this programme, Variable Energy Cyclotron Centre, Kolkata, India, has been actively taking part in the development of large size (240 cm $\times$ 120 cm) RPCs using High Pressure paper Laminates (HPL), commonly referred as bakelite, that has been proposed to be used in INO-ICAL or in the Near Detector (ND) of DUNE. As a part of the detector R&D, a large size single gap oil-free bakelite RPC has been developed. Various grades of bakelites procured from the local market have been tested for their suitability to build RPCs. A small (30 cm $\times$ 30 cm) RPC was built using the selected suitable grade bakelite and the chamber has been successfully tested using cosmic rays. The successful results of 30 cm $\times$ 30 cm RPC encouraged us to develop a large size RPC module with same grade material.

My thesis deals with the material characterization, fabrication and testing of the small and large modules. In this work, unlike standard procedure of using oil for smoothening the electrode surface, we have used oil-free electrodes, thereby eliminating a major fabrication step.

1.2.1 Fabrication and testing of a small (30 cm $\times$ 30 cm $\times$ 0.2 cm) oil free bakelite RPC

A single gap (30 cm $\times$ 30 cm $\times$ 0.2 cm) bakelite RPC using 0.3 cm thick bakelite electrodes has been fabricated. The bakelite sheets were procured from Indian bakelite industry. A gap

of 0.2 cm was maintained between these electrodes with the help of 4 button spacers, each of diameter 1 cm and height 0.2 cm and 4 side spacers each of length 28 cm and height of 0.2 cm. Two gas nozzles have been used in the module. The outer surfaces of both the electrodes were painted with conducting graphite paint mixed with a special thinner in 1:1 ratio in order to apply uniform electric field across the plates. The RPC has been tested with cosmic rays in a standard cosmic ray test set-up. We have used three plastic scintillators - two paddle scintillators (20 cm × 8.5 cm) and one finger scintillator (7 cm × 1.5 cm). The overlap area between the scintillators has been used to obtain the cosmic ray efficiency for a particular set-up. Various detector parameters like I-V characteristics, leakage current stability, efficiency, noise rate have also been measured. An efficiency plateau was obtained beyond total applied high voltage of

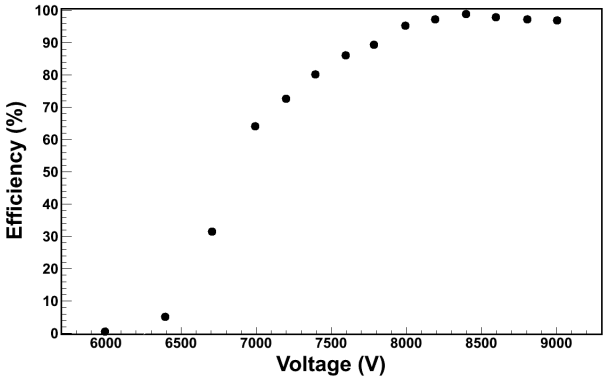

Figure 1.1: [Colour online] Variation of efficiency with applied high voltage of the small bakelite RPC module.

8000 V. The efficiency, as shown in Figure 1.1 was found to be ∼98% whereas the noise rate was found to be ∼1.7 Hz/cm^2 at 9000 V. A linearly varying behaviour of the noise rate with the applied voltage is shown in Figure 1.2.

With the successful development of small size (30 cm × 30 cm × 0.2 cm) bakelite RPC, we have also developed a large size (240 cm × 120 cm × 0.2 cm) bakelite RPC.

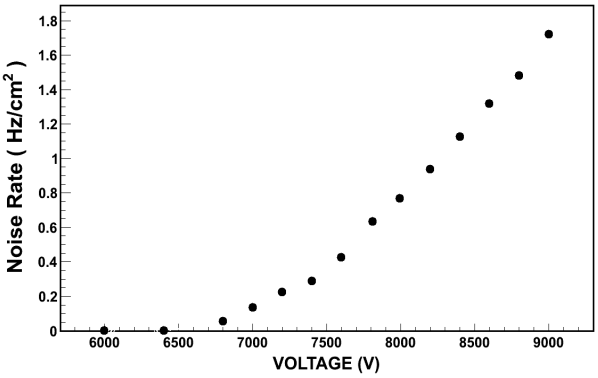

Figure 1.2: [Colour online] Variation of noise rate of the fabricated the bakelite RPC with applied high voltage.

1.2.2 Fabrication and testing of a large size (240 cm × 120 cm × 0.2 cm oil free bakelite RPC

For the fabrication of the large area RPC, we have followed the standard procedure of RPC fabrication. Figure 1.3 shows the photograph of the complete RPC and Figure 1.4 shows the complete RPC with the pick-up panels on it. Each pick-up panels are made of ∼(125 cm × 105

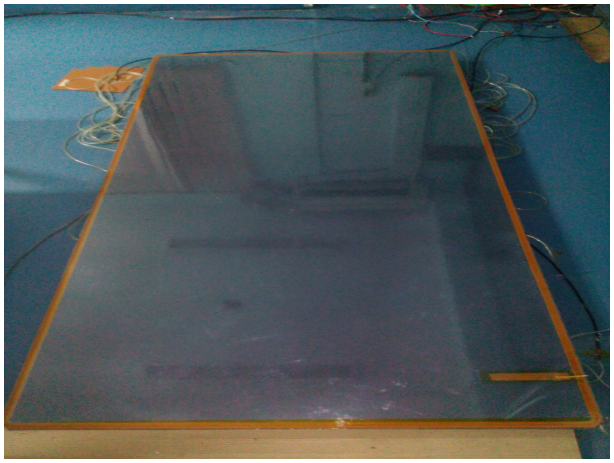

Figure 1.3: [Colour online] Photograph of the large bakelite RPC.

cm × 0.15 cm) FR4 sheet sandwiched between ∼(125 cm × 105 cm × 0.0035 cm) copper sheets. The copper pick-up strips are 2.5 cm in width, with a gap of 0.2 cm between adjacent strips. During fabrication, special care has been taken to ensure good planarity of the electrodes.

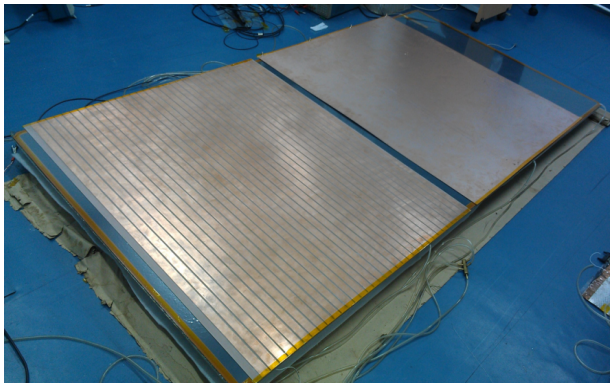

Figure 1.4: [Colour online] Photograph of the large bakelite RPC with pick-up panel.

We have studied the efficiency and noise rate of the chamber at a signal threshold of -20 mV. Figure 1.5 shows the variation of efficiency with the total applied voltage showing a plateau of >95% above 8400 V. The variation of efficiency, temperature and relative humidity during the testing period is shown in Figure 1.6. The noise rate variation as a function of the applied voltage is shown in Figure 1.7. During this test, the noise rate of the RPC has been found to be ∼0.75 Hz/cm^2 at 9000 V. Efficiency of the chamber has been measured at 16 different

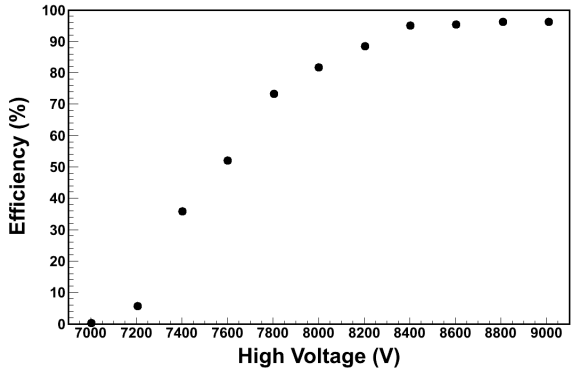

Figure 1.5: *Efficiency of the chamber as a function of the applied voltage. The error bars are within the marker size.*

locations of the detector at 9000 V, eight at the edges of the RPC and eight away from the edges. Figure 1.8 shows these locations over the RPC surface along with the measured efficiency values and Figure 1.9 shows the distribution of efficiency measured at these locations. The

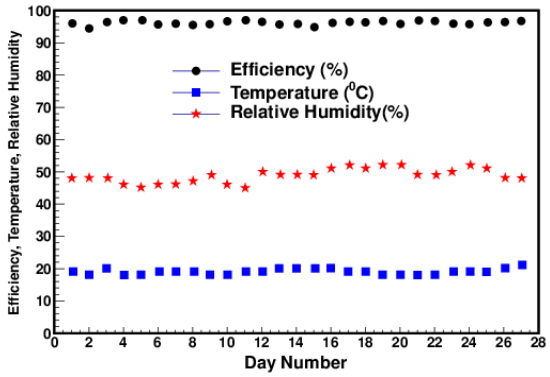

Figure 1.6: *[Colour online] variation of efficiency, temperature and rlative humidity with time. The error bars of efficiencies are within the marker size.*

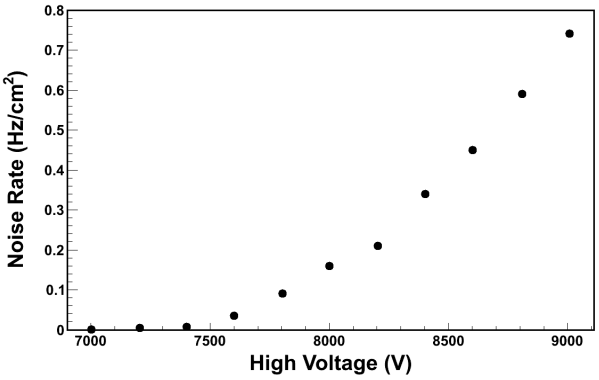

Figure 1.7: *Noise rate of the chamber as a function of the applied voltage. The error bars are within the marker size.*

figure clearly shows two distinct groups, the edges of the RPC are relatively low efficient as the probability of distortion of the electric field and the non-uniformity of gas-flow are higher at these regions. The average efficiency is found to be >95%.

Time resolution

The time resolution of the RPC has been measured only at a central location of the chamber using a 16 channel PHILIPS SCIENTIFIC 7186 TDC module. Figure 1.10 shows the uncorrected time spectra of the RPC at 9000 V. The final RPC time resolution ($\sigma_{RPC}^{corrected}$) has been extracted from the Gaussian fit after removing the contribution of the three scintillators. Figure 1.11 shows

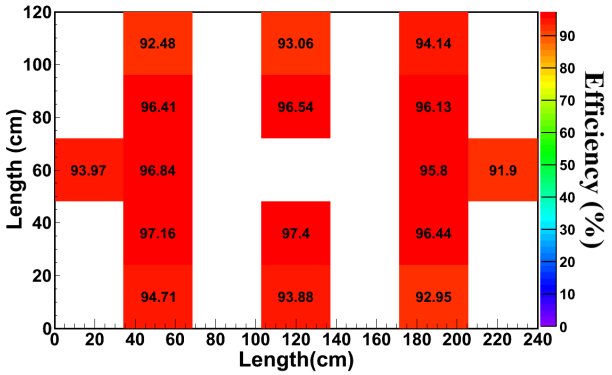

Figure 1.8: *[Colour online] Locations on the RPC plane where efficiency has been measured, along with the measured efficiency values written on the figure.*

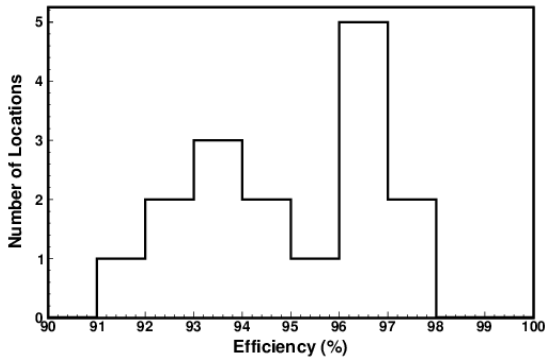

Figure 1.9: *Efficiency measurement at various locations on the RPC surface.*

the variation of time resolution ($\sigma_{RPC}^{corrected}$) of the large RPC as a function of the applied voltage. The best value of the time resolution has been found to be ∼0.83 ns at 9000 V.

1.2.3 Long term performance testing of the large oil-free bakelite RPC

In the following subsections, the test results over a period of 60 days have been discussed.

Current stability

Figure 1.12 shows the variation of current for both the electrodes. The top and middle figures show the current variation for the first and second electrodes respectively whereas the bottom

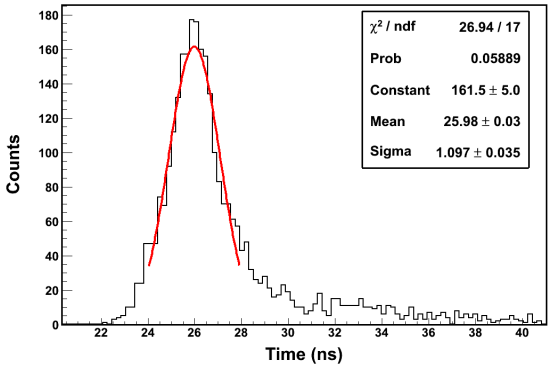

Figure 1.10: *[Colour online] Raw TDC spectra of the RPC at 9000 V. The red curve shows the Gaussian fit.*

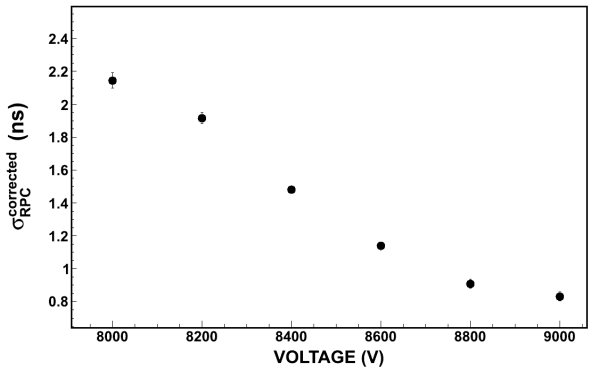

Figure 1.11: *Time resolution ($\sigma_{RPC}^{corrected}$) as a function of the applied voltage.*

figure shows the average current of both the electrodes. We have calculated the bulk resistivity of the chamber from the average current values which is shown in Figure 1.13. The bulk resistivity of the chamber was found to be $\sim 9 \times 10^{13}$ Ωcm.

Efficiency and noise rate

The efficiency of detection of cosmic muons and noise rate of the chamber were also monitored continuously for 60 days. The values of efficiency and noise rate have been shown in Figure 1.14 and Figure 1.15 respectively. The efficiency and noise rate of the chamber have been found to be >95% and $\sim$ 0.75 Hz/cm^2 respectively. Both have been found to remain stable over the entire

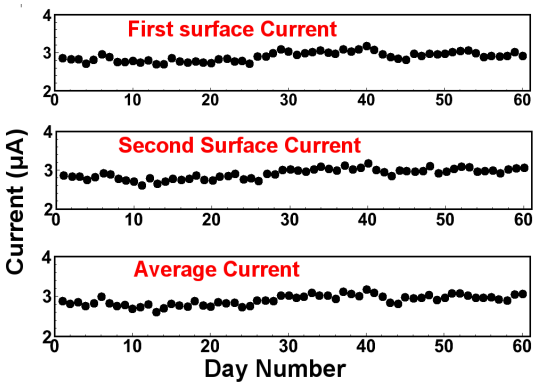

Figure 1.12: *Current stability of the electrodes of over a period of 60 days.*

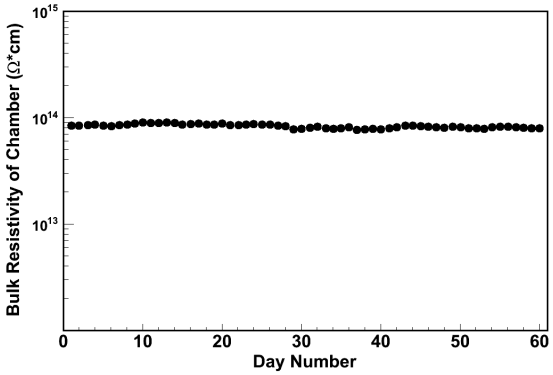

Figure 1.13: *[Colour online] Variation of bulk resistivity of the chamber with time.*

testing period.

Time resolution

Figure 1.16 shows the variation of time resolution (σ) over the entire testing period. The average time resolution of the chamber was found to be $\sim$ 0.83 ns.

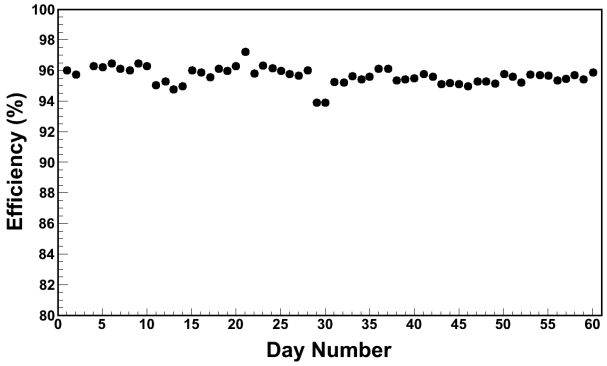

Figure 1.14: *Efficiency of the chamber over a period of 60 days. The error bars are within the marker size.*

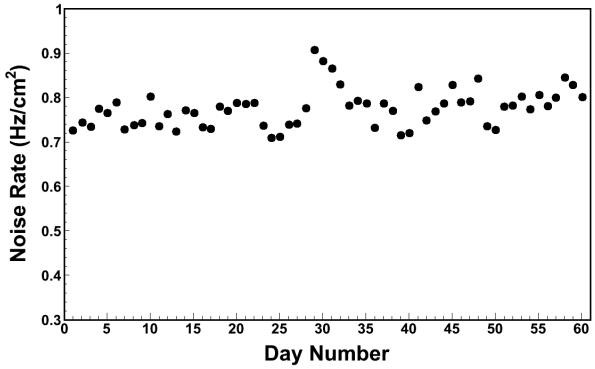

Figure 1.15: *[Colour online] Noise rate of the chamber over a period of 60 days. The error bars are within the marker size.*

1.3 Use Of MRPC For TOF-PET (Time-of-Flight Positron Emission Tomography)

We are also working on a project using Multi-gap Resistive Plate Chambers (MRPCs) for medical applications. MRPC, because of its excellent time resolution is considered to be a potential candidate of TOF-PET systems. In order to explore this avenue, a pair of small sized (18 cm $\times$ 18 cm) 5-gap glass based MRPC's have been built and a system of 511 keV photon pair detection from a Na^{22} source has been setup. The chambers, on an average, give $\sim$ 300 ps time resolution.

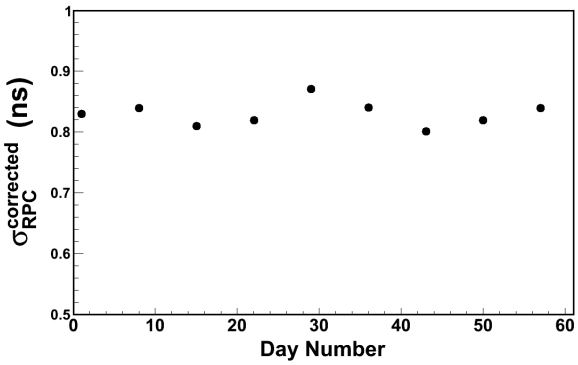

Figure 1.16: *[Colour online] Time resolution (σ) of the chamber over a period of 60 days.*

In this work so far, (a) coincidence rate of two photons using the MRPCs have been obtained (b) preliminary proof-of-principle of TOF-PET imaging has been established by shifting the Na-22 source and obtaining the peaks of the time spectra. We have used two MRPC modules to detect the back to back photons and two plastic scintillators to eliminate the cosmic muons in our measurement by veto method. We have changed the position of the source and found that the difference between the mean of the two fitted TDC spectra at two locations is 35 TDC channels corresponding to a time difference of $\sim$ 0.850 ns. This translates to $\sim$13 cm and matches with the distance between the two locations of the source.

Bibliography

[1] R. Santonico, R. Cardarelli, *Development of Resistive Plate Counters*, *Nucl. Instr. and Meth.* **187** (1981) 377.

[2] INO Project Report,M. Sajjad Athar et al.*India-based Neutrino Observatory: Project Report. Volume I, INO-2006-01 (2006) and online pdf version at* **http://www.ino.tifr.res.in/ino//OpenReports/INOReport.pdf**

[3] http://www.dunescience.org/, arXiv:1601.02984v1.

[4] R. Ganai, *Study of Performance of Bakelite Resistive Plate Chamber (RPC)*, *Springer Proceedings in Physics.* **174** (2016) 547.

[5] R.Ganai, *Fabrication and characterisation of oil-free large High Pressure Laminate Resistive Plate Chamber Journal of Instrumentation.* **JINST 11 P04026** (2016).

List of Figures

List of Tables

Chapter 2

Introduction

I have done something very bad today by proposing a particle that cannot be detected; it is something no theorist should ever do.

Wolfgang Pauli

What do we see when we look deep into the universe ? We see millions and millions of stars, galaxies and other celestial objects. But there is something which we do not see even though they are there right from the beginning of our universe. These are tiny little neutral particles called **neutrinos**. Neutrinos were created at a time of less than a second after the Big Bang [1] and they are still there as they do not easily interact with anything. Trillions of neutrinos pass though our body every second and we don't even feel it as they are weakly interacting particles. Neutrinos played a crucial role in the formation of the universe and our existence. They are playing important roles in several incidents in the universe like death of starts, shinning of stars, formation of stars and so on. Its own proposer doubted if anyone would ever detect them. But they are everywhere right from inside giant stars, black holes to the earth's surface and even in the empty space of the universe.

Neutrinos are one of the most exciting fundamental particles ever known. Studying their properties and interactions have been one of the most exciting and vigorous activities in particle physics and astrophysics ever since Pauli first proposed their existence in 1930. They were first

detected in 1956 by F. Reines and C.L. Cowan. Initially, they were considered to be massless but now we know that they have tiny masses. They are the most abundant particles in the universe after photons. There are ∼340 neutrinos/cc in the universe. Among all other particles, neutrinos have the widest range of energy spectrum. Figure 2.1 shows the known range of energy of neutrinos along with their fluxes. They only experience weak and gravitational interactions. In spite of such a large flux of neutrinos, they are very hard to detect as they are weakly interacting. They are excellent probes for weak interaction studies. In spite of their weakly interacting nature, we have accumulated an enormous amount of knowledge about neutrinos over the past few decades. There are three different flavours of neutrinos known till date. They are ν_μ, ν_e and ν_τ. Their antiparticles also come in three flavours v.i.z $\overline{\nu}_\mu$, $\overline{\nu}_e$ and $\overline{\nu}_\tau$. These neutrinos and anti-neutrinos change from one flavour to another during the course of their travel. This phenomenon is known as "neutrino oscillation". Neutrino oscillation proved that neutrinos have mass. However, we still do not know the absolute values of their masses and some aspects of their flavour mixing.

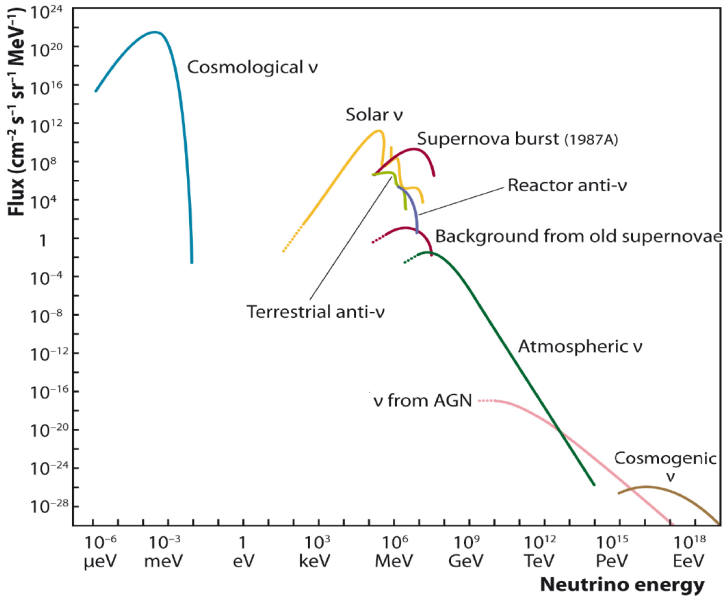

Figure 2.1: *[Colour online] Neutrino flux versus neutrino energy [2].*

2.1 A Brief Introduction to Neutrinos

With the discovery of radioactivity of uranium in 1896 by Becquerel, mankind started to learn about the *weak interactions*. Three years later, α and β were introduced as two different by-products by Rutherford with γ to be discovered later. In 1914, the then physicists started to face a very puzzling problem when Chadwick demonstrated that the β-spectrum was continuous, in contrast to α and γ-rays which were unique in energy. This astonishing result was confirmed in 1927 by Ellis and Wooster and a question mark arose on energy conservation in beta decay. N. Bohr suggested that, perhaps energy conservation held only in a statistical sense. Meitner demonstrated that the missing energy could not be ascribed to γ-rays leading to the idea of the existence of a new particle that might explain the missing energy. With this idea, W. Pauli tried to combine problem of the spin and statistics of nuclei with the problem of the continuous beta spectrum, without abandoning the conservation of energy and proposed, in an open letter to a physics conference at T*ü*bingen on 4 December 1930, addressed to "Dear Radioactive Ladies and Gentlemen", that the existence of a neutral weakly interacting fermion emitted in β-decay could solve the problems [3] and called this neutral fermion **neutron**. E. Fermi renamed the Pauli particle the **neutrino** after J. Chadwick discovered **the neutron** as we know it today in 1932. In 1933, Fermi [4] and Perrin [5] independently concluded neutrinos could be massless! The first published reference to the neutrino is in the Proceedings of the Solvay Conference of October 1933.

In 1934, H. Bethe and R. Peierls predicted the strength of neutrino interactions and claimed by that neutrinos might never be observed [6]. But in the early 1950's, urged, in particular by B. Pontecorvo, F. Reines and C.L. Cowan searched for a way to measure inverse β-decay, in which an anti-neutrino can produce a positron. By using a large flux of anti-neutrinos from a nuclear reactor and 10 ton of equipment, including 1400 liters of liquid scintillators, they successfully detected neutrino, in fact electron anti-neutrino ($\overline{\nu}_e$). This experiment was the first reactor neutrino experiment. In June of 1956, Reines and Cowan sent a telegram informing Pauli of the discovery [7] [8]. Reines (Cowan passed away) was awarded the Nobel prize 40 years later in

1995. Figure 2.2 shows Pauli's reply.

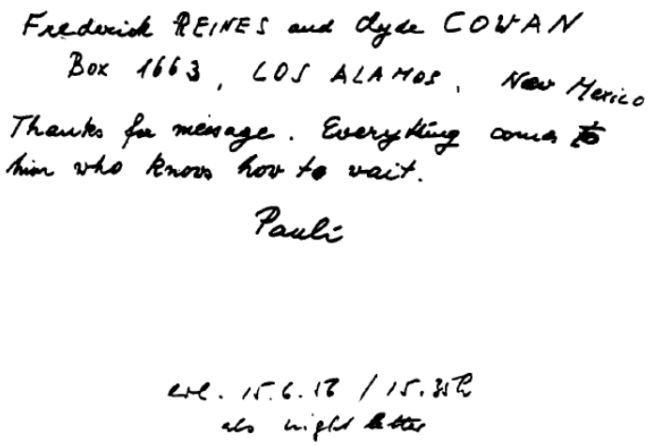

Figure 2.2: *[Colour online] The letter Pauli sent in response to Cowan and Reines's telegram.*

In 1962, L.M. Lederman, M. Schwartz and J. Steinberger et. al. [9] discovered the existence of the muon neutrino (ν_μ) at the Brookhaven National Laboratory (BNL). This experiment utilized an enormous amount of iron shielding plates cut out of the battleship USS Missouri and marked the first serious accelerator neutrino experiment. The detection of tau (τ) neutrino (ν_τ) was reported in July 2000 by DONUT (Direct Observation of the Nu Tau) collaboration. The DONUT experiment in Fermilab was built during the 1990s to specifically detect the tau neutrino. The detection of ν_τ completed the three lepton families, consisting of three charged leptons (e, μ, τ) and the associated neutrinos (ν_e, ν_μ, ν_τ).

Neutrinos played an important role in the discovery of parity violation. The violation of parity in weak interactions was first proposed by Lee and Yang in an attempt to solve the famous τ - θ puzzle[10]. C.S. Wu showed that there is forward - backward asymmetry of the electrons emitted from the β decay of polarized ^{60}Co and hence the parity violation[11]. Neutrino oscillation opened the window on physics beyond Standard Model (SM) as SM predicted that neutrinos are massless. But the famous "solar neutrino problem" and its solution unveiled that neutrinos oscillate and they are massive. The discovery of existence of neutrinos led to a new

field of research which may reveal many truths about the universe including our own existence.

2.2 Sources of neutrinos

Neutrinos are emitted from several processes. The sources can be classified broadly as natural and man-made. The energy, flux and process of generation of neutrinos depend of the kind of source they emerge from. As their interaction cross section is very low, they prove to be very efficient messengers of their sources. Hence they are also known as "messenger particles". This section discusses the important sources of neutrinos.

2.2.1 Solar neutrinos

The Sun is a very powerful source of neutrinos, specially electron neutrinos, of energy of the order of 1 MeV. These neutrinos are produced in the thermonuclear fusion reactions in the core of the sun. As the interaction of neutrinos with matter is very weak, practically all the neutrinos produced pass undisturbed through the interior of the sun. The solar neutrino flux on the earth is $\sim 6 \times 10^{10}$ cm$^{-2}s^{-1}$ [12]. The solar neutrinos were first detected in 1970 in the Homestake Experiment [13], [14]. The Sun shines because of the energy produced in its core by thermonuclear reactions. There are many models which predict about these thermonuclear reactions. According to the Standard Solar Model [15], these thermonuclear reactions are exothermal thermonuclear fusion of hydrogen to helium. This process can be written as

$$4p \rightarrow {}^4He + 2e^+ + 2\nu_e + 26.731 MeV \tag{2.1}$$

This energy is released in the form of photons or kinetic energy of the neutrinos (only a small fraction). The kinetic energy of ^{4}He nucleus is negligible because of its large mass. Extremely large number of these reactions taking place inside the core of the Sun results into such a huge flux of ν_e. We, on the earth, receive only a small fraction of the solar neutrinos. Figure 2.5

shows the flux of the solar neutrinos along with their energy. The energy production mechanism inside the sun can be divided into two cycles: (i) Proton – Proton (PP) cycle, and (ii) Carbon – Nitrogen – Oxygen (CNO) cycle. Figure 2.3 and Figure 2.4 show production mechanisms of solar neutrinos by PP-cycle and CNO cycle respectively. Figure 2.5 shows the solar neutrino energy spectrum along with the uncertainities [16].

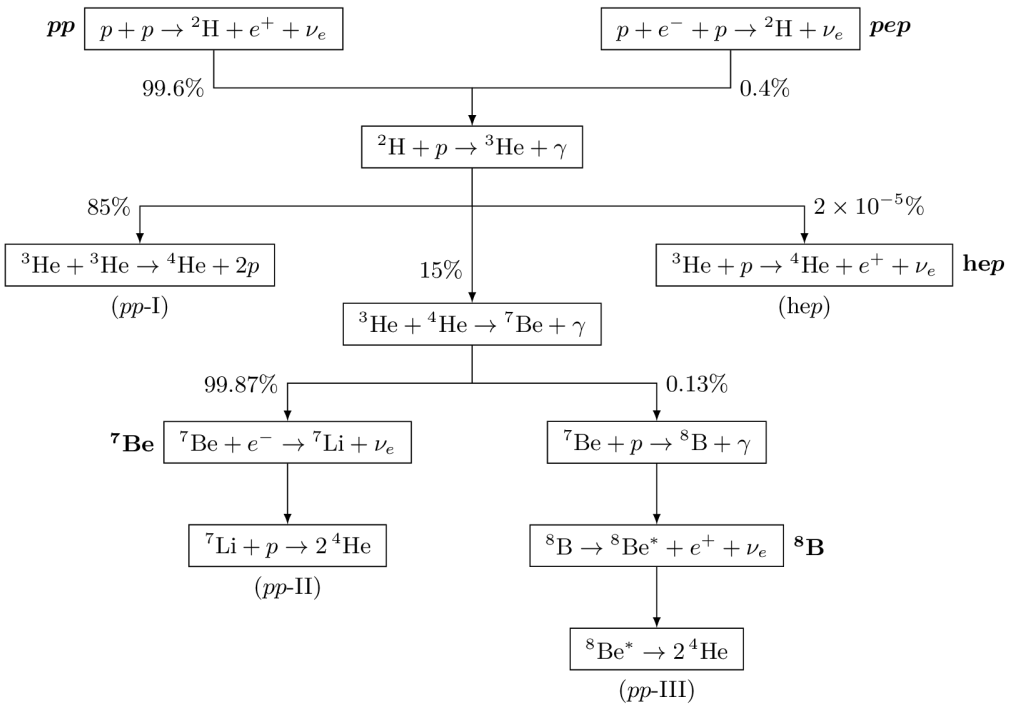

Figure 2.3: *[Colour online] Production of solar neutrinos by pp chain [12].*

2.2.2 Atmospheric neutrinos

We know that primary cosmic rays consist of mostly protons with a small fraction of heavier nuclei. When these primary cosmic rays interact with the nuclei in the atmosphere, they generate secondary cosmic rays which consist of hadrons and their decay products. In particular, many secondary pions are produced. These pions mainly decay into muons and corresponding neutrinos as follows :

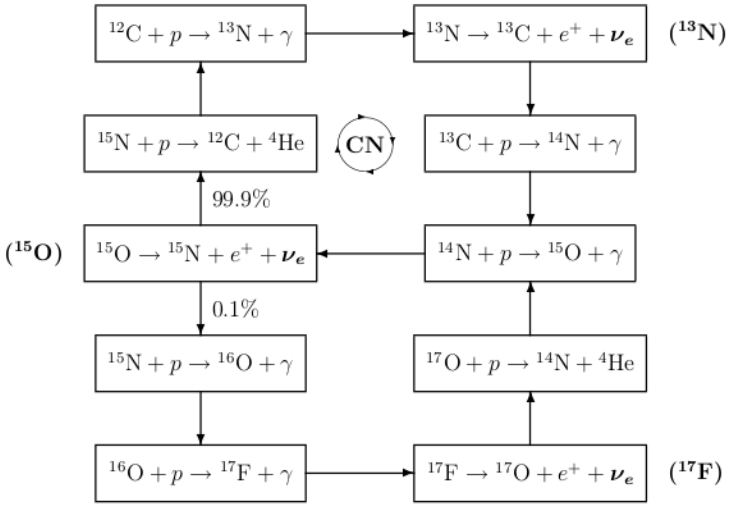

Figure 2.4: *[Colour online] Production of solar neutrinos by CNO cycle[12].*

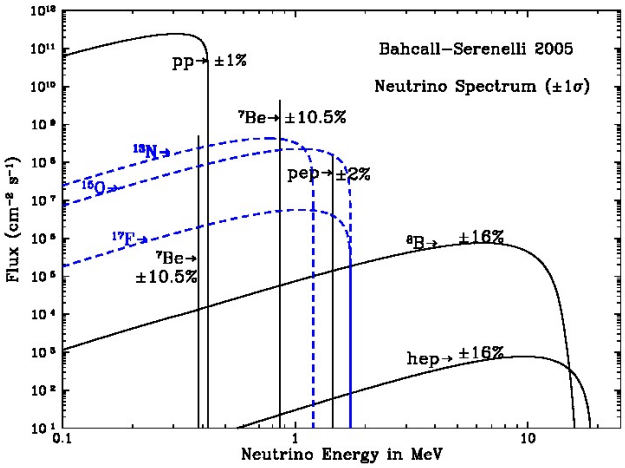

Figure 2.5: *[Colour online] Flux of solar neutrinos[16].*

$$\pi^+ \rightarrow \mu^+ + \nu_\mu \tag{2.2}$$

$$\pi^- \rightarrow \mu^- + \overline{\nu}_\mu \tag{2.3}$$

At sufficient high energies, kaons also contribute to the production of muons. Before reaching the earth's surface, these muons decay as follows:

$$\mu^+ \rightarrow e^+ + \nu_e + \overline{\nu}_\mu \tag{2.4}$$

$$\mu^- \rightarrow e^- + \overline{\nu}_e + \nu_\mu \tag{2.5}$$

Figure 2.6 shows a schematic of the production of the atmospheric neutrinos.

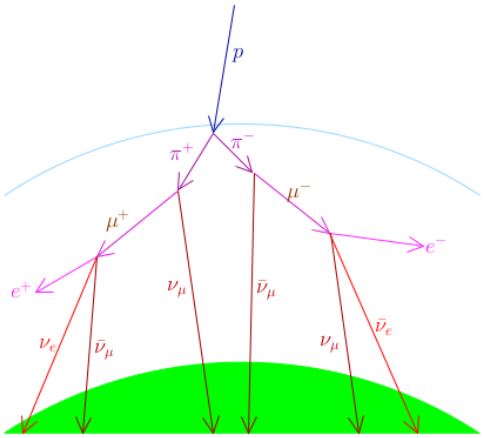

Figure 2.6: *[Colour online] Production of atmospheric neutrinos. [12]*

The energies of atmospheric neutrinos vary from ∼100 MeV to ∼100 GeV. These atmospheric neutrinos are produced ∼15 km above the earth's surface. In order to detect these muon neutrinos (anti-neutrinos), the detectors must be underground so that a suitable shielding can

be provided to the cosmic muons. The earth provides a wide range of baselines (path lengths of neutrinos travelling from the point of production to the detector) from ∼few hundreds of km to ∼13000 km for the detection of atmospheric neutrinos. From equations 2.2, 2.3, 2.4 and 2.5 it is clear that at energies $\lesssim$1 GeV, the neutrino fluxes satisfy the following ratios :

$$(\phi_{\nu_\mu} + \phi_{\overline{\nu}_\mu})/(\phi_{\nu_e} + \phi_{\overline{\nu}_e}) \simeq 2, \quad \phi_{\nu_\mu}/\phi_{\overline{\nu}_\mu} \simeq 1, \quad \phi_{\nu_e}/\phi_{\overline{\nu}_e} \simeq \phi_{\mu^+}/\phi_{\mu^-} \tag{2.6}$$

At higher energies the number of muons hitting the earth's surface before decaying increases resulting in the increase in the ratio of $(\phi_{\nu_\mu} + \phi_{\overline{\nu}_\mu})/(\phi_{\nu_e} + \phi_{\overline{\nu}_e})$. The basic principles of detection of atmospheric neutrinos were already known in the 1960s. In 1965 two groups reported the observation of atmospheric neutrinos by detectors in the Kolar Gold Field Mine in South India[17],[18] and in the East Rand Proprietary Gold Mine in South Africa[19].

2.2.3 Relic neutrinos

The Big Bang Theory predicted the existence of the cosmic neutrino background (CνB). The properties of CνB are closely related to cosmic microwave background. The Big Bang relic neutrinos are the second most abundant particles in the universe. There are ∼336 cm^{-3} relic neutrinos. They are an essential ingredient of the Standard Cosmological Model. At the beginning of the universe, the neutrinos were in thermal equilibrium with other particles through weak interaction in the hot plasma. As the universe expanded, it cooled resulting a decrease in the rates of weak interaction processes. As these rates became smaller than the expansion rate and the neutrinos were relativistic, they decoupled. These neutrinos are hot relics. The kinetic energy of these neutrinos are predicted to be $\sim 10^{-4}$eV which results into even smaller interaction cross-section ($\sim 10^{-64} cm^2$) with matter. Hence, the detection of relic neutrinos is very difficult and challenging with today's technology and experimental techniques. As relic neutrinos are produced during the Big Bang and weakly interacting, they are predicted to be

good probe to the early universe.

2.2.4 Accelerator neutrinos

Accelerator neutrinos are produced by the decay of charged pions and kaons. When a beam of high energy protons is bombarded on a specific target, several particles like pions and kaons are produced. The charged pions and kaons are focussed using a magnetic horn towards an evacuated decay tunnel where they eventually decay to muons and neutrinos. The remaining mesons and the produced muons are absorbed in a beam dump at the end of the tunnel. This ultimately, produces a neutrino beam consisting of muon neutrinos. Another way of producing accelerator neutrino beam is by the semi-leptonic decay of the charmed particles. These particles are produced when a high energetic proton beam is stopped by a thick target generating heavy hadrons. These charmed heavy hadrons decay producing equal fluxes of high energy electrons and muon neutrinos.

2.2.5 Supernovae neutrinos

Supernovae are extremely powerful explosions which terminate the life of some stars. Supernovae produced by the collapse of the core of massive stars produce large fluxes of neutrinos that could be detected on the Earth. The supernovae neutrinos are produced by the electron capture of nuclei and free protons. The hot core of the resultant proto–neutron star, too, produces neutrinos through various processes. As neutrinos are weakly interacting, they easily escape the highly dense core of these stars and may reach the earth earlier than the photons from the explosion. The flux of the supernovae neutrinos is very high, hence they are very efficient source to study supernovae as well as neutrino characteristics. Neutrinos of all flavours are produced in the hot core of the proto-neutron star, which has a temperature of about 40 MeV, through electron–positron pair annihilation. The only supernova that has been detected through the neutrino burst is The SN1987A which has provided landmark results in the neutrino astronomy [20], [21], [22].

2.2.6 Galactic and extra galactic neutrinos or Astrophysical Neutrinos

Astrophysical sources like Gamma-Ray Burst (GRB), Active Galactic Nuclei (AGN) emit neutrinos with very high energy. Astrophysical sources like Supernova Remnants (SNRs), AGNs, GRBs can accelerate protons to very high energies by the Fermi acceleration mechanism. Ultra high energy (UHE) neutrinos are produced by the interaction of these protons with matter or soft photons by several processes like $p\gamma$, $pp \rightarrow \pi^{\pm}X$, $\pi^{\pm} \rightarrow \mu^{\pm}\nu_{\mu}(\overline{\nu}_{\mu})$, $\mu^{\pm} \rightarrow e^{\pm}\overline{\nu}_{\mu}(\nu_{\mu})\nu_{e}(\overline{\nu}_{e})$ with a flux ratio of $\phi_{\nu_e} : \phi_{\nu_\mu} : \phi_{\nu_\tau} :: 1 : 2 : 0$. These neutrino fluxes do not get bent in the interstellar magnetic field. As the flux of these neutrinos reaching the earth is very low, large volume neutrino telescopes are required to detect them. One such telescope, the IceCube detector has already detected a total of 37 neutrino events with deposited energies ranging from 30 TeV to 2 PeV [23], [24], [25]. The event with 2 PeV energy is the highest-energy neutrino event ever observed.

2.2.7 Reactor neutrinos

Nuclear reactors are copious sources of artificially produced neutrinos. These neutrinos are mainly electron anti-neutrinos. These are produced by the chain β-decays of the fission products. The flux of these neutrinos is very high which ultimately depends on the power of the reactor. The power generated by a conventional nuclear reactor is mainly due to the fission of four isotopes U-235 ($\sim$56%), U-238 ($\sim$8%), Pu-239 ($\sim$30%) and Pu-241 ($\sim$6%). The reactor electron anti-neutrinos are detected through inverse neutron decay process. In fact the first neutrino detected was reactor electron anti-neutrino by this process [7], [8]. The energy of reactor neutrinos varies from 0.1 MeV to $\sim$10 MeV.

2.2.8 Geo-neutrinos

Geo-neutrinos are electron anti-neutrinos emitted in β- decay of a radionuclide like U-238, Th-232, K-40, naturally existing inside the Earth [26], [27], [28]. These are produced by the following decay schemes:

$$^{238}U \rightarrow^{206} Pb + 8\alpha + 8e^{-} + 6\overline{\nu}_e + 51.7MeV \tag{2.7}$$

$$^{232}Th \rightarrow^{208} Pb + 6\alpha + 4e^{-} + 4\overline{\nu}_e + 42.7MeV \tag{2.8}$$

$$^{40}K \rightarrow^{40} Ca + e^{-} + \overline{\nu}_e + 1.31MeV \tag{2.9}$$

As the geo-neutrino flux and the radiogenic heat generated are in a well fixed ratio, a precise measurement of the flux of these neutrinos can provide crucial insight to the radiogenic heat developed and thereafter to the composition to the inner structure of the earth.

2.3 Neutrino Oscillations

Neutrino oscillation is a quantum mechanical phenomenon in which a neutrino of certain flavour with certain energy oscillates into another flavour during the course of its travel. It was first proposed in the late 1950s by Pontecorvo in analogy with K ^{0} - $\overline{K}^0$ oscillations [29], [30]. Before the discovery of neutrino oscillations, neutrinos were considered to be massless by the Standard Model. Other than neutrino oscillation experiments, no experiments have been performed so far that have detected conclusive deviations from the Standard Model. It is very difficult to understand how neutrinos get their mass, however small they are, and how they are mixed. Thus neutrinos play an important role to understand the new physics beyond Standard Model. The famous "solar neutrino problem"led to the discovery of neutrino oscillations. Solar neutrino problem was the deficit in the observed solar electron neutrino flux with respect to the predicted solar electron neutrino flux produced in the Sun by the Standard Solar Model. The solar electron neutrino flux was first measured in the Homestake experiment [13], [14] which led to the discovery of solar neutrino problem. This was later confirmed by the observations of the Kamiokande, GALLEX/GNO, SAGE, Super-Kamiokande, and SNO experiments. In 2002, the results of the SNO experiment [33] proved useful in solving the solar neutrino problem. The depletion in the solar neutrinos was found to be due to the oscillations of ν_e into ν_μ and ν_τ inside

the Sun by the MSW resonance conversion effects. The SNO collaboration determined the total number of solar neutrinos of all types (electron, muon, and tau) as well as the number of just electron neutrinos by combining the SNO and the Super-Kamiokande measurements. The total number of neutrinos of all types agreed with the number predicted by the solar model. Electron neutrinos constitute about a third of the total number of neutrinos. But Pontecorvo predicted the "solar neutrino problem"even before the first measurement of the solar electron neutrino flux. The discovery and confirmation of neutrino oscillation led to Nobel prize to Prof. Takaaki Kajita and Prof. Arthur B. McDonald in 2015.

This section discusses the neutrino oscillations in vacuum and matter.

2.3.1 Neutrino oscillation in vacuum

According to the standard theory of neutrino oscillations, a neutrino of flavour α (ν_α) with momentum $\vec{p}$, is a superposition of massive neutrinos, ν_k (mass m_k) with weights proportional to $U^*_{\alpha k}$ and can be written as

$$|\nu_\alpha\rangle = \sum_k U^*_{\alpha k}|\nu_k\rangle \qquad (\alpha = e, \mu, \tau) \qquad and \qquad (k = 1, 2, 3) \tag{2.10}$$

where, $U_{\alpha k}$ is known as the Pontecorvo–Maki–Nakagawa–Sakata (PMNS) matrix or the lepton mixing matrix. The PMNS mixing matrix can be written as

$$U = \begin{pmatrix} c_{12}c_{13} & s_{12}c_{13} & s_{13}e^{-i\delta} \\ -s_{12}c_{23} - c_{12}s_{23}e^{i\delta} & c_{12}c_{23} - s_{12}s_{23}s_{13}e^{i\delta} & s_{23}c_{13} \\ s_{12}s_{23} - c_{12}c_{23}s_{13}e^{i\delta} & -c_{12}s_{23} - s_{12}c_{23}s_{13}e^{i\delta} & c_{23}c_{13} \end{pmatrix}$$

The massive neutrino states $|\nu_k\rangle$ are the eigenstates of the vacuum Hamiltonian,

$$\mathcal{H}_0|\nu_k\rangle = E_k|\nu_k\rangle \tag{2.11}$$

with energy eigenvalues

$$E_k = \sqrt{\vec{p}^2 + m_k^2} \tag{2.12}$$

Using the time dependent Schrödinger equation, the time evolution of the state can be written as

$$|\nu_\alpha(t)\rangle = \sum_k U^*_{\alpha k} e^{-iE_k t} |\nu_k\rangle \tag{2.13}$$

so that,

$$|\nu_\alpha(t=0)\rangle = |\nu_\alpha\rangle \tag{2.14}$$

Using the unitary relation of U, the massive states can be expressed in terms of flavour states as

$$|\nu_k\rangle = \sum_\alpha U_{\alpha k} |\nu_\alpha\rangle \tag{2.15}$$

Substituting equation (2.12) in equation (2.10), we get

$$|\nu_\alpha(t)\rangle = \sum_{\beta=e,\mu,\tau} (\sum_k U^*_{\alpha k} e^{-iE_k t} U_{\beta k}) |\nu_\beta\rangle \tag{2.16}$$

The amplitude of $\nu_\alpha \longrightarrow \nu_\beta$ is the coefficient of $|\nu_\beta\rangle$,

$$A_{\nu_\alpha \longrightarrow \nu_\beta}(t) \equiv \langle \nu_\beta | \nu_\alpha(t) = \sum_k U^*_{\alpha k} U_{\beta k} e^{-iE_k t} \tag{2.17}$$

The probability of neutrino oscillation from one flavour to another flavour ($P_{\nu_\alpha \longrightarrow \nu_\beta}$), known as transition probability, is given by

$$P_{\nu_\alpha \longrightarrow \nu_\beta}(t) = |A_{\nu_\alpha \longrightarrow \nu_\beta}(t)|^2 = \sum_{k,j} U^*_{\alpha k} U_{\beta k} U_{\alpha j} U^*_{\beta j} e^{-i(E_k - E_j)t} \tag{2.18}$$

For ultra-relativistic neutrinos,

$$E_k - E_j \simeq \frac{\Delta m^2_{kj}}{2E}, \qquad where, \qquad \Delta m^2_{kj} \equiv (m^2_k - m^2_j) \quad and \quad E = |\vec{p}| \tag{2.19}$$

With the above substitution in equation (2.15), it becomes,

$$P_{\nu_\alpha \longrightarrow \nu_\beta}(t) = \sum_{k,j} U^*_{\alpha k} U_{\beta k} U_{\alpha j} U^*_{\beta j} exp(-i \frac{\Delta m^2_{kj} t}{2E}) \tag{2.20}$$

In neutrino oscillation experiments, the propagation time t is not measured. What is known is the distance traveled by the neutrino(s) (L) between the source and the detector. Since the neutrinos are ultra-relativistic, it is possible to approximate t = L, which makes equation (2.17) as

$$P_{\nu_\alpha \longrightarrow \nu_\beta}(L, E) = \sum_{k,j} U^*_{\alpha k} U_{\beta k} U_{\alpha j} U^*_{\beta j} exp(-i \frac{\Delta m^2_{kj} L}{2E}) \tag{2.21}$$

Equation (2.18) is the probability of oscillation of neutrino with energy, E, and traveling a

distance, L, from one flavour to another in vacuum. Equation (2.18) can also be written as

$$P_{\nu_\alpha \longrightarrow \nu_\beta}(L,E) = \sum_k |U^2_{\alpha k}||U^2_{\beta k}| + 2\Re \sum_{k>j} U^*_{\alpha k} U_{\beta k} U_{\alpha j} U^*_{\beta j} exp(-2\pi i \frac{L}{L^{osc}_{kj}}) \tag{2.22}$$

$$where \qquad L^{osc}_{kj} = \frac{4\pi E}{\Delta m^2_{kj}} \tag{2.23}$$

is called the oscillation length. It is the distance at which the phase generated by Δm^2_{kj} becomes equal to 2π.

Separating the real part and imaginary part, equation (2.18) can also be written as

$$P_{\nu_\alpha \longrightarrow \nu_\beta}(L,E) = \delta_{\alpha\beta} - 4\sum_{k>j} \Re[U^*_{\alpha k} U_{\beta k} U_{\alpha j} U^*{}_{\beta j}] \sin^2(\frac{\Delta m^2_{kj} L}{4E}) + 2\sum_{k>j} \Im[U^*_{\alpha k} U_{\beta k} U_{\alpha j} U^*_{\beta j}] \sin(\frac{\Delta m^2_{kj} L}{2E}) \tag{2.24}$$

The oscillation probabilities ($P_{\nu_\alpha \longrightarrow \nu_\beta}$) with $\alpha \neq \beta$ are known as transition probabilities whereas those with $\alpha = \beta$ are known as survival probabilities.

For anti-neutrinos, equation (2.9) looks like

$$|\overline{\nu}_\alpha\rangle = \sum_k U_{\alpha k} |\overline{\nu}_k\rangle \qquad (\alpha = e, \mu, \tau). \tag{2.25}$$

Applying the similar procedure as in neutrino oscillations, the oscillation probability of anti-neutrinos from one flavour to another can be obtained as

$$P_{\overline{\nu}_\alpha \longrightarrow \overline{\nu}_\beta}(L,E) = \sum_{k,j} U_{\alpha k} U^*_{\beta k} U^*_{\alpha j} U_{\beta j} exp(-i \frac{\Delta m^2_{kj} L}{2E}) \tag{2.26}$$

Separating the real and imaginary parts, equation (2.23) looks like

$$P_{\overline{\nu}_\alpha \longrightarrow \overline{\nu}_\beta}(L,E) = \delta_{\alpha\beta} - 4\sum_{k>j} \Re[U^*_{\alpha k} U_{\beta k} U_{\alpha j} U^*_{\beta j}] \sin^2(\frac{\Delta m^2_{kj} L}{4E}) - 2\sum_{k>j} \Im[U^*_{\alpha k} U_{\beta k} U_{\alpha j} U^*_{\beta j}] \sin(\frac{\Delta m^2_{kj} L}{2E}) \quad (2.27)$$

From equations (2.18) and (2.23), we can note that the oscillation length of neutrinos and anti-neutrinos are the same. The oscillation length of neutrinos (anti-neutrinos) depends only on the kinematical properties of massive neutrinos (anti-neutrinos). From equations (2.21) and (2.24), one can note that the oscillation probability of anti-neutrinos differs from that of neutrinos only in the sign of the terms depending on the imaginary parts of the quartic products of the elements of the mixing matrix.

2.3.2 Neutrino oscillation in matter

Neutrinos traveling through matter experience a potential, equivalent to an index of refraction, because of the coherent and incoherent scattering with the particles (electrons and nucleons) in the medium . This modifies the mixing of neutrinos in matter significantly as a result the oscillation probability of neutrinos traveling through matter differs from those traveling through vacuum. The effective mixing of neutrinos travelling through matter for three neutrino case was formulated by S.P Mikheev, A.yu. Smirnov and L. Wolfenstein. This phenomenon is known as MSW mechanism [32], [34], [35].

A neutrino of certain flavour with momentum $\vec{p}$ can be written as a combination of the massive neutrino states which are the eigen states of the vacuum Hamiltonian, $\mathcal{H}_0$, as described in equations (2.9), (2.10) and (2.11). But the total Hamiltonian in matter is different from that in vacuum and is given by

$$\mathcal{H} = \mathcal{H}_0 + \mathcal{H}_1, \qquad with \qquad \mathcal{H}_1|\nu_\alpha\rangle = V_\alpha|\nu_\alpha\rangle \quad (2.28)$$

where,

$$V_\alpha|\nu_\alpha\rangle = \sqrt{2}G_F(N_e\delta_{\alpha e} - \frac{1}{2}N_n) \qquad where \qquad \alpha = e, \mu, \tau \tag{2.29}$$

N_e and N_n in equation (2.28) are the electron and nucleon density respectively in the medium and G_F is the Fermi coupling constant. Further, it can be shown that the relevant evolution equation for flavour transition amplitudes can take the form

$$i\frac{d}{dx}\Psi_\alpha = \mathcal{H}_F\Psi_\alpha \tag{2.30}$$

with the effective Hamiltonian matrix $\mathcal{H}_F$ in the flavour basis

$$\mathcal{H}_F = \frac{1}{2E}(U\mathcal{M}^2U^\dagger + \mathcal{A}) \tag{2.31}$$

where,

$$\Psi_\alpha = \begin{pmatrix} \psi_{\alpha e} \\ \psi_{\alpha\mu} \\ \psi_{\alpha\tau} \end{pmatrix}, \quad \mathcal{M}^2 = \begin{pmatrix} 0 & 0 & 0 \\ 0 & \Delta m^2_{21} & 0 \\ 0 & 0 & \Delta m^2_{31} \end{pmatrix}, \quad \mathcal{A} = \begin{pmatrix} A_{CC} & 0 & 0 \\ 0 & 0 & 0 \\ 0 & 0 & 0 \end{pmatrix}.$$

where,

$$A_{CC} \equiv 2EV_{CC} = 2\sqrt{2}EG_FN_e. \qquad with \quad V_{CC} = \sqrt{2}G_FN_e. \tag{2.32}$$

V_{CC} is the charged current potential.

For a two neutrino case with initial ν_e state i.e $\nu_e \to \nu_\mu$, it can be shown that the effective mixing matrix in matter is given by

$$U_M = \begin{pmatrix} cos\vartheta_M & sin\vartheta_M \\ -sin\vartheta_M & cos\vartheta_M \end{pmatrix}$$

and the effective mass-squared difference is given by

$$\Delta m^2_M = \sqrt{(\Delta m^2 cos2\vartheta - A_{CC})^2 + (\Delta m^2 sin2\vartheta)^2} \tag{2.33}$$

The effective mixing angle in the matter (ϑ_M) is given by

$$tan2\vartheta_M = \frac{tan2\vartheta}{1 - \frac{A_{CC}}{\Delta m^2 cos2\vartheta}}. \tag{2.34}$$

There is a resonance in oscillation when A_{CC} becomes equal to

$$A^R_{CC} = \Delta m^2 cos2\vartheta, \tag{2.35}$$

corresponding to the electron number density

$$N^R_e = \frac{\Delta m^2 cos2\vartheta}{2\sqrt{2} E G_F}. \tag{2.36}$$

At the resonance the effective mixing angle is equal to $\pi/4$, hence, the mixing is maximal. This leads to the possibility of total transitions between the two flavors if the resonance region is wide enough. This mechanism is called the MSW effect.

Since, in normal matter, A_{CC} is positive, a resonance can exist only if $\vartheta < \pi/4$, because for $\vartheta > \pi/4$, cos $2\vartheta < 0$. Therefore, the behavior of neutrino oscillations in matter is different from that of neutrino oscillations in vacuum, whose probability is symmetric under the exchange $\vartheta \rightarrow \pi/2$ - ϑ, as for two neutrino case, the oscillation probability of neutrinos in vacuum is given by

$$P_{\nu_\alpha \rightarrow \nu_\beta}(L, E)|_{vacuum} = sin^2 2\vartheta sin^2(\frac{\Delta m^2 L}{4E}), \qquad for \quad \alpha \neq \beta. \tag{2.37}$$

For the case of anti-neutrinos, the potential is reversed, hence the resonance can occur only if $\vartheta > \pi/4$ [12].

If $d\vartheta_M/dx = 0$, i.e the matter density is constant, where x is the distance traveled by the neutrino through matter, the oscillation probability becomes

$$P^m_{\nu_\alpha \to \nu_\beta}(x) = sin^2 2\vartheta_M sin^2(\frac{\Delta m^2_M x}{4E}), \qquad for \quad \alpha \neq \beta. \tag{2.38}$$

Equation 2.38 has the similar structure as that of equation 2.37 i.e the structure of two neutrino transition probability in constant matter density is same as that in vacuum except that the mixing angle and mass squared difference are replaced by their values in matter. The oscillation in matter is given by

$$L^{osc}_M = \frac{4\pi E}{\Delta m^2_M}. \tag{2.39}$$

For variable matter density profile, the effect of $d\vartheta_M/dx$ has to be taken into account, which is given by

$$\frac{d\vartheta_M}{dx} = \frac{1}{2}\frac{sin2\vartheta_M}{\Delta m^2_M}\frac{dA_{CC}}{dx}. \tag{2.40}$$

Since the oscillation probability is effected by the presence of matter, studying the same by separating the neutrino and anti-neutrino events may give an idea about the density profile of the matter through which the neutrinos pass.

2.4 Present status of neutrino oscillation parameters

Neutrinos are ubiquitous and have always surprised mankind. Observation of neutrino oscillation has shown that neutrinos are massive and there is physics beyond the Standard Model. For three flavour neutrinos, the oscillation is governed by three mixing angles θ_{12}, θ_{13} ,θ_{23}, a CP violating phase δ_{cp} and two mass squared differences Δm^2_{21} and Δm^2_{31}. Several experiments are dedicated to study the neutrino oscillation phenomenon and the precision measurement of the oscillation parameters with neutrinos from different sources and in different energy ranges. Table 2.1 gives

a list of the present experiments with the determination of the oscillation parameters and table 2.2 gives the list of recent best fit and 3σ range of the oscillation parameters for both normal and inverted hierarchies. The measurement of solar neutrino oscillation parameters (Δm^2_{21}, θ_{12})

Experiments	**Dominant**	**Important**
Accelerator LBL ν_e appearance (Minos, NOνA, T2K)	δ_{CP}	θ_{13}, θ_{23}, sign(Δm^2_{3l})
Accelerator LBL ν_μ disappearance (Minos, NOνA, T2K)	$\lvert\Delta m^2 3l\rvert$, θ_{23}	
Atmospheric experiments	θ_{23}	$\lvert\Delta m^2_{3l}\rvert$, θ_{13}, δ_{CP}
Reactor LBL (KamLAND)	Δm^2_{21}	θ_{12}, θ_{13}
Reactor MBL (Daya-Bay, RENO, D-Chooz)	θ_{13}	$\lvert\Delta m^2_{3l}\rvert$
Solar experiments	θ_{12}	Δm^2_{21}, θ_{13}

Table 2.1: *Experiments contributing to the present determination of the oscillation parameters. Here, $l = 1$ for Normal Hierarchy (NH) and $l = 2$ for Inverted Hierarchy (IH).For NH, $\Delta m^2_{3l} \equiv \Delta m^2_{31} > 0$ and for IH,$\Delta m^2_{3l} \equiv \Delta m^2_{32} < 0$. LBL and MBL stands for Long Baseline and Medium Baseline respectively. This table has been taken from reference [31].*

Oscillation parameter	**Best fit value $\pm1\sigma$ (NH)**	**3σ range (NH)**	**Best fit value$\pm1\sigma$ (IH)**	**3σ range (IH)**
$\sin^2\theta_{12}$	$0.304^{+0.013}_{-0.012}$	$0.270 \rightarrow 0.344$	$0.304^{+0.013}_{-0.012}$	$0.270 \rightarrow 0.344$
$\theta_{12}(^\circ)$	$33.48^{+0.78}_{-0.75}$	$31.29 \rightarrow 35.91$	$33.48^{+0.78}_{-0.75}$	$31.29 \rightarrow 35.91$
$\sin^2\theta_{23}$	$0.452^{+0.052}_{-0.028}$	$0.382 \rightarrow 0.643$	$0.579^{+0.025}_{-0.037}$	$0.389 \rightarrow 0.644$
$\theta_{23}(^\circ)$	$42.3^{+3.0}_{-1.6}$	$38.2 \rightarrow 53.3$	$49.5^{+1.5}_{-2.2}$	$38.6 \rightarrow 53.3$
$\sin^2\theta_{13}$	$0.0218^{+0.0010}_{-0.0010}$	$0.0186 \rightarrow 0.0250$	$0.0219^{+0.0011}_{-0.0010}$	$0.0188 \rightarrow 0.0251$
$\theta_{13}(^\circ)$	$8.50^{+0.20}_{-0.21}$	$7.85 \rightarrow 9.10$	$8.51^{+0.20}_{-0.21}$	$7.87 \rightarrow 9.11$
$\delta_{CP}(^\circ)$	306^{+39}_{-70}	$0 \rightarrow 360$	254^{+63}_{-62}	$0 \rightarrow 360$
$\Delta m^2_{21}(10^{-5}eV^2)$	$7.50^{+0.19}_{-0.17}$	$7.02 \rightarrow 8.09$	$7.50^{+0.19}_{-0.17}$	$7.02 \rightarrow 8.09$
$\Delta m^2_{3l}(10^{-3}eV^2)$	$+2.457^{+0.047}_{-0.047}$	$+2.317 \rightarrow +2.607$	$-2.449^{+0.048}_{-0.047}$	$-2.590 \rightarrow 2.307$

Table 2.2: *Recent best-fit and 3σrange of the oscillation parameters. . Here, $l = 1$ for Normal Hierarchy (NH) and $l = 2$ for Inverted Hierarchy (IH). This table has been taken from reference [31].*

have been done from the combined analysis of KamLAND $\overline{\nu}_e$ and solar neutrino experiment like Chlorine, Gallex/GNO, SAGE, SNO, Borexino, four phases of Super Kamiokande data

whereas the atmospheric neutrino oscillation parameters (Δm^2_{31}, $\sin^2\theta_{23}$) have been measured from the Super-Kamiokande (SK) atmospheric, T2K, MINOS and other atmospheric neutrino experiment's data. Results from the ν_e appearance events in T2K and MINOS along with the data from Daya-Bay, RENO, Double Chooz have provided a clear indication of non-zero θ_{13}. The Dirac phase has not been measured accurately yet.

Over the past few decades several neutrino physics experiments have produced very exciting results. Still there are several open challenges in neutrino physics which require experiments with higher capability and sensitivity. The major challenges for neutrino oscillation experiments includes

- Determination of neutrino mass hierarchy.
- More precise measurement of the oscillation parameters specially θ_{23} and δ_{CP}
- Probing of CP violation in the leptonic sector, analogous to the quark sector.

Apart from these challenges there are several other open problems in neutrino physics like

- The mass generation mechanism of neutrinos.
- Are neutrinos Dirac or Majorana particles ?
- Absolute mass scale of neutrinos.
- Detection of relic neutrinos.
- Are there more than 3 kinds of neutrinos ?

The Iron Calorimeter (ICAL) experiment in the India based Neutrino Observatory is an upcoming atmospheric neutrino experiment whose prime aim will be to determine the neutrino mass hierarchy. Till now we know that there are three mass eigen states (ν_1 of mass m_1, ν_2 of mass m_2 and ν_3 of mass m_3) of neutrinos. The oscillation experiments can determine the mass squared difference of these states as the oscillation probability depends on the mass squared

difference term. The magnitude and sign of Δm^2_{21} is known, however in case of Δm^2_{31} (or, Δm^2_{32}) only the magnitude is known. This leads to two possible arrangements of the mass states - i) $m_3 > m_2 > m_1$, known as Normal Hierarchy (NH), or ii) $m_2 > m_1 > m_3$, known as Inverted Hierarchy (IH), as shown in Figure 2.7. The ICAL experiment will also study the matter effects

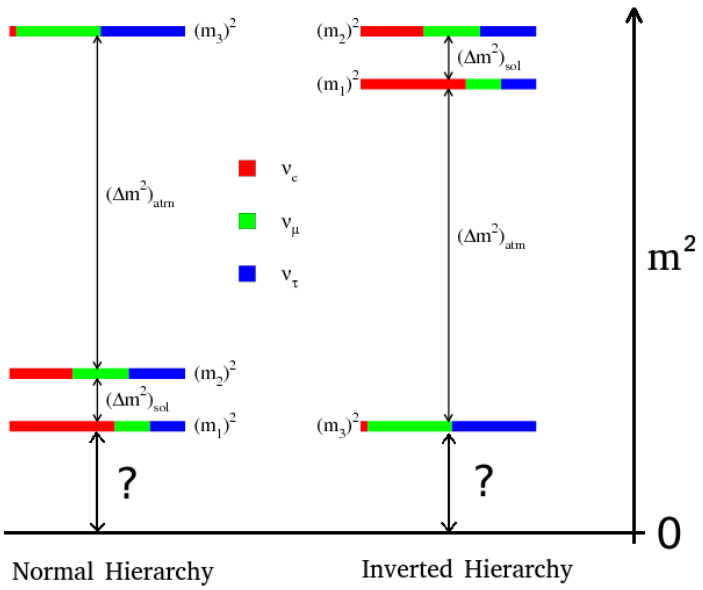

Figure 2.7: *[Colour online] Two possible arrangements of the neutrino mass eigenstates, normal hierarchy (left) and inverted hierarchy (right). The coloured bands signify the respective contributions of the flavour components in the mass eigen states.*

in neutrino oscillation. The ICAL detector, its physics motivations and configuration will be discussed in the following chapters.

2.5 Outline of this thesis work

In order to understand neutrinos, several experiments have been operational for over past few decades like SK, ICE CUBE, Daya - Bay, RENO etc. and several experiments will be coming in near future like INO-ICAL, Hyper-Kamiokande, DUNE etc. All these experiments will take us to the mysterious world of neutrinos. Motivated by what neutrinos can do, this thesis mainly focuses on the simulation study of neutrino oscillation of atmospheric neutrinos passing

through the Earth and related detector development for the INO-ICAL experiment. The thesis is organized as follows :-

Chapter 3 describes about the upcoming Iron Calorimeter experiment in the India based neutrino Observatory, its physics motivation, design and about the active detector elements of ICAL which are Resistive Plate Chambers.

Chapter 4 describes our study about probing the matter density profile of the inner structure of the Earth with atmospheric neutrinos and INO-ICAL.

In chapter 5 the details of Resistive Plate Chamber (RPC) have been discussed including its history of evolution, working principle, operational choices and applications. RPCs will be the active detector element in the INO-ICAL experiment.

Chapter 6 describes about the detailed development of large sized oil-free bakelite RPC that might be used in the INO-ICAL experiment. Failures and successes on the way of development have been addressed along with its various test results.

In chapter 7 we have discussed about a possible societal application of Multi-gap Resistive Plate Chamber (MRPC). MRPC may be a possible replacement in TOF-PET imaging. The details of detector development for this purpose and various test results have been reported.

Chapter 8 is the summary of the thesis and its main conclusions.

Bibliography

[1] Hitoshi Murayama, *The origin of neutrino mass*, *Physics World*, **15**, (2002), 5.

[2] **https://masterclass.icecube.wisc.edu/en/learn/detecting-neutrinos**

[3] Pauli W., *Neutrino Physics*, *Second Edition, Edited by Klaus Winter*, **Cambridge University Press**, (2000), 1-22.

[4] Fermi E., *Ricerca Scientifica*, **2**, (1933), 12.

[5] Perrin F., *Comptes Rendues*, **197**, (1933), 1625.

[6] H. Bethe, R. Peierls, *The "neutrino"*, *Nature*, **133**, (1934), 532.

[7] Cowan Clyde L. Jr. and Frederick Reines, *Search for Antineutrino Interaction with Deuterons*, *Phys. Rev.*, **107**, (1957), 1069.

[8] Reines F., *The neutrino: from poltergeist to particle,Rev. Mod. Phys.*, **68**, (1996), 317.

[9] Danby G. et. al., *Observation of High-Energy Neutrino Reactions and the Existence of Two Kinds of Neutrinos*, *Phys. Rev. Lett.*, **9**, (1962), 36.

[10] Lee T. D and Yang C. N, *Question of Parity Conservation in Weak Interactions*, *Phys. Rev.*, **104**, (1956), 254.

[11] Wu C. S, *Experimental Test of Parity Conservation in Beta Decay*, *Phys. Rev.*, **105**, (1957), 1413.

[12] Guinti C, Kim chung W, *Fundamentals of Neutrino Physics and Astrophysics*, **Oxford University Press**.

[13] Lande K. et. al., *Solar neutrino observations with the Homestake ^{37}Cl detector*, *AIP Conf. Proc.*, **243**, (1992), 1122.

[14] Cleveland Bruce T. et. al., *Measurement of the Solar Electron Neutrino Flux with the Homestake Chlorine Detector*, *The Astrophysical Journal*, **499**, (1998), 505 - 526.

[15] Bahcall John N and Aldo M. Serenelli, *New solar opacities, abundances, helioseismology, and neutrino fluxes*, *Astrophys. J.*, **621**, (2001), 85 - 88.

[16] Bahcall John N, Serenelli1 Aldo M, Basu Sarbani, *New Solar Opacities, Abundances, Helioseismology, and Neutrino Fluxes*, *The Astrophysical Journal Letters*, **621**, (2005), 85.

[17] C. V. Achar et al., *Detection of muons produced by cosmic ray neutrinos deep underground*, *Phys. Lett.*, **18**, (1965), 196–199.

[18] C. V. Achar et al., *Observation of a non–elastic cosmic ray neutrino interaction*, *Phys. Lett.* **19**, (1965), 78–80.

[19] Reines F et al., *Evidence for High-Energy Cosmic-Ray Neutrino Interactions*, *Phys. Rev. Lett.* **15**, (1965), 429.

[20] Hirata K. et. al., *Observation of a neutrino burst from the supernova SN1987A*, *Phys. Rev. Lett.*, **58**, (1987), 1490.

[21] R. M. Bionta R. M. et. al., *Observation of a neutrino burst in coincidence with supernova 1987A in the Large Magellanic Cloud*, *Phys. Rev. Lett.*, **58**, (1987), 1494.

[22] Alekseev E. N. et. al., *Possible detection of a neutrino signal on 23 February 1987 at the Baksan underground scintillation telescope of the Institute of Nuclear Research*, *JETP Lett.*, **45**, (1987), 589.

[23] M. G. Aartsen et al., *Evidence for High-Energy Extraterrestrial Neutrinos at the IceCube Detector*, *Science* **342**, (2013), 1242856.

[24] M. G. Aartsen et al., *First observation of PeV-energy neutrinos with IceCube*, *Phys. Rev. Lett.*, **111**, (2013), 021103.

[25] M. G. Aartsen et al., *Observation of High-Energy Astrophysical Neutrinos in Three Years of IceCube Data*, *Phys. Rev. Lett.*, **113**, (2014), 101101.

[26] G. Bellini et al., *Observation of Geo-Neutrinos*, *Phys. Lett. B*, **687**, (2010), 299.

[27] G. Bellini et al., *Measurement of geo-neutrinos from 1353 days of Borexino*, *Phys.Lett. B*, **722**, (2013), 295.

[28] T. Araki et al., *Experimental investigation of geologically produced antineutrinos with KamLAND*, *Nature*, **436**, (2005), 499.

[29] B. Pontecorvo, *Sov. Phys. JETP*, **6**, (1957), 429.

[30] B. Pontecorvo, *Sov. Phys. JETP*, **7**, (1958), 172–173.

[31] Gonzalez-Garcia M. C, *Global analyses of neutrino oscillation experiments*, *Nuclear Physics B*, **908**, (2008), 199 - 217.

[32] L. Wolfenstein,*Neutrino oscillations in matter*, *Phys. Rev. D*, **17**, (1978), 2369.

[33] Q. R. Ahmad et. al., *Direct Evidence for Neutrino Flavor Transformation from Neutral-Current Interactions in the Sudbury Neutrino Observatory*, *Phys. Rev. Lett.*, **89**, (2002), 011301

[34] Mikheev S. P and Smirnov A. Y,*The MSW effect and Solar Neutrinos*, *Sov. J. Nucl.Phys.* **42**, (1985),913.

[35] Mikheev S. P and Smirnov A. Y, *Resonant amplification of ν oscillations in matter and solar-neutrino spectroscopy*, *Nuovo Cimento C*, **9**, (1986), 17.

Chapter 3

The Iron CALorimeter (ICAL) in the India based Neutrino Observatory (INO)

Neutrino physics is largely an art of learning a great deal by observing nothing.

Haim Harari

3.1 The India-based Neutrino Observatory

The Indian neutrino physics community got their attainment in 1960's with the first detection of atmospheric neutrino induced muon events in the Kolar Gold Field Experiment in Karnataka in South India [1],[2]. Two weeks later, similar discovery was made in East Rand Proprietary (ERP) mines in South Africa [3]. Discoveries like solar neutrinos, atmospheric neutrinos, neutrino oscillation have encouraged the neutrino physicists all over the world for newer neutrino detectors, long base line experiments and so on. It is in this context that Indian neutrino physics community have decided to resurrect the underground neutrino experiments in India and hence came the birth of the concept of the India based Neutrino Observatory (INO). Basically, INO

will be a multi-institutional underground neutrino laboratory which will accommodate several experiments like neutrino oscillation study using an Iron CALorimeter (ICAL), Neutrino-less Double Beta Decay (NDBD) and Dark matter searches at INO (DINO). INO will be built inside a large underground cavern with ∼1 km or more rock overburden, under Bodi West Hills near Pottipuram village, 110 km away from the city of Madurai, at 9°58´N 77 °16´E in Theni district of Tamil Nadu in southern India. The rock coverage will help to reduce the background due to cosmic muons significantly. Figure 3.1 shows a comparison of the cosmic muon flux at various undergrond experiments. It is noteworthy that the experimental site at KGF (Kolar Gold Mines) is the deepest site. This is where the detection of the atospheric neutrinos was reported for the first time. Figure 3.2 shows a schematic view of the proposed INO facility under the mountain.

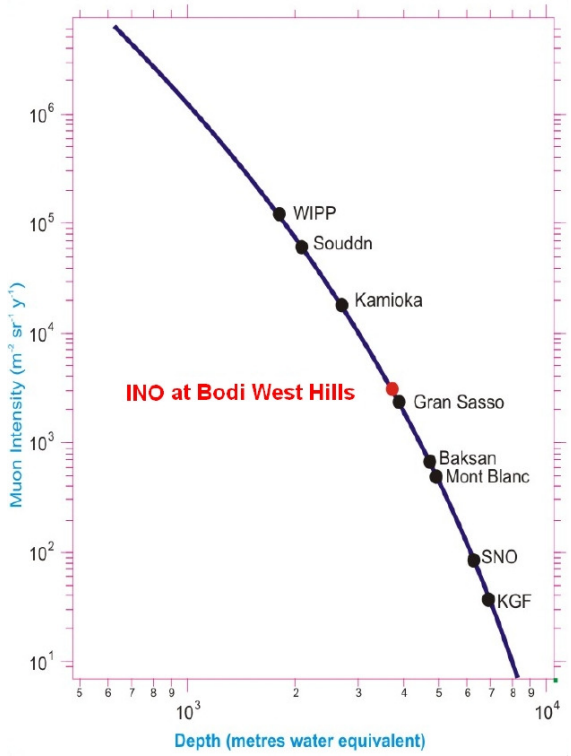

Figure 3.1: *[Colour online] The suppression in intensity of atmospheric muon flux at various underground sites, compared to the INO cavern [4].*

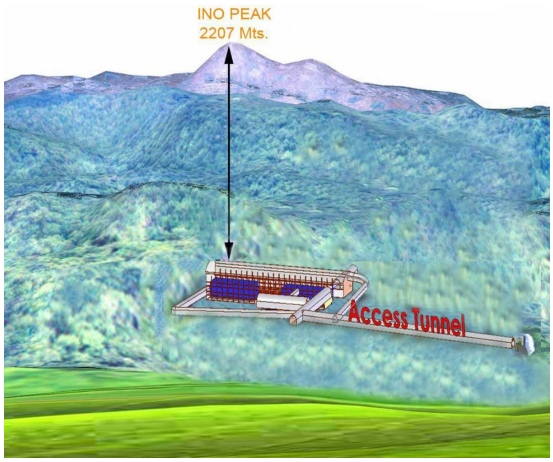

Figure 3.2: *[Colour online] Schematic view of the underground neutrino lab in India[5].*

Iron Calorimeter (ICAL) will be the key apparatus in INO. ICAL with Resistive Plate Chambers as the active detectors, will study the oscillation of atmospheric neutrinos. One of the main aims of this experiment will be to determine the neutrino mass hierarchy by studying the oscillations of the atmospheric neutrinos and anti-neutrinos passing through the earth. As ICAL will have a huge electromagnet, it will have the ability to separate the neutrinos from anti-neutrinos. Apart from this, ICAL will also be able to determine the atmospheric neutrino mixing parameters and provide hints of any non-standard interactions of neutrinos and hence new physics.

Other than the neutrino oscillation studies, INO will host several other experiments in neutrino physics like NDBD and DINO. These experiments have respective physics motivations like NDBD has the potential to figure out if neutrinos are Dirac or Majorana particles. Dark matter have always fascinated the particle physicists. As neutrinos are suitable probes for dark matter searches, experiment like DINO will be fruitful in this field.

The details of the ICAL detector and its physics motivations have been discussed in the next section.

3.2 The Magnetized Iron CALorimeter (ICAL)

3.2.1 Physics goals of the magnetized ICAL

The ICAL detector is to detect atmospheric neutrinos primarily by detection of muons produced in charged current (CC) neutrino interactions. The major physics goals of the ICAL detector are

- To reconfirm oscillation of the atmospheric neutrinos by observing the ν_μ disappearance channel,
- To study of matter effects of ν_μ and $\overline{\nu}_\mu$ interactions,
- To determine the sign of Δm^2_{31} and hence determine the neutrino mass hierarchy,
- To measure the neutrino oscillation parameters (θ_{23} and $|\Delta m^2_{31}|$) precisely,
- To measure the deviation of θ_{23} from maximality and hence resolve octant degeneracy,
- Study of Kolar events, possible identification of very-high energy neutrinos and multi-muon events.

Apart from the above mentioned oscillation related measurements, ICAL detector has the potential to study new physics like,

- Studying the Charge conjugation – parity – time (CPT) violation in the leptonic sector and hence the matter-antimatter discrepancy
- Searching for the possible existence of sterile neutrinos.
- Searching for non standard interactions (NSI) in neutrino oscillations.
- Searching for dark matter.
- Studying solar, supernova and geo-neutrinos.

- Studying tomography of the earth using natural and laboratory neutrino sources.

Charge determination is necessary to achieve most of the physics goals mentioned above. It is well known that the oscillation probability of neutrinos depends on the distance travelled by them (L), their energies (E) and the mixing parameters. To explicitly detect the oscillation pattern in the L/E spectrum of atmospheric muon neutrinos, the energy E and direction θ of the incoming neutrinos have to be accurately measured in each event. The direction of the neutrino can be estimated from the direction of the muon produced from the ν_μ charged-current interaction. Energy of a neutrino will be estimated by measuring the energy or momentum of the corrosponding muon and the hadrons produced in each event. The energy and angular resolution of the detector should therefore be crucial for L/E to be measured with an accuracy better than half of the neutrino oscillation modulation period. In order to estimate the distance traversed by the neutrino, it is necessary to establish the flight direction (up vs. down) of the muon produced from the neutrino with high efficiency. Different techniques like increase of curvature in a magnetic field, multiple scattering along the track or the measurement of timing in successive detector layers can be used to achieve this. Of these, the time-of-flight technique is the most effective and allows excellent up-down discrimination by a detector with a time resolution (σ) of 2 nano-seconds or better. Hence, the nanosecond time resolution of the RPCs ($\sim$1 nano-second) will allow the distinction between up-going and down-going muons (neutrinos).

3.2.2 The choice of detector

In order to achieve the above mentioned goals, the choice of the detector set-up is very important. The basic features of the detector should have following attributes[4]

- A large target mass to achieve a statistically significant number of neutrino interactions in a reasonable time-frame (say 5 years) for the confirmation of atmospheric neutrino oscillation. Hence, the detector should be of large volume as neutrinos are weakly interacting.

- Good energy and angular resolution so that L/E can be measured with an accuracy better than half of the modulation period.
- Identification of the electric charge of muons so as to distinguish between neutrino and anti-neutrino interactions.
- Time resolution should be ∼2 nano-seconds or better for discriminating between up-coming and down-going neutrinos.

As the detector should be of large mass, the factors like modularity and the possibility of phasing, compactness, ease of construction and the existence of other neutrino detectors around the world in the same time period should be kept in consideration. The Iron Calorimeter (ICAL) detector described in this chapter is based on all the design goals listed above. The ICAL is a sampling calorimeter consisting of magnetized iron plates interleaved with layers of position sensitive active detectors having a time resolution better than 2 nano-seconds and spatial resolution ∼1 cm. The detector has been divided into 3 modules each of about 17 kton. Such a detector with a target mass of about 50 kton has been found to be suitable to address the physics goals listed above [4]. Figure 3.3 and 3.4 shows the schematic diagrams of the ICAL and magnetic coil of the ICAL respectively.

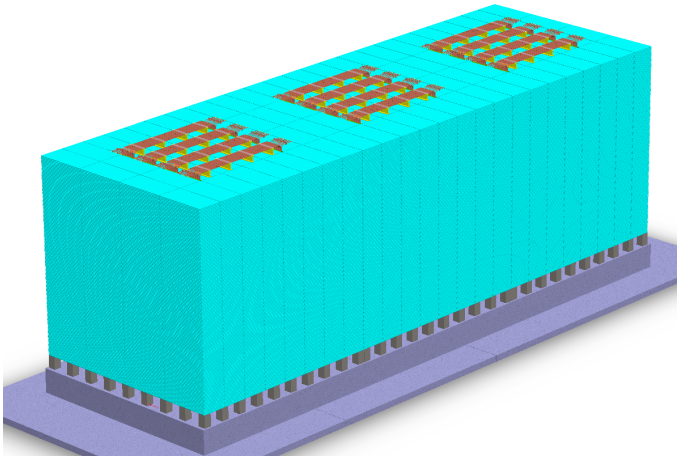

Figure 3.3: *[Colour online] Schematic view of ICAL detector.*

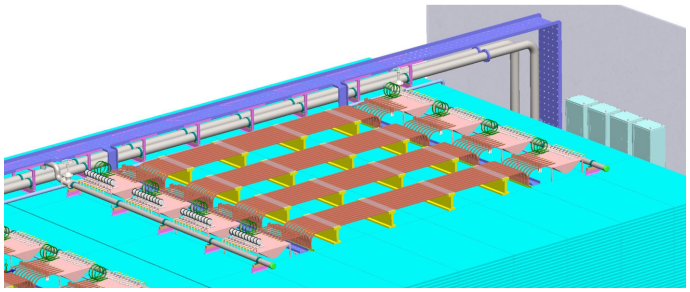

Figure 3.4: *[Colour online] Schematic view of the magnetic coil of the ICAL detector.*

ICAL will study the ν_μ and $\overline{\nu}_\mu$ by their Charged Current (CC) interactions. The CC interaction of ν_μ gives a μ^- whereas that of $\overline{\nu}_\mu$ gives a μ^+. Magnetized ICAL need to separate between μ^- and μ^+, hence ν_μ and $\overline{\nu}_\mu$ in order to study the matter effects in neutrino and anti-neutrino oscillation and hence determine the mass hierarchy. As ICAL will have layered structure, the timing in each layer through which the created muons pass will help to seperate between up-coming and down-going neutrinos. The identification of the charge of the muons will be done in the presence of magnetic field. Hence ICAL can distinguish between up-coming ν_μ, up-coming $\overline{\nu}_\mu$, down-going ν_μ and down-going $\overline{\nu}_\mu$. ICAL will consist of ∼50 kTon of low carbon iron in the form of plates, stacked one over the other. It will have 3 modules, each of dimension $\sim$ 16 m $\times$ 16 m $\times$ 14.5 m. The thickness of each plate will be 5.6 cm and gap between two layers of iron plates will be 4 cm. Figure 3.5 shows the schematic view of ICAL consisting of 3 modules each having 151 layers of iron plates (each plate 5.6 cm thick) stacked one over the other with a gap of 4 cm.

The roles of iron in ICAL are as follows :-

- It will act as the main target for neutrinos to interact to produce μ^- and μ^+ by CC interactions.
- It can be magnetized easily and hence μ^- and μ^+ can be separated.

Table 3.1 summarizes the specifications of the ICAL detector. An extensive study has been carried out for design of the ICAL magnet system and its response to the muons produced by

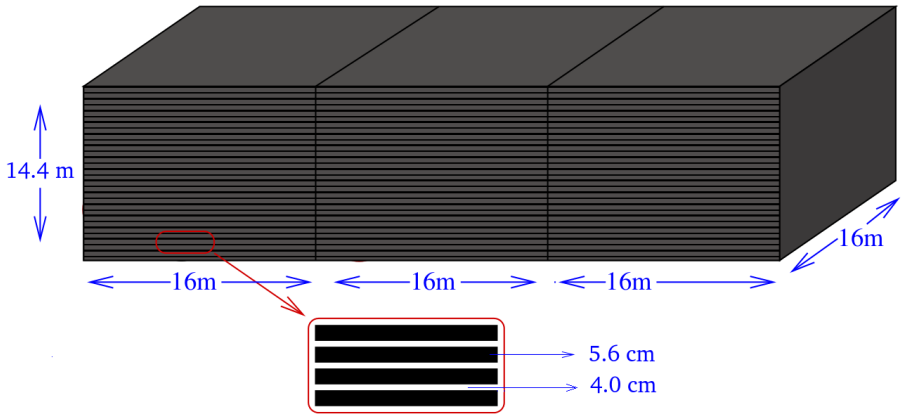

Figure 3.5: *[Colour online] Schematic view of the ICAL consisting of 3 modules each having 151 layers of iron plates stacked one over the other. The proposed thickness of each iron plate is 5.6 cm and the separation between two adjacent iron plates is 4.0 cm.*

No of modules	3
Modular dimension	16 m × 16 m × 14.4 m
Total dimension	48 m × 16 m × 14.4 m
Number of layers	151
Iron plate thickness	5.6 cm
Gap for RPC assembly	4 cm
Magnetic field	∼1.4 T

Table 3.1: Specifications of the ICAL detector.

CC interactions of neutrinos inside ICAL [6]. Figure 3.6 shows the overall distribution of the magnetic field inside iron plates having continuous slots carrying four coils (5 kA current per coil) in one module of ICAL. The direction of the arrows denote the direction of the magnetic field, while the length of the arrows indicate the field magnitude. The white circle and cross symbol show the outward and inward direction of current, respectively.

From Figure 3.6 it is clear that magnetic filed is lower at the peripheral regions of the plate as compared to the regions near the coils. Hence, all parts of the plate will not be equally effective for reconstruction of momenta and charge of the muons produced after neutrino interactions.

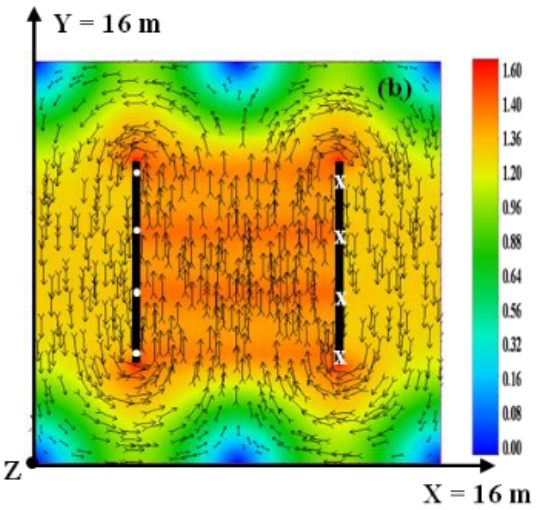

Figure 3.6: *[Colour online] Distribution of magnetic field in a module of INO-ICAL magnet having continuous slots containing four coils at 20 kA-turns [6].*

3.3 Choice of Active Detector for INO-ICAL

The total active area of ICAL will be ∼97,500 m^2. Keeping in mind the large active area, the choice of active detector for INO-ICAL should have features like low cost, can be fabricated over a large surface area, modular in construction with elements of a size suitable for mass production on a time scale consistent with the requirement that the detector be internationally competitive. Based on the physics goals of INO-ICAL, the active detectors should also have position and time resolution of ∼1 cm and ∼1 nano-second respectively. Considering all these factors the Resistive Plate Chamber (RPC) seems to be the most appropriate choice as the active detector.

Resistive Plate Chamber (RPC) is a type of gaseous detector that works on the principle of gas ionization and is made up of two high resistive plates of certain dimension seperated by a certain gap-width. The volume of separation between two plates is known as gas gap which is maintained by spacers (side and button spacers). A nearly uniform graphite / semi-conductive paint is applied on the outer surface of both the plates. Figure 3.7 shows the schematic of a typical RPC to be used in INO-ICAL experiment. The signals are read out of the RPC with

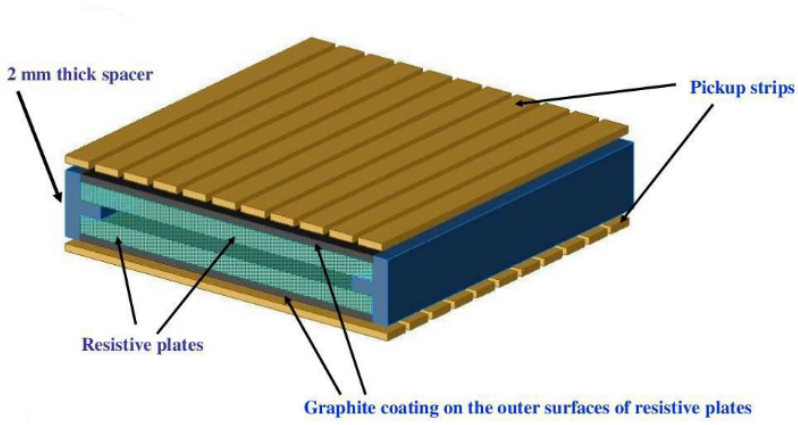

Figure 3.7: *[Colour online] Schematic of a single gap RPC to be used in the upcoming INO-ICAL experiment.*

the help of pick up strips placed on the top and bottom sides of the RPC, orthogonal to each other. The pick up panels are kept orthogonal to each other so as to get the X and Y positions of the particle falling on the RPC. INO-ICAL will deploy single gap RPCs of ∼2 mm gas gap thickness. These RPCs will track the paths of μ^- and μ^+ produced during neutrino interactions. The timing property of the RPCs will provide informations on whether a muon is up-coming or down-going. The details about RPCs have been discussed in chapter 5 and the development of RPCs for INO-ICAL have been discussed in chapter 6. Table 3.2 summarizes the specifications of the RPCs to be used in ICAL detector.

Total number of RPC units	28, 800
RPC unit dimension	195 cm × 184 cm × 2.4 cm
Gas gap of each RPC	0.2 cm
Readout strip width	2.8 cm
Number of RPCs/Road/Layer	8
Number of RPC units/Layer	192
Number of electronic channels	$\sim 3.7 \times 10^6$

Table 3.2: Specifications of the RPCs to be used in ICAL.

In order to understand the technical challenges to build the INO-ICAL, an ICAL prototype detector had been installed and operated in Variable Energy Cyclotron Centre (VECC), Kolkata,

India. The prototype detector consists of 13 layers of iron plates, each of 5 cm thick, separated by ∼5 cm gap for placing RPCs in the gap acting as the active detectors. In this prototype stack, there are single gap (2 mm gas gap) RPCs made of two types of electrodes, 8 are made of glass and 4 are made of bakelite. Figure 3.8 shows the picture of the prototype stack. The parameters of the ICAL prototype detector are as follows

- The total modular size is 2.48 m × 2.17 m × 1.3 m
- Total weight of the stack is ∼ 30 ton (∼ 0.1% of main ICAL).
- 12 layers of RPCs interleaved by iron plates of thickness 5 cm.
- There are 12 RPCs - 8 glass and 4 bakelite. Each RPC is of dimension 1 m × 1 m with a gas gap of 0.2 cm. The operating voltage for glass and bakelite RPCs is 9.5 kV and 8.0 kV respectively.
- Glass and bakelite RPCs were operated in avalanche and streamer mode respectively using respective gas mixing systems.
- Magnetic field is ∼1.5 Tesla with 500 AT (Ampere Turn) current.
- There are total 768 electronic channels (∼0.02% of main ICAL).

3.4 Performance Studies of Neutrino Interaction and Oscillation with INO-ICAL

The cosmic rays reaching the earth's surface mostly consist of μ^+, μ^-, ν_μ. $\overline{\nu}_\mu$. ν_e. $\overline{\nu}_e$ etc. For detection and studies of atmospheric neutrinos in INO-ICAL, these μ^+ and μ^- act as background. Going underground with a rock overburden helps to eliminate these backgrounds. Upcoming INO-ICAL will be sensitive to ν_μ and $\overline{\nu}_\mu$ induced Charged Current (CC) events of atmospheric neutrinos interacting with the iron plates of the ICAL. The energy of atmospheric

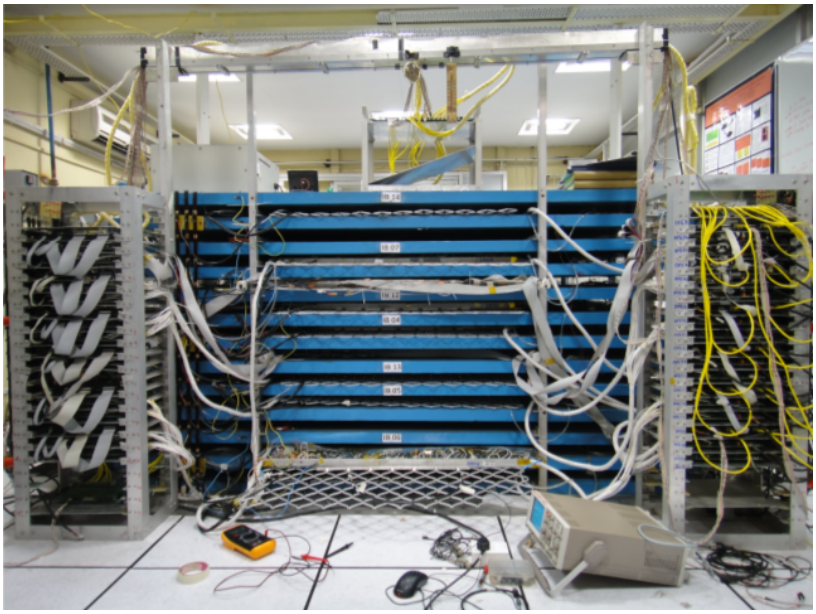

Figure 3.8: *[Colour online] The INO-ICAL prototype stack at VECC, Kolkata.*

neutrinos varies from $\sim 10^6$ eV to $\sim 10^{15}$ eV with maximum flux at $\sim 10^{12}$ eV. Figure 3.9 and 3.10 shows the CC interaction cross sections of ν_μ and $\overline{\nu}_\mu$. It is clearly seen from both the figures that atmospheric ν_μ and $\overline{\nu}_\mu$ will interact with the iron target in the ICAL mostly through quasi-elastic (QE) process at sub-GeV neutrino energy region. Resonance Scattering (RS) and Deep

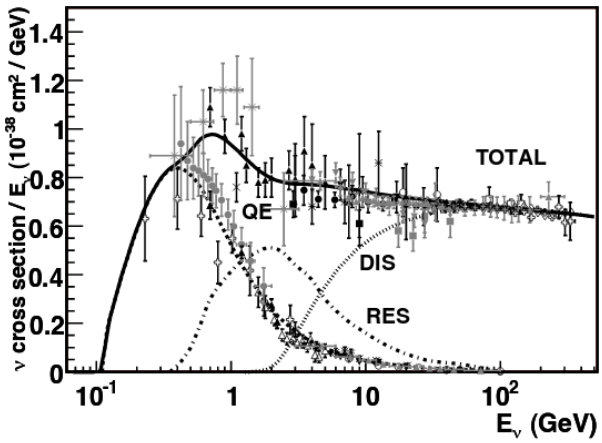

Figure 3.9: *[Colour online] The cross sections of various CC induced ν_μ interaction processes [7].*

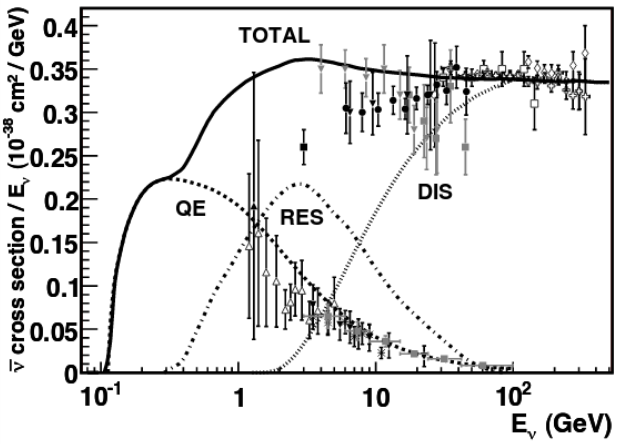

Figure 3.10: *[Colour online] The cross sections of various CC induced $\overline{\nu}_\mu$ interaction processes [7].*

Inelastic Scattering (DIS) processes will also contribute significantly and their contributions increase with increase in the neutrino energy. At few tens of GeV of neutrino energy, DIS completely dominates. There is a negligible probability of diffractive and coherent processes playing their roles. The ICAL detector will be most sensitive to the atmospheric muon neutrinos in the energy range 1 – 10 GeV. Typically, a 1 GeV muon generated from ν_μ or $\overline{\nu}_\mu$ interactions with ICAL, can pass through 5 - 12 RPC layers of the INO-ICAL depending upon the angle of incidence[8] whereas the electrons or positrons generated from ν_e or $\overline{\nu}_e$ interactions will hardly cross a few layers. Hence, a suitable selection criterion on the number of layers crossed by the charged particles can help to remove the ν_e or $\overline{\nu}_e$ events. The atmospheric neutrino flux provides a wide spectrum in the neutrino energy and the ICAL structure will enable it to be sensitive to a broad range of the path length (L) for the neutrinos penetrating through the Earth. These features would be very helpful to study the atmospheric neutrino oscillation and also the the matter effects on neutrino oscillation and hence the **neutrino mass hierarchy** as the neutrinos and the anti-neutrinos experience different matter effects while propagating through matter (for the case of ICAL, it will be the Earth). The neutrino oscillation depends on the energy, path length and also on the density of the matter through which it passes. As the inner structure of the Earth has a wide range of density variations, the neutrinos passing through the Earth

experience varying oscillation. The atmospheric neutrinos passing through the core of the earth and reaching INO-ICAL will experience dissimilar oscillations with respect to the ones passing only through the mantle or crust of the Earth. Hence, studying the oscillation of the neutrinos passing through the Earth may help us to understand the density profile of the inner structure of the Earth. As INO-ICAL will be sensitive to the broad range of path lengths of the neutrinos passing through the Earth, it will be possible to study the oscillations of the neutrinos passing through the core, mantle and crust separately. The next chapter will discuss the details about this study.

3.5 Summary

INO is an upcoming facility in India to study atmospheric neutrinos. It will host several neutrino experiments like ICAL, NDBD, DINO. ICAL will be the prime experiment in INO whose aim will be to study oscillation phenomenon in atmospheric neutrinos and determine the mass hierarchy. The major advantage of ICAL over several other neutrino experiments is seperation between μ^- and μ^+ events due to the ν_μ and $\overline{\nu}_\mu$ interaction with iron in ICAL. ICAL will be a tracking calorimeter with magnetised iron plates stacked one over the other. RPCs will be the active detectors to get the hit points of the passing μ^- and μ^+. the RPCs will be single gap with electrodes made of either glass or bakelite. The RPCs will be inserted between the iron plates. The time information obtained from the respective layers of RPCs will help to distinguish between up-coing and down-going events whereas the bending of the muon tracks in presence of magnetic field will distinguish between ν_μ and $\overline{\nu}_\mu$. A protopye of INO-ICAL had been operated in VECC, Kolkata which is $\sim$1000 times smaller than the actual ICAL.

Bibliography

[1] C. V. Achar et al., *Detection of muons produced by cosmic ray neutrinos deep underground*, *Phys. Lett.*, **18**, (1965), 196–199.

[2] C. V. Achar et al., *Observation of a non–elastic cosmic ray neutrino interaction*, *Phys. Lett.* **19**, (1965), 78–80.

[3] F. Reines et al., *Evidence for high energy cosmic-ray neutrino interactions*,*Phys. Rev. Lett.* **15**, (1965), 429.

[4] INO Project Report, INO/2006/01, `http://www.ino.tifr.res.in/ino//OpenReports/INOReport.pdf`

[5] `http://www.ino.tifr.res.in/ino/gallery/Schematic view of the Underground neutrino lab under a mountain.JPG`

[6] Shiba P. Behera et al., *Simulation Studies for Electromagnetic Design of INO ICAL Magnet and Its Response to Muons'*, *IEEE Transactions on Magnetics*, **51**, (2015), 2.

[7] J. A. Formaggio and G. P. Zeller, *From eV to EeV: Neutrino Cross Sections Across Energy Scales*, *Rev. Mod. Phys.*, **84**, (2012), 1307.

[8] A. Chatterjee et. al., *A Simulations Study of the Muon Response of the Iron Calorimeter Detector at the India-based Neutrino Observatory*, *Journal of Instrumentation*, **JINST 9, P07001** (2014).

Chapter 4

Probing the Earth Matter Density through INO-ICAL

Without experimentalists, theorists tend to drift. Without theorists, experimentalists tend to falter.

T.D. Lee

4.1 Introduction

The Earth has many mysteries, may it be the life on it or its ecology or its structure . Over many centuries, mankind has tried to solve the mysteries and succeeded in many of them. Among those, the inner structure of the earth has always been interesting and exciting as it may help us to understand the dynamics of the core and mantle, the gravitational field, the mechanism of the geomagnetic dynamo, the bulk composition of the Earth etc. The inner structure of the earth played a vital role for the evolution of life and continues to do so to sustain life. Over the centuries, mankind has tried to know about the inner structure of the earth by studying meteorites, rocks originating from depth, from geomagnetic data, geodynamical data, solid state theory, high temperature-pressure experimental results and so on. But most of the knowledge

we have about the internal structure of the Earth and the physical properties of its different layers come from the data we obtain from seismic waves (precisely from the velocities of P-waves, S-waves and K-waves). Several models have been proposed about the inner structure. Among those the most widely accepted model is Preliminary Reference Earth Model (PREM) [1]. Neutrinos may also prove to be an essential tool to probe the density profile of the inner structure of the earth. Neutrino oscillation tomography, neutrino absorption tomography and neutrino diffraction are the proposed phenomena to study the inner structure of the earth. Neutrino oscillation tomography exploits the matter effects on neutrino oscillation specially the matter effects due to θ_{13}. Neutrino beams from accelerators, solar neutrinos [2],[3],[4],[5] and supernova neutrinos [6], [7] have been very useful to study the matter effects. Neutrino absorption topography uses the information of absorption of very high energy neutrinos to explore the composition of the earth [8]. Neutrino diffraction is based on the fact that neutrinos may undergo coherent scattering due to the presence of crystalline matter inside the earth[9]. Studying the diffraction pattern may help to know the inner structure.

Atmospheric neutrinos may prove themselves to be a suitable tool to probe the matter density profile of the earth as they have a wide range of energy and also can provide a wide range of baseline through the earth. As resonant effects are very sensitive to the density of the matter through which the neutrinos traverse, neutrino oscillation tomography with atmospheric neutrinos of energies in GeV range may be exploited. The resonant effects in the propagation of GeV atmospheric neutrinos (anti-neutrinos) through the earth significantly affect the sub-leading $\nu_\mu \to \nu_e$ and $\nu_e \to \nu_\mu$ ($\overline{\nu}_\mu \to \overline{\nu}_e$ and $\overline{\nu}_e \to \overline{\nu}_\mu$) transitions that can be explored. When atmospheric neutrinos pass through deep inside the earth, MSW effect, resonant effect etc. could show up. These effects are well known since last few decades and they have major physics potentials which can be studied in magnetized iron calorimeter detector like INO-ICAL, liquid argon detectors water-$\check{C}$erenkov detectors etc.

In this thesis a model-based study of the sensitivity of INO-ICAL to the density of the core of the earth by using a neutrino generator (GENIE), atmospheric neutrino flux (HONDA flux

at Theni, the site of INO) and ICAL detector response has been done. In this work, the ratio of the number of "the up-coming neutrinos" and "the down-going neutrinos" measured at a time interval v/s "L/E", where "L" is the distance traveled by the neutrinos and "E" is the energy of the corresponding neutrinos, has been used as a tool.

4.2 Matter Density Profile of the Earth

The shape of our Earth is Oblate Spheroid, flattened at the poles and bulges at the equator. The internal structure of the earth is divided into three main approximately spherical concentric shells - the core, the mantle and the crust. The core further consists of inner core and outer core. Inner core is highly dense solid shell and the outer core is liquid, both consisting of an alloy of iron (major content) and nickel with a small mixture of lighter elements. The density of these internal structures varies quite significantly from each other with discontinuity in density at the interfaces. During several years, the most widely used radially symmetric model of the earth's interior structure has been the Preliminary Reference Earth Model (PREM). This model is mainly based on astronomic-geodetic data, free oscillation and long-period surface wave data and data from travel times of body waves. In PREM, the density, velocity of S and P-waves for the following principle regions within the earth have been considered

- Ocean layer
- Upper and lower crust
- Region above the low velocity zone (LID)
- Low velocity zone (LVZ).
- Region between low velocity zone and 400 km discontinuity
- Transition zone spanning the region between the 400 and 670 km discontinuities.
- Lower mantle.

- Outer core
- Inner core

The lower mantle and the transition zone has been further divided into three concentric sub-shells. Table 4.2 lists out the matter density of the different inner shells of the earth as a function of normalized radius x = R/R$_E$, with R_E being the radius of earth (6371 km) according to PREM.

Radius (km)	**Region**	**Density (g/cm^3)**
0 - 1221.5	Inner Core	13.0885 - 8.8381x^2
1221.5 - 3480.0	Outer Core	12.5815 - 1.2638x - 3.642x^2 - 5.5281x^3
3480.0 - 5701.0	Mantle	7.9565 - 6.4761x + 5.5283x^2 - 3.0807x^3
5701.0 - 5771.0	Mantle	5.3197 - 1.4836x
5771.0 - 5971.0	Mantle	11.2494 - 8.0298x
5971.0 - 6151.0	Mantle	7.1089 - 3.8045x
6151.0 - 6346.0	Mantle	2.6910 + 0.6924x
6346.0 - 6356.0	Oceanic Crust	2.900
6356.0 - 6371.0	Continental Crust	2.600

Table 4.1: *Density Profile of the Earth as a function of normalized radius $x = R/R_E$ according to PREM [10].*

Figure 4.1 shows the density profile of the inner structure of the earth as a function of its radial distance. From this figure we can see that there are discontinuities in the density at the interfaces of the sub-shells. The core has average density (ρ_{core}) of 11.83 g/cm^3 and electron fraction (Y_e^{core}) of 0.466, while the mantle has average density (ρ_{mantle}) of 4.66 g/cm^3 and electron fraction (Y_e^{mantle}) of 0.494. The electron fraction is defined as

$$Y_e = \frac{N_p}{N_p + N_n} \tag{4.1}$$

where, where N_p and N_n are, respectively, the numbers of protons and neutrons.

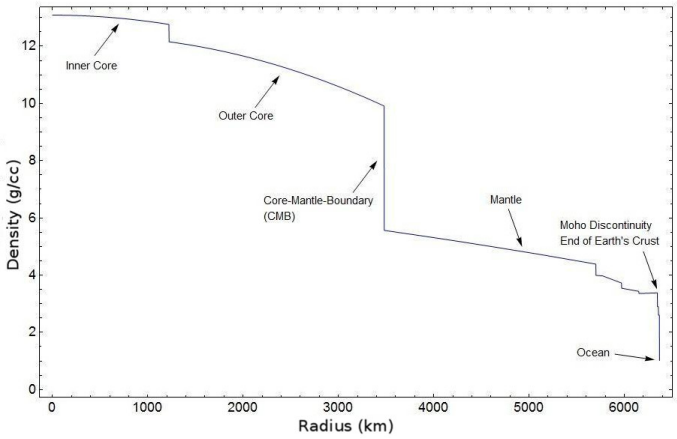

Figure 4.1: *[Colour online] Density profile of the various inner sub-shells of the earth.*

4.3 Probing the Matter Density Profile of the Earth through INO-ICAL

It is a very well known fact that the presence of matter affects the neutrino oscillation. Neutrinos of electron flavours are directly affected when they travel through the Earth matter. However, this effect gets induced into the other neutrino flavors indirectly through mixing cum oscillation phenomenon. The neutrinos with muonic flavours are affected either by mixing between the electron like flavor and the third physical neutrino or by sub-dominant oscillations between electron like and muon like neutrino flavors, driven by Δm^2_{21} [11]. For three flavour neutrinos, with One Mass Scale Dominant (OMSD) approximation (neglecting the smaller mass-squared difference, Δm^2_{21} with respect to Δm^2_{31}) the oscillation probabilities ($P^m_{\nu_\mu \to \nu_\mu}$, $P^m_{\nu_\mu \to \nu_e}$) for neutrinos

travelling through matter is given by [11], [19]

$$P^m_{\nu_\mu\to\nu_\mu} = 1 - cos^2\vartheta^m_{13}sin^2 2\vartheta^m_{23}sin^2\left[1.27\left(\frac{\Delta m^2_{31} + A + (\Delta m^2_{31})^m}{2}\right)\frac{L}{E}\right] - sin^2\vartheta^m_{13}sin^2 2\vartheta^m_{23}sin^2\left[1.27\left(\frac{\Delta m^2_{31} + A - (\Delta m^2_{31})^m}{2}\right)\frac{L}{E}\right] - sin^4\vartheta_{23}sin^2 2\vartheta^m_{13}sin^2\left[1.27(\Delta m^2_{31})^m\frac{L}{E}\right] \quad (4.2)$$

$$P^m_{\nu_\mu\to\nu_e} = sin^2\vartheta_{23}sin^2 2\vartheta^m_{13}sin^2\left[1.27(\Delta m^2_{31})^m\frac{L}{E}\right] \quad (4.3)$$

As the OMSD analytical expressions are insensitive to δ_{CP} and the probability for the time-reversed transition $P^m_{\nu_\mu\to\nu_e}$ is same as $P^m_{\nu_e\to\nu_\mu}$ with the replacement $\delta_{CP} \to -\delta_{CP}$, hence $P^m_{\nu_\mu\to\nu_e}$ = $P^m_{\nu_e\to\nu_\mu}$ [8].

In this work we have used **nuosc++** which is a library for calculating three neutrino (anti-neutrino) oscillation probabilities with and with out matter effects as well as the possibility for a nonzero Dirac CP phase. **nuosc++** calculates the oscillation probabilities by solving the evolution equation

$$\frac{d\nu}{dx} = \left[\left(\frac{-i}{2E}\right)\left((U\mathcal{M}^2U^\dagger - iV\right)\right]\nu(x) \quad (4.4)$$

where, U is the mixing matrix (potentially complex), $\mathcal{M}^2$ is diag(0, Δm^2_{21}, Δm^2_{31}) and V is diag(A_{CC}, 0, 0) which is the matter effect term. In the case of anti neutrinos the sign of A_{CC} and of the CP phase are inverted. Figure 4.2 shows the oscillation probabilities obtained from **nuosc++** for $\nu_\mu \to \nu_\mu$, $\overline{\nu}_\mu \to \overline{\nu}_\mu$, $\nu_e \to \nu_\mu$ and $\overline{\nu}_e \to \overline{\nu}_\mu$ as a function of energy for the neutrinos and anti-neutrinos travelling through the Earth with a baseline of 12740 km for both normal and inverted hierarchies. Table lists the values of different oscillation parameters used in nuosc++.

It is clear from Figure 4.2 that the oscillation probabilities for $\nu_\mu \to \nu_\mu$ and $\overline{\nu}_\mu \to \overline{\nu}_\mu$ channel

Oscillation parameter	Value
Δm^2_{21}	$7.5 \times 10^{-5} eV^2$
Δm^2_{31}	$2.44 \times 10^{-3} eV^2$
ϑ_{12}	31.7°
ϑ_{23}	45.0°
ϑ_{13}	8.878°
$\sin^2 2\vartheta_{12}$	0.846
$\sin^2 2\vartheta_{23}$	1.0
$\sin^2 2\vartheta_{13}$	0.093
δ_{CP}	0

Table 4.2: *The values of the oscillation parameters used to calculate the transition probabilities ny nuosc++. For inverted hierarchy,* $\Delta m^2_{31} \rightarrow -\Delta m^2 31$.

in the Earth matter for Inverted Hierarchy (IH) deviates slightly from Normal Hierarchy (NH). The oscillation probabilities in $\nu_e \rightarrow \nu_\mu$ channel for NH rises over the corresponding values of IH and in $\overline{\nu}_e \rightarrow \overline{\nu}_\mu$ channel, IH rises over NH. This is due to the fact that electron neutrinos are more affected by the presence of matter which has been well explained in chapter 9 in reference [12].

Atmospheric neutrinos are generated at ∼15 km above the Earth's surface by the interaction of primary cosmic rays with the nuclei in upper atmosphere. The oscillation probabilities of neutrinos depend on the length they travel. The length traveled by the atmospheric neutrinos before they reach INO-ICAL has been calculated by the following formulae.

$$L_{down} = \sqrt{(R + L_0)^2 - (Rsin\theta_z)^2} - Rcos\theta_z \tag{4.5}$$

$$L_{up} = \sqrt{(R + L_0)^2 - \{Rsin(\pi - \theta_z)\}^2} - Rcos(\pi - \theta_z) \tag{4.6}$$

where,

R is the radius of the Earth.

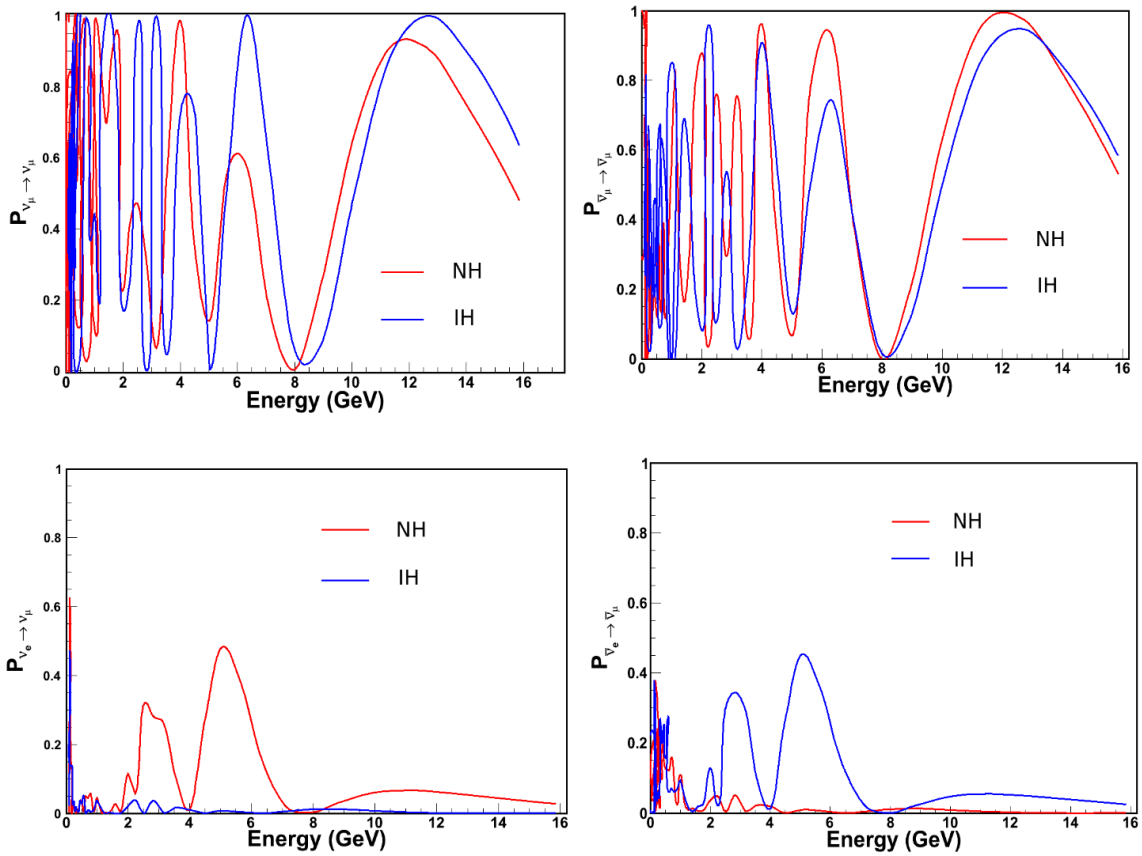

Figure 4.2: *[Colour online] The oscillation probabilities for $\nu_\mu \rightarrow \nu_\mu$ (top left), $\overline{\nu}_\mu \rightarrow \overline{\nu}_\mu$ (top right), $\nu_e \rightarrow \nu_\mu$ (bottom left) and $\overline{\nu}_e \rightarrow \overline{\nu}_\mu$ (bottom right) channels as a function of energy for the neutrinos and anti-neutrinos travelling through the Earth with a baseline of 12740 km for both normal and inverted hierarchies. NH stands for Normal Hierarchy and IH stands for Inverted Hierarchy. The matter density profile of the Earth is according to PREM.*

$L_0 = 15$ km, is the distance from the Earth's surface where atmospheric neutrinos are created.

θ_z is the zenith angle of the incoming neutrino.

L_{down} and L_{up} are the distance traveled by the down-going and up-coming neutrinos (as shown in Figure 4.3) respectively.

The replacement of the zenith angle, $\theta_z \longleftrightarrow (\pi - \theta_z)$, effectively changes the sign of the second term in Equation 4.5, thus relating a down-going neutrino to an up-coming one. We define the reference path length L for down-going neutrinos to be that of the associated up-coming neutrino with zenith angle $(\pi - \theta_z)$ so that the range of L/E remains the same for

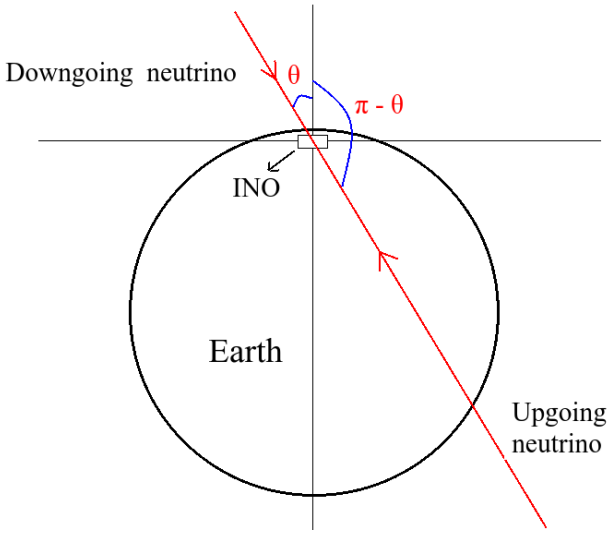

Figure 4.3: *[Colour online] Direction of the atmospheric neutrinos reaching the INO-ICAL.*

up-coming and down-going neutrinos. The ratio of up-coming to down-going neutrinos is a useful measure of neutrino oscillations. The up-coming fluxes corresponding to the down-going fluxes reaching a detector are expected to be similar in absence of oscillation , especially for larger neutrino energies (E > a few GeV). Hence, the ratio is expected to be near unity. But, in presence of oscillation, the upcoming neutrino fluxes are expected to be modified resulting in a deviation of the up-down ratio from unity causing the asymmetry of the up-down fluxes. This technique gives a direct measure of the oscillation probability. In case of vacuum oscillations, the neutrino event rates are a function of L/E only whereas they become separately a function of L and E in presence of matter[15]. Let us define

$$\mathcal{R}(L/E) = \frac{\text{Up}}{\text{Down}}(L/E) = \frac{\text{No. of events from up-coming muon neutrinos (L/E)}}{\text{No. of events from down-going muon neutrinos (L/E)}}\text{[15]}. \quad (4.7)$$

On plotting this $\mathcal{R}$ as a function of L/E, a "dip"is obtained as shown in Figure 4.6. It has been observed that the position of the dip is sensitive to the effective magnitude of Δm^2_{13} while the value of the ratio at the dip is sensitive to effective $\sin^2 2\theta_{23}$ [15]. For the neutrinos traveling through matter, the effective values of the oscillation parameters change due to the matter

effects. This fact establishes the motivation of this thesis.

We know that neutrino oscillation also depends on the energy of the neutrinos. The energy range of the atmospheric neutrinos is very wide (approximately 0.1 GeV to 10^4 GeV). The numbers of the atmospheric neutrinos reaching the Earth's surface are different at different latitudes and longitudes. There are several models on the flux of the atmospheric neutrinos reaching the Earth's surface. For our work, the Honda neutrino flux [13], [14] without mountain cover and averaged over the azimuthal direction at the INO site has been used. The oscillation probabilities for $\nu_\mu \rightarrow \nu_\mu$, $\overline{\nu}_\mu \rightarrow \overline{\nu}_\mu$, $\nu_e \rightarrow \nu_\mu$ and $\overline{\nu}_e \rightarrow \overline{\nu}_\mu$ channels have been calculated for down-going neutrinos assuming that they travel through matter of constant density (average density of troposphere which is $\sim$0.001225 g/cc) with different calculated travel length (L_{down}) and energy (obtained from HONDA flux file). Similarly the transition probabilities for the above mentioned channels have been calculated for up-coming neutrinos travelling through the Earth matter profile with different L_{up} and neutrino energy. In order to probe the matter density profile of the Earth, we have taken the density profile provided by the PREM as a reference. The density profile of the core of the earth has been changed by $\pm$5%, $\pm$10%, $\pm$15% and $\pm$20% keeping the overall mass of the Earth constant and the density of the crust unchanged. Figure 4.4 shows the values of the ratio of $\rho^{new}_{mantle}/\rho^{default}_{mantle}$ for the corresponding ratio of $\rho^{new}_{core}/\rho^{default}_{core}$. A value of $\rho^{new}_{core}/\rho^{default}_{core} = 1$ represents the density profile of the Earth according to the PREM. A change in the core density is reflected by a change in the mantle density according to the equation

$$\frac{V_{core}}{V_{mantle}} = \frac{\rho^{new}_{mantle} - \rho^{default}_{mantle}}{\rho^{new}_{core} - \rho^{default}_{core}} \tag{4.8}$$

where,

V_{core} and V_{mantle} are the volume of the core and the mantle respectively.

$\rho^{default}_{core}$ and $\rho^{default}_{mantle}$ are the density of the core and the mantle respectively according to PREM.

ρ^{new}_{core} is the changed core density.

ρ^{new}_{mantle} is the changed mantle density due to the changed core density.

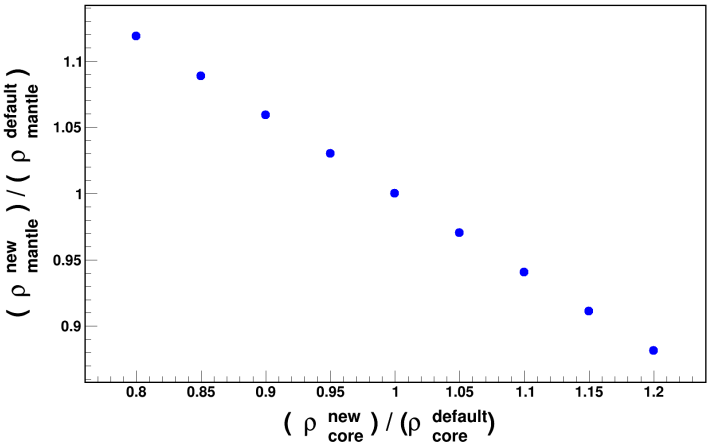

Figure 4.4: *[Colour online] Variation in the ratio of* $\rho^{new}_{mantle}/\rho^{default}_{mantle}$ *for the changed ratio of* $\rho^{new}_{core}/\rho^{default}_{core}$

In order to generate the neutrino events, we have used GENIE Neutrino Monte Carlo generator [16] and a detailed ROOT-based INO-ICAL detector geometry. Three million events were generated using the gevgen_atmo application of GENIE, for the down-going neutrinos travelling through matter of constant density (∼0.001225 g/cc), up-coming neutrinos travelling through the density profile of the Earth according to the PREM and up-coming neutrinos travelling through the changed density profile of the Earth as per Figure 4.4. For the analysis of the generated data, the angular cuts used have been listed out in table 4.3. INO-ICAL detector

Baselines	**Down-going events**	**Up-coming events**
Through the **Core**	$0^\circ \leq \theta_{down} < 30^\circ$	$150^\circ < \theta_{up} \leq 180^\circ$
Through the **Mantle**	$30^\circ \leq \theta_{down} < 85^\circ$	$95^\circ < \theta_{up} \leq 150^\circ$
All baselines	$0^\circ \leq \theta_{down} < 90^\circ$	$90^\circ < \theta_{up} \leq 180^\circ$

Table 4.3: *The angular cut values used during the analysis of the generated data. The angular values are w.r.t the zenith direction.*

parameters like energy resolution, direction resolution, muon detection efficiency, charge identification efficiency [17], [18] have been taken into account during the analysis of the generated

data. The results have been discussed in the next section.

4.4 Results and Discussion

4.4.1 The "Up/Down"ratio plots

This work aims at the observation of the deviation in the matter density profile of the core of the Earth from the predicted density profile according to PREM, by studying the oscillation in the atmospheric neutrinos (anti-neutrinos) at INO-ICAL. The ratio of up-coming neutrinos (anti-neutrinos) to the down-going neutrinos (anti-neutrinos) as a function of L/E has been chosen as an observable as the ratio tells us how much the up-coming neutrinos (anti-neutrinos) flux passing through the Earth have oscillated in comparison to the respective down-going neutrinos (anti-neutrinos) flux. For our work, we have separated the baselines which pass through the core and the mantle of the earth. Among the generated ν_μ events, $\sim$6% of them pass only through the core and $\sim$50% pass only through the mantle of the Earth. Whereas for the generated $\overline{\nu}_\mu$, $\sim$8% of them pass only through the core and $\sim$65% pass only through the mantle of the Earth. Those passing through the core see the mantle twice whereas those passing only through the mantle does not see the core at all. A plot of $Up/Down$ (Up-coming events/Down-going events) v/s $\log_{10}\{L(km)/E(GeV)\}$ for the baselines passing only through the core of the Earth will be different from those passing only through the mantle due to the change in the matter density. Figure 4.5 shows such a plot for all the baselines, Figure 4.6 shows for the baselines passing only through the core of the Earth and Figure 4.7 shows the same for all baselines passing only through the mantle of the Earth, for the density profile of the Earth according to the PREM. In Figure 4.5 and Figure 4.6 there are very clean dips at $\log_{10}(L/E) = \sim 3$ and $\sim$ 3.7 respectively. Figure 4.7 shows two clean dips at $\log_{10}(L/E) = \sim 2$ and $\sim$2.8 respectively. These dips are the effects of neutrino oscillations. The position of these dips are sensitive to the effective Δm^2_{31}, which is different for different matter densities through which neutrinos (anti-neutrinos) travel. As the densities of the core and the mantle of the Earth are different, the effective Δm^2_{31} changes

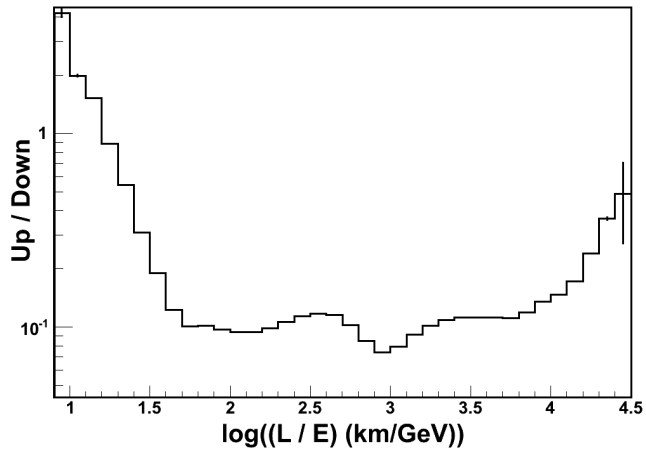

Figure 4.5: *[Colour online] The ratio of up-coming $\overline{\nu}_\mu$ to down-going $\overline{\nu}_\mu$ (as measured by using INO-ICAL detector parameters) as a function of L/E for all baselines taken together. The density profile of the Earth is according to the PREM. Each bin width along X-axis being $log_{10}(L/E) = 0.10$, where L is in km and E is in GeV.*

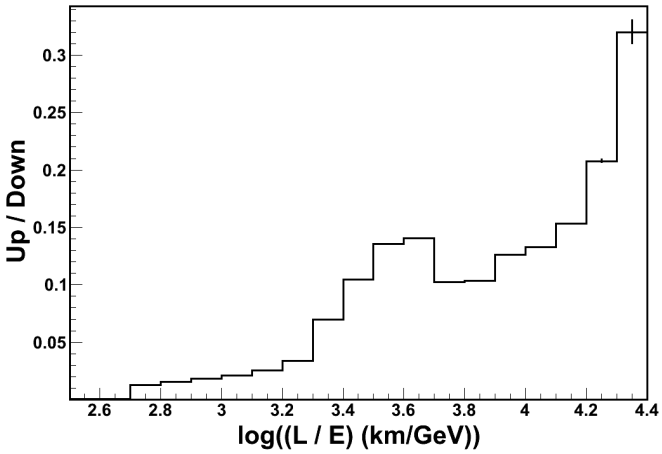

Figure 4.6: *[Colour online] The ratio of up-coming anti-neutrinos to down-going anti-neutrinos (as measured by using INO-ICAL detector parameters) as a function of L/E for baselines passing only through the core of the Earth. The density profile of the Earth is according to the PREM. Each bin width along X-axis being $log_{10}(L/E) = 0.10$, where L is in km and E is in GeV.*

for the baselines passing only through core and only through mantle.

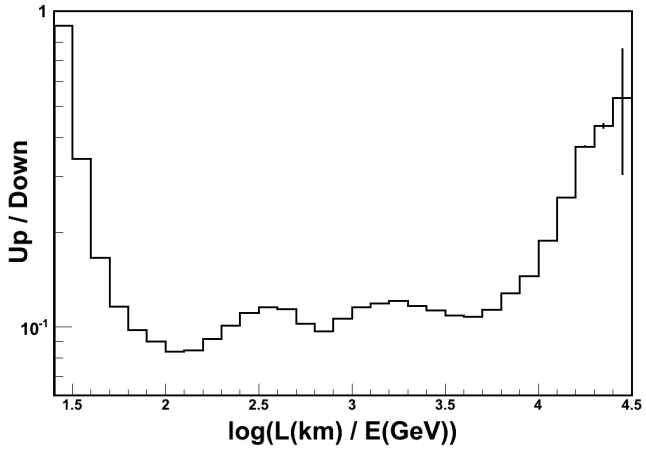

Figure 4.7: *[Colour online] The ratio of up-coming anti-neutrinos to down-going anti-neutrinos (as measured by using INO-ICAL detector parameters) as a function of L/E for baselines passing only through the mantle of the Earth. The density profile of the Earth is according to the PREM. Each bin width along X-axis being $log_{10}(L/E) = 0.10$, where L is in km and E is in GeV.*

4.4.2 Comparison of Up/Down ratio for neutrinos and anti-neutrinos passing through different baselines

The effective Δm^2_{31} and $\sin^2 2\theta_{23}$ are different for neutrinos and anti-neutrinos as they see different matter potentials, however small, when traveling through matter. This change in the

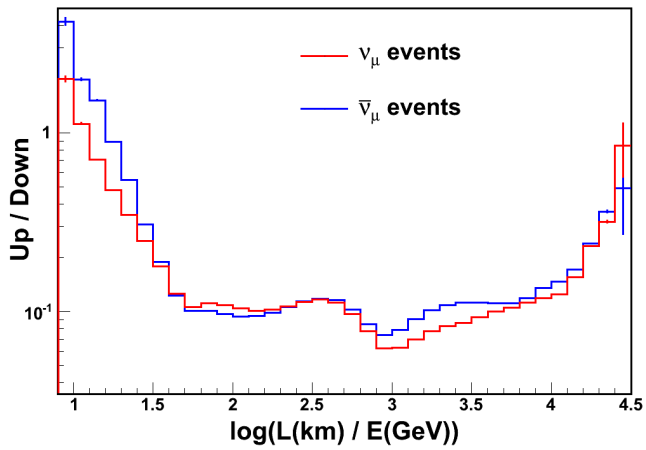

Figure 4.8: *[Colour online] Comparison of Up by down ratio for neutrino and anti-neutrino events in INO-ICAL for all baselines.*

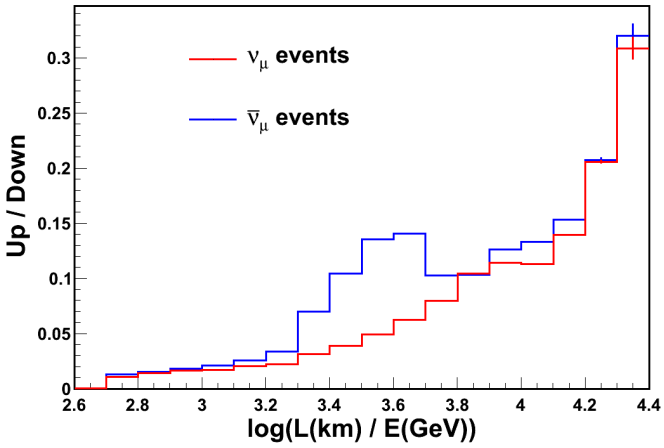

Figure 4.9: *[Colour online] Comparison of Up by down ratio for neutrino and anti-neutrino events in INO-ICAL for baselines passing through the core of the Earth only.*

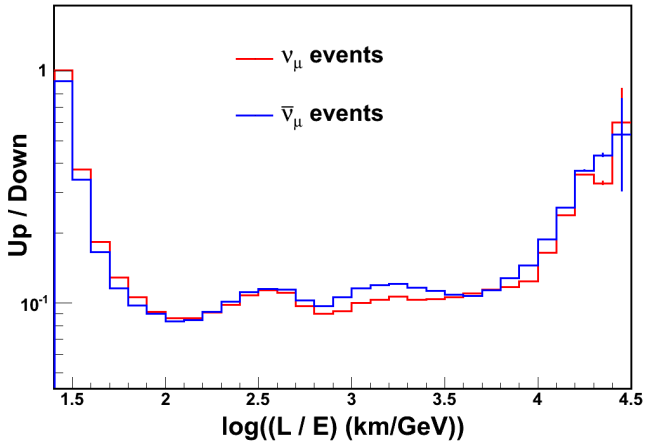

Figure 4.10: *[Colour online] Comparison of Up by down ratio for neutrino and anti-neutrino events in INO-ICAL for baselines passing through the mantle of the Earth only.*

matter potential term is reflected in the transition probabilities, effecting the Up/Down ratio, as seen in figures 4.8, 4.9 and 4.10 for neutrinos and anti-neutrinos for all baselines, baselines only through the core and baselines only through the mantle respectively. The ν_μ and $\overline{\nu}_\mu$ events corresponds to the μ^- and μ^+ events in the INO-ICAL respectively. The bin size along X-axis for all the three figures is 0.10 km/GeV. It can be seen from the figures 4.8, 4.9 and 4.10 that the position as well as the value of the Up/Down ratio are different for the ν_μ and $\overline{\nu}_\mu$ events.

This is due to the difference in interaction of neutrinos and anti-neutrinos with matter which has been discussed in section 2.3.2.

4.4.3 Comparison of Up/Down ratio for different core densities

We have analyzed each data set generated by varying the core density by ±5%, ±10%, ±15% and ±20%. The Up/Down ratio was plotted as a function of $\log_{10}$L/E for each data set and then compared with the same plot for density profile of the Earth according to PREM. Figure 4.11, 4.12 and 4.13 show the comparison for all baselines, baselines only through the core and baselines only through the mantle respectively. The bin size for all the plots are 0.10 km/GeV. The histograms on left sides of the figures correspond to ν_μ events (μ^- events) and the right side histograms correspond to $\overline{\nu}_\mu$ events (μ^+ events). The histograms at the bottom line in each of the three figures show the zoomed versions of the dips obtained. The values in the legend of the figures show the ratio of new (changed) core density to the core density according to the PREM, i.e $\rho^{new}_{core}/\rho^{PREM}_{core}$. It is very clear from figures 4.11, 4.12 and 4.13 that there is a difference in the dip values when the density of the core is changed. As discussed earlier, this difference is due to the change in the effective $\sin^2 2\theta_{23}$ due to the change in the density profile of the core and hence that of the Earth. The positions and values of these dips for ν_μ events in the INO-ICAL for all baselines, baselines passing only through the core and mantle of the Earth have been tabulated in table 4.4 and the same for $\overline{\nu}_\mu$ events in the INO-ICAL have been tabulated in table 4.5. From the bottom left histogram in Figure 4.13 and table 4.4, we can see that the position of the dip for the ν_μ events in INO-ICAL for neutrinos passing only through the mantle of the Earth changes when the density of the core is changed by ±15 % and ±20 %.

Table 4.6 summarizes the % change in the values of the dips obtained for events due to $\overline{\nu}_\mu$ and $\overline{\nu}_\mu$ reaching INO-ICAL through all baselines, baselines passing only the core and mantle of the Earth. Figure 4.14 shows the correlation between the measured dip values for ν_μ events in INO-ICAL due to atmospheric neutrinos travelling through all baselines and baselines only through the core. By knowing the respective dip values, one can predict the deviation in the density

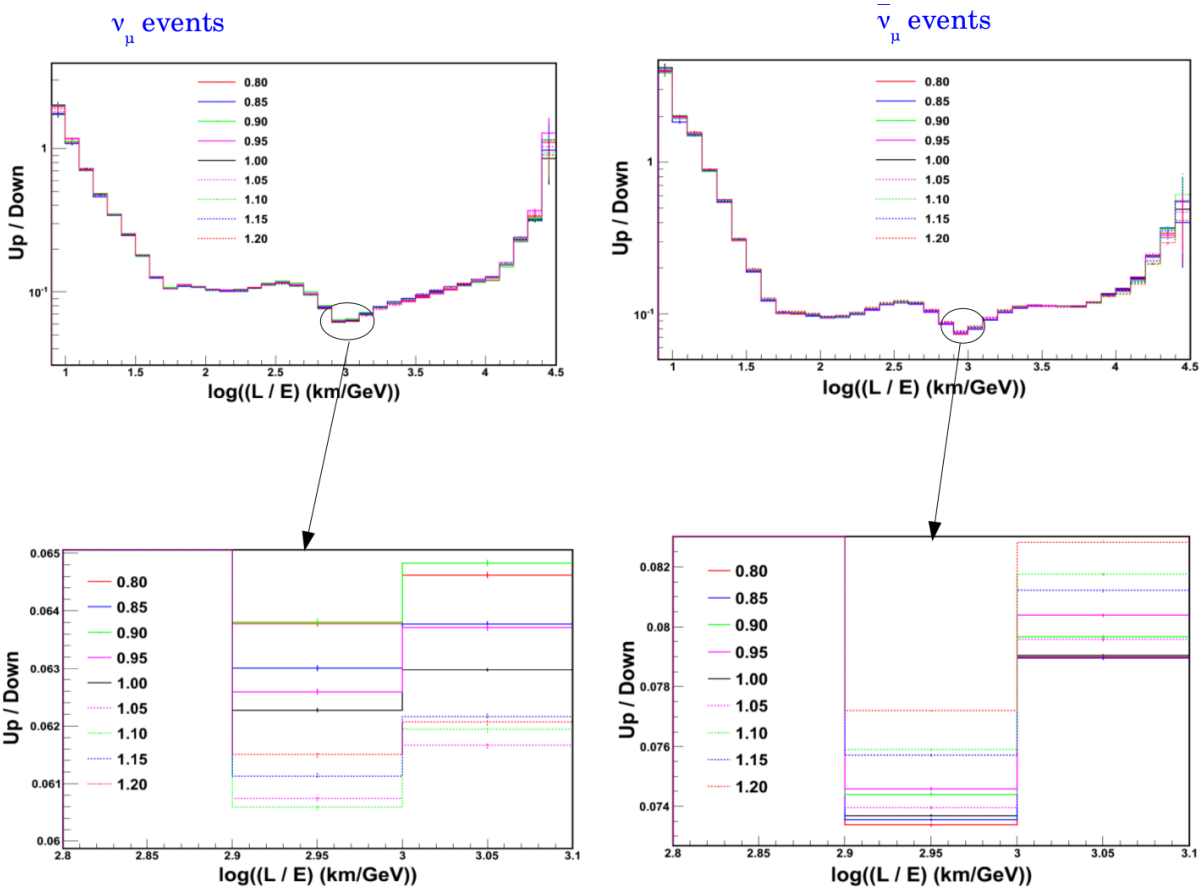

Figure 4.11: *[Colour online] Comparison of Up/Down ratios for neutrino and anti-neutrino events coming from all baselines in INO-ICAL for the default (PREM) density and the new (changed) densities of the core of the Earth. The values in the legend with colour coding show the ratios of* $\rho^{new}_{core}/\rho^{PREM}_{core}$*. The histograms on the left side are for* ν_μ *events whereas those on the right are for* $\overline{\nu}_\mu$ *events.*

profile of the core of the Earth compared to that from PREM. Similarly, Figure 4.15 shows the correlation between the measured dip values for $\overline{\nu}_\mu$ events in INO-ICAL due to atmospheric neutrinos traveling through all baselines and baselines only through the core whereas Figure 4.16 and 4.17 shows the same for neutrinos and anti-neutrinos passing only through mantle and core of the Earth respectively. We have also studied the correlation between the neutrinos and anti-neutrinos passing only through the core of the Earth, which is shown in Figure 4.18. Hence, from these correlation plots and by the measured values of the dip in the ratio of Up/Down

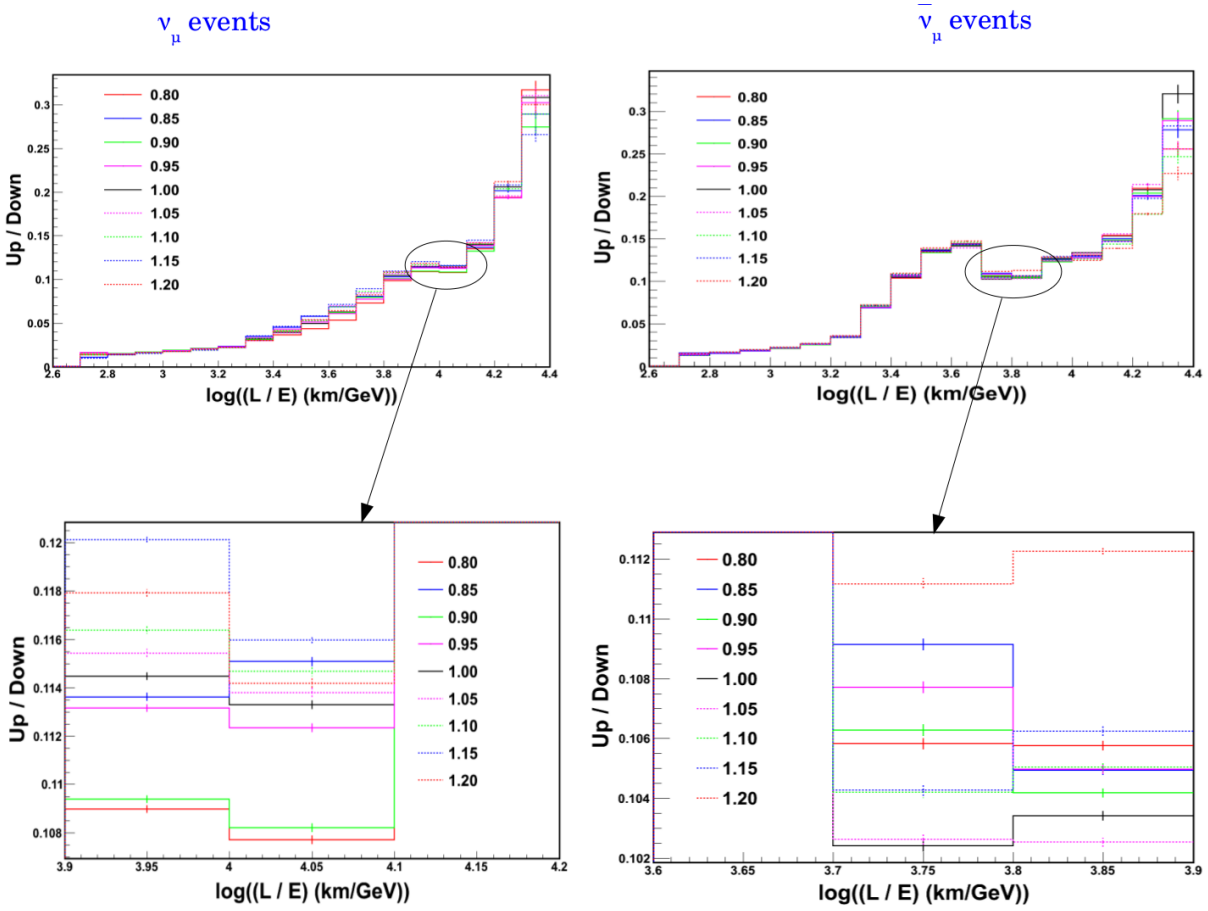

Figure 4.12: *[Colour online] Comparison of Up/Down ratio for neutrino and anti-neutrino events passing only through the core of the Earth and reaching INO-ICAL, for the default (PREM) density and the new (changed) densities of the core of the Earth. The values in the legend with colour coding show the ratios of* $\rho_{core}^{new}/\rho_{core}^{PREM}$*. The histograms on the left side are for* ν_μ *events whereas those on the right are for* $\overline{\nu}_\mu$ *events.*

neutrinos and anti-neutrinos reaching INO-ICAL through several baselines (directions) can help us to obtain the density of the core of the Earth and thus the matter density profile of the inner structure of the Earth.

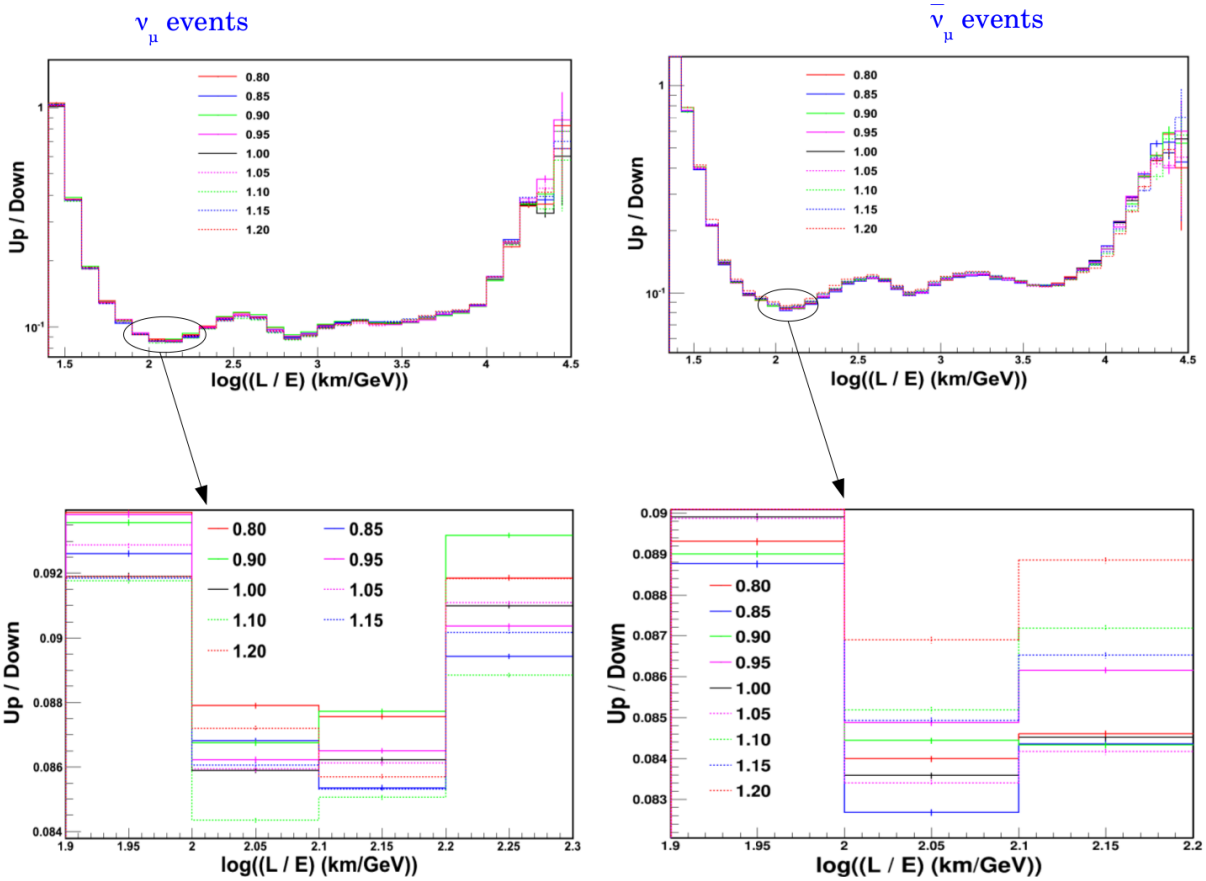

Figure 4.13: *[Colour online] Comparison of Up/Down ratio for neutrino and anti-neutrino events passing only through the mantle of the Earth and reaching INO-ICAL, for the default (PREM) density and the new (changed) densities of the core of the Earth. The values in the legend with colour coding show the ratios of* $\rho_{core}^{new}/\rho_{core}^{PREM}$*. The histograms on the left side are for* ν_μ *events whereas those on the right are for* $\overline{\nu}_\mu$ *events.*

4.5 Summary

Atmospheric neutrino flux mostly consists of ν_μ and $\overline{\nu}_\mu$ along with ν_e and $\overline{\nu}_e$ in a ratio of $(\nu_\mu + \overline{\nu}_\mu)/(\nu_e + \overline{\nu}_e) \approx 2$. Atmospheric neutrinos can be used as a suitable tool to probe the density profile of the inner structure of the Earth as they come with wide range of energies and provide a wide range of baselines. INO-ICAL, an upcoming atmospheric neutrino experiment with excellent direction resolution and charge identification efficiency, will be able to detect ν_μ

$\frac{\rho_{\text{core}}^{\text{new}}}{\rho_{\text{core}}^{\text{PREM}}}$	Baselines through					
	All		Core		Mantle	
	Position	Value	Position	Value	Position	Value
0.80	2.9 - 3.0	0.0637	4.0 - 4.1	0.1077	2.1 - 2.2	0.0876
0.85	2.9 - 3.0	0.0630	4.0 - 4.1	0.1151	2.1 - 2.2	0.0854
0.90	2.9 - 3.0	0.0638	4.0 - 4.1	0.1082	2.0 - 2.1	0.0868
0.95	2.9 - 3.0	0.0626	4.0 - 4.1	0.1123	2.0 - 2.1	0.0862
1.00	2.9 - 3.0	0.0623	4.0 - 4.1	0.1133	2.0 - 2.1	0.0859
1.05	2.9 - 3.0	0.0608	4.0 - 4.1	0.1138	2.0 - 2.1	0.0860
1.10	2.9 - 3.0	0.0606	4.0 - 4.1	0.1147	2.0 - 2.1	0.0844
1.15	2.9 - 3.0	0.0611	4.0 - 4.1	0.1160	2.1 - 2.2	0.0853
1.20	2.9 - 3.0	0.0615	4.0 - 4.1	0.1142	2.2 - 2.2	0.0857

Table 4.4: *Summary of positions and values of the dips obtained for events due to ν_μ reaching INO-ICAL.*

$\frac{\rho_{\text{core}}^{\text{new}}}{\rho_{\text{core}}^{\text{PREM}}}$	Baselines through					
	All		Core		Mantle	
	Position	Value	Position	Value	Position	Value
0.80	2.9 - 3.0	0.0734	3.7 - 3.8	0.1058	2.0 - 2.1	0.0840
0.85	2.9 - 3.0	0.0735	3.7 - 3.8	0.1092	2.0 - 2.1	0.0827
0.90	2.9 - 3.0	0.0744	3.7 - 3.8	0.1063	2.0 - 2.1	0.0845
0.95	2.9 - 3.0	0.0746	3.7 - 3.8	0.1077	2.0 - 2.1	0.0849
1.00	2.9 - 3.0	0.0737	3.7 - 3.8	0.1024	2.0 - 2.1	0.0836
1.05	2.9 - 3.0	0.0740	3.7 - 3.8	0.1026	2.0 - 2.1	0.0834
1.10	2.9 - 3.0	0.0759	3.7 - 3.8	0.1042	2.0 - 2.1	0.0852
1.15	2.9 - 3.0	0.0757	3.7 - 3.8	0.1043	2.0 - 2.1	0.0850
1.20	2.9 - 3.0	0.0772	3.7 - 3.8	0.1112	2.0 - 2.1	0.0869

Table 4.5: *Summary of positions and values of the dips obtained for events due to $\overline{\nu}_\mu$ reaching INO-ICAL.*

and $\overline{\nu}_\mu$ events in the oscillation channels $\nu_\mu \to \nu_\mu$, $\overline{\nu}_\mu \to \overline{\nu}_\mu$, $\nu_e \to \nu_\mu$ and $\overline{\nu}_e \to \overline{\nu}_\mu$. Neutrino (anti-neutrino) oscillation in vacuum is different from that in matter and also the matter effects in neutrino oscillation is different from the matter effects in anti-neutrino oscillation. The ratio of Up-coming neutrinos to Down-going neutrinos as a function of L/E, where L is the travel length and E is the energy of the neutrinos, can be a suitable tool to probe the density profile of the core of the Earth. A comparison in the measurement of the dip values in the Up/Down

$\frac{\rho_{core}^{new}}{\rho_{core}^{PREM}}$	Baselines through					
	All		Core		Mantle	
	ν_μ events	$\overline{\nu}_\mu$ events	ν_μ events	$\overline{\nu}_\mu$ events	ν_μ events	$\overline{\nu}_\mu$ events
0.80	+2.25	-0.41	-4.94	+3.30	+1.98	+0.48
0.85	+1.12	-0.20	+1.59	+6.60	-0.58	-1.08
0.90	+2.41	+0.95	-4.50	+3.80	+0.99	+1.08
0.95	+0.5	+1.22	-0.90	+5.18	+0.35	+1.56
1.05	-2.49	+0.41	+0.40	+0.20	+0.12	-0.24
1.10	-2.70	+2.99	+1.23	+1.76	-1.80	+1.91
1.15	-1.93	+2.71	+2.38	+1.86	-0.70	+1.67
1.20	-1.28	+4.75	+0.80	+8.60	-0.23	+3.95

Table 4.6: *% change in the values of the dips obtained for events due to $\overline{\nu}_\mu$ and $\overline{\nu}_\mu$ reaching INO-ICAL through all baselines, baselines passing only the core and mantle of the Earth. The change is w.r.t the PREM density profile of the Earth. The "+" sign indicates the increment and "-" sign indicates the decrement in the dip values w.r.t to PREM density profile.*

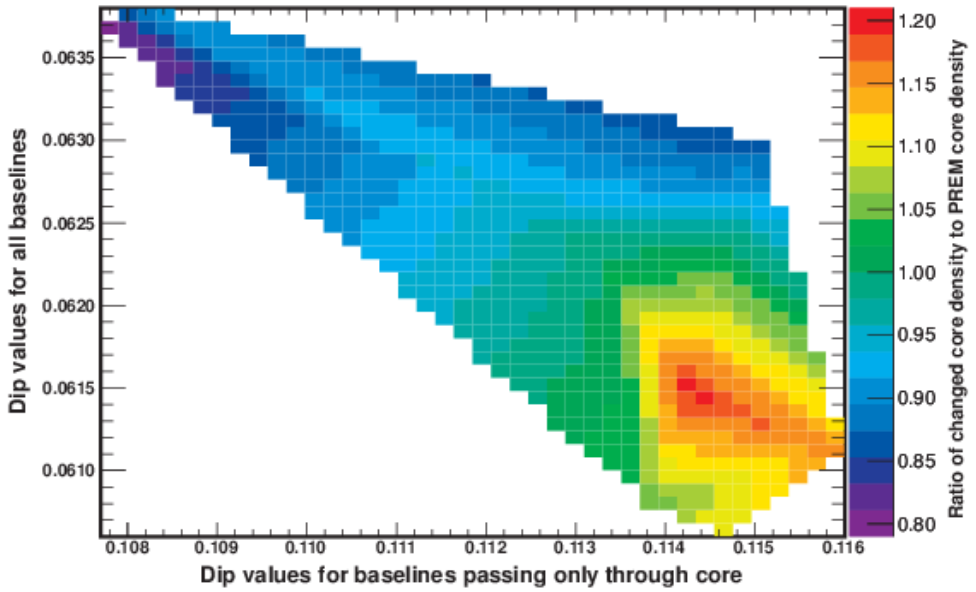

Figure 4.14: *[Colour online] Variation of the dip values for ν_μ events obtained from INO-ICAL for neutrinos passing through all baselines and only through core of the Earth*

ratio by the INO-ICAL for neutrinos (anti-neutrinos) passing only through the core and mantle and through all baselines will help in the determination in the deviation of the Earth matter

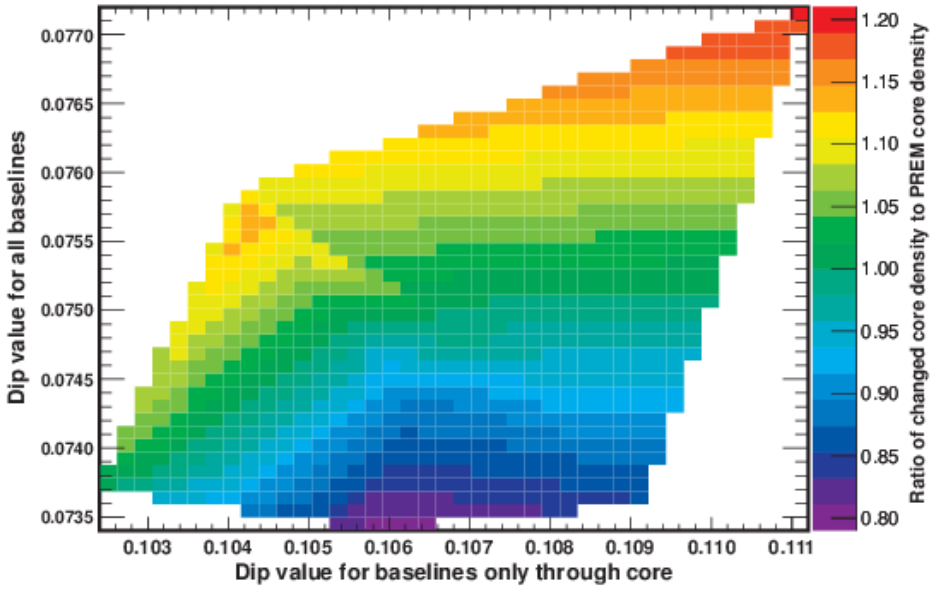

Figure 4.15: *[Colour online] Variation of the dip values for $\overline{\nu}_\mu$ events obtained from INO-ICAL for neutrinos passing thorugh all baselines and only through the core of the Earth.*

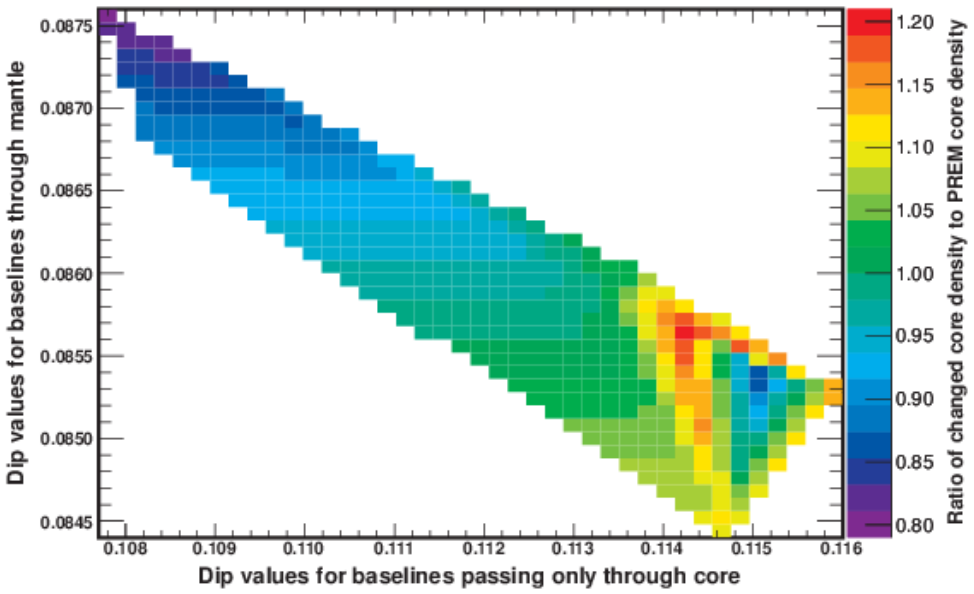

Figure 4.16: *[Colour online] Variation of the dip values for ν_μ events obtained from INO-ICAL for neutrinos passing only through the mantle and core of the Earth.*

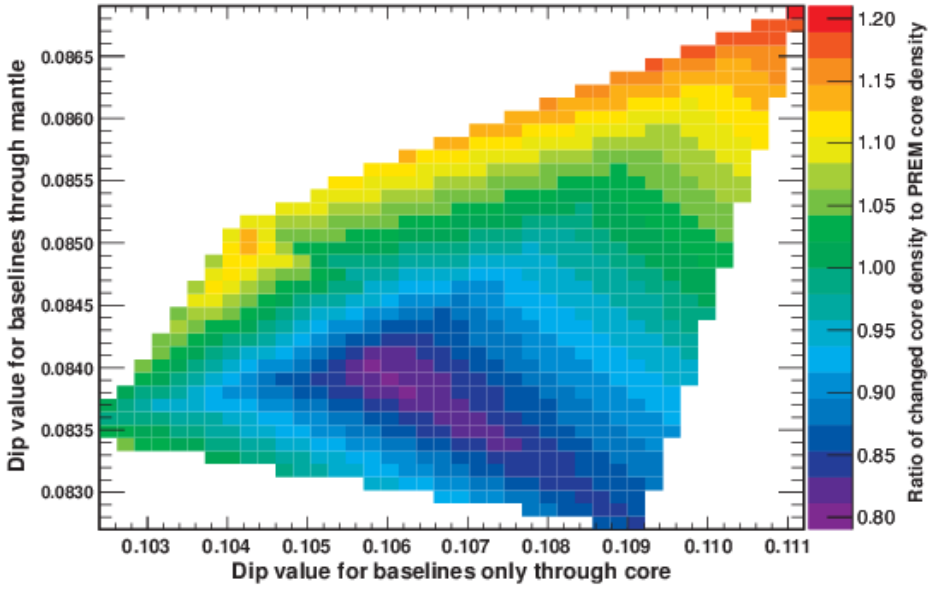

Figure 4.17: *[Colour online] Variation of the dip values for $\overline{\nu}_\mu$ events obtained from INO-ICAL for neutrinos passing only through the mantle and core of the Earth.*

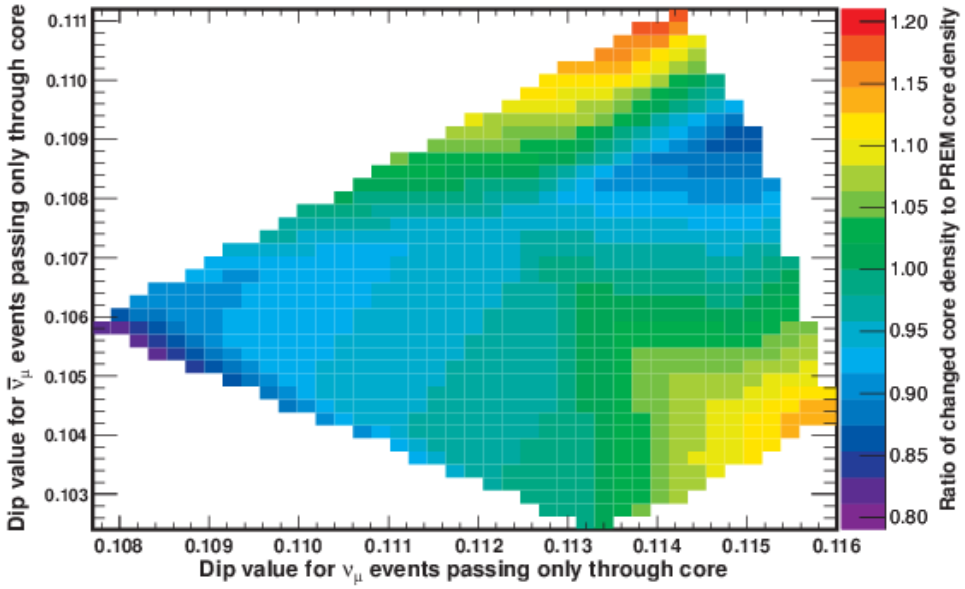

Figure 4.18: *[Colour online] Variation of the dip values for $\overline{\nu}_\mu$ and ν_μ events obtained from INO-ICAL for neutrinos passing only through the core of the Earth.*

density from the standard PREM.

Bibliography

[1] Adam M. Dziewonski, Don L. Anderson, *Preliminary reference Earth model,Physics of the Earth and Planetary Interiors*, **25**, (1981), 297.

[2] W. Winter, *Probing the absolute density of the Earth's core using a vertical neutrino beam,Phys.Rev. D*, **72**, (2005), 037302.

[3] H. Minakata and S. Uchinami, *On in situ Determination of Earth Matter Density in Neutrino Factory*, *Phys.Rev. D*, **75**, (2007) 073013.

[4] T. Ohlsson and W. Winter, *Reconstruction of the earth's matter density profile using a single neutrino baseline*, *Phys.Lett. B*, **512**, (2001), 357–364.

[5] T. Ohlsson and W. Winter, *Could one find petroleum using neutrino oscillations in matter?*, *Europhys.Lett.*, **60**, (2002), 34–39.

[6] E. K. Akhmedov, M. Tortola, and J. Valle, *Geotomography with solar and supernova neutrinos,JHEP*, **0506**, (2005), 053.

[7] M. Lindner et. al., *Tomography of the earth's core using supernova neutrinos*, *Astropart.Phys.*, **19**, (2003), 755–770.

[8] L. V. Volkova and G. T. Zatsepin Bull. *Acad. Sci. USSR, Phys. Ser.*, **38** (1974) 151–154.

[9] A. D. Fortes, I. G. Wood, and L. Oberauer, *Using neutrino diffraction to study the Earth's core*, *Astron. Geophys.*, **47**, (2006), 5.31–5.33.

[10] Irina Mocioiu and Robert Shrock, *Matter Effects on Neutrino Oscillations in Long Baseline Experiments*, *arXiv:***hep-ph/0002149**

[11] Sandhya Choubey and Prabir Roy, *Testing whether muon neutrino flavor mixing is maximal*, *arXiv:***hep-ph/0310316v2**

[12] Guinti C, Kim chung W, *Fundamentals of Neutrino Physics and Astrophysics*, **Oxford University Press**.

[13] http://www.icrr.u-tokyo.ac.jp/ mhonda/nflx2014/index.html

[14] M. Honda, M. Sajjad Athar, T. Kajita, K. Kasahara, and S. Midorikawa, *Atmospheric neutrino flux calculation using the NRLMSISE-00 atmospheric model*, *Phys.Rev. D*, **92**, (2015), 023004.

[15] INO Project Report, INO/2006/01, http://www.ino.tifr.res.in/ino//OpenReports/INOReport.pdf

[16] http://www.genie-mc.org/

[17] The ICAL collaboration, *Physics Potential of the ICAL detector at the India-based Neutrino Observatory (INO)*, **https://arxiv.org/pdf/1505.07380.pdf**.

[18] A. Chatterje et. al., *A Simulations Study of the Muon Response of the Iron Calorimeter Detector at the India-based Neutrino Observatory*, *JINST*, **9**, (2014), P07001.

[19] PhD thesis of Animesh Chatterjee, *Physics Sensitivity Studies at the ICAL detector*, **Homi Bhabha National Institute**, *September, 2014.*

Chapter 5

Resistive Plate Chamber

Detectors are our best friend to guide us through the vast sea of knowledge.

5.1 Introduction

Gas filled detectors are being extensively used in several high energy physics and neutrino physics experiments like ALICE, ATLAS, CMS, OPERA, BaBar, STAR, Belle, BES-III and so on. Several upcoming experiments like CBM, INO-ICAL, DUNE also aim to use gas filled detectors. These kind of detectors are of low cost, easy to develop, easy to operate, robust and can be developed over a large area. The detector parameters like efficiency, rate handling capability, particle identification capability, time resolution, position resolution, dead time etc. varies among these detectors. Depending on the experiment requirements, the specific choice of the gaseous detector in a particular experiment is being made. Over the past several decades, this field has seen appreciable improvement which has led to the development of significantly improved detectors. Different types of gaseous detectors presently used are Multi-Wire Proportional Chamber (MWPC), Time Projection Chamber (TPC), parallel plate avalanche chamber (PPAC), Gas Electron Multiplier (GEM), micromegas and so on. Resistive Plate Chamber (RPC)[1] is also a type of gas filled detector. It was first introduced in the year 1981 by R.Santonico and R. Cardarelli. RPC has subsequently found wide range of applications in several past, present and

future high energy physics and neutrino experiments.

This chapter focuses on the Resistive Plate Chamber, its historical evolution, working principle, modes of operation, classification and applications of RPC followed by a brief introduction on the development of oil-free bakelite RPC.

5.2 Historical development of RPC

5.2.1 Evolution of geseous detectors

Detectors play an important role in our daily life. Human eye is an example of a natural particle detector. Out of curiosity, particle detectors for specific detection purposes are being developed. The particle detectors of the present era thus evolved slowly. The development of particle detectors by mankind dates back to 1890s when X-ray and radioactivity were discovered. The discovery of X-rays opened the door for discovery of radioactivity and hence the birth of particle detector. The photosensitive paper, blackened by radiation from uranium salt, used by A. H. Becquerel when he discovered radioactivity, is perhaps the first documented particle detector. Later, in the beginning of the 20th century, E. Rutherford and E. Marsden used a scintillating screen to detect the scattering of alpha particles which gave birth to the first atomic model. Sooner people developed detectors like spark chamber, cloud chamber, bubble chamber, emulsions, to look for the tracks of charged particles using optical methods. As the technology developed, electrical methods were chosen over the optical ones. Among the electrical methods, scintillators with coupled photo multiplier tubes gained importance. Slowly, R&D had started on ionization detectors. These were the first electrical devices developed for radiation detection. They work on the principle of gas ionization when a charged particles passes through it. These kind of detectors gained more importance as they had shown better spatial resolution than that of the scintillators.

After detailed R&D, in 1928 Geiger and Müller invented a detector which was capable of detecting the electron-ion avalanche produced by the amplified ionization of the gas present

between an anode wire and cylindrical cathode in a coaxial cylinder. The amplification of the ionization was done by applying high electric field between the central wire (anode) and the outer cylinder (cathode). The advanced form of these kinds of wire-based detectors like multi-wire proportional chambers (MWPC)[3], invented in 1967 by G. Charpak, found applications in several experiments as they provide a good spatial resolution. Due to the geometry of the wire based detectors, the electric field between the anode and the cathode has a strong dependence on $\frac{1}{r}$, where r is the distance from the wire. As the radius of the anode wire is much smaller than that of the cathode, the electric field is very high in the vicinity of the anode, hence the amplification of the ionization happens in this region. This leads to a good spatial resolution ($\sim 100\mu m$). On the other hand, these kinds of detectors are known to have poor time resolution because of the fact that the electrons generated in primary ionizations need to drift to the vicinity of the anode in order to give a detectable signal as the elctric field has $\frac{1}{r}$ dependency. The drift of the electrons introduces a time jitter giving a poor time resolution. Removing the "distance" dependency on the electric field can minimize the time jitter, hence improving the time resolution. This idea led to the development of parallel plate counters as they have uniform electric field between the anode and the cathode. The Keuffel Spark counter[4][5] is the first gas detector developed based on this principle.

5.2.2 Spark Counter

In general, spark counters are made up of two planar metal electrodes with a certain uniform gap between them. High voltage is applied across these metal electrodes. the gap is filled with certain mixture of gases. When a charged particle passes through the gas, it causes primary ionization in the gas that triggers multiple ionization in presence of high electric field resulting into avalanche formation. As the avalanche grows, it results into a streamer which ultimately connects the two electrodes in the form of a conducting plasma filament which creates a spark. The spark mode of operation (streamer mode) results into large signals avoiding the electronic time jitter, hence increasing the time resolution as compared to wired based gas detectors[2].

Keuffel Spark Counter

The Keuffel Spark counter[4][5], developed in 1948 by J. Warren Keuffel , is the first gaseous detector that works on this principle. The electrodes used in Keuffel spark counter were of copper with a separation of ∼2.5 mm between them. The gap between these electrodes was filled with a mixture of Argon and Xylene at ∼ 500 mbar pressure. A uniform electric field of ∼4-12 kV/cm was applied between the electrodes. The time resolution of the Keuffel Spark counter was ∼1 nano-second which is far better than Geiger-M*ü*ller counter which was in extensive use during that time.

However, the spark or discharge created in a spark chamber had several shortcomings. First of all, it damages the inner surface of the electrodes. The dead area of these kinds of detectors increases due to the non restriction of the charge as the electrodes are metallic. Also, the dead time of these detectors were measured to be a few milliseconds which ultimately limits the rate handling capability of the detectors. In order to overcome these problems, a new kind of parallel plate gas detectors were introduced with resistive plate electrodes, known as Pestov spark counters[6][7].

Pestov Spark Counter

The Pestov spark counter[6] was introduced in 1971 by Yu. Pestov and V. Parchomchuk. It uses resistive plate electrodes unlike that of Keuffel spark counter. The resistivity of the electrodes used is $\sim 10^9\ \Omega cm$. A special gas mixture was used which absorbed the photons, specially the UV photons, as they were responsible for the streamers in Keuffel spark counter which resulted into the damage of the electrodes. The high resistivity of the electrodes led to the localization of the discharges and the remaining area of the counter was still be available for the incoming particles, hence reducing the dead area of the detector. The Pestov counter having a gas gap of ∼0.1 mm resulted a time resolution of ∼25 ps [2] and a noise rate of ∼0.2 Hz/cm^2[8]. A very good surface smoothness of the electrodes were needed in Pestov counter as the electric field was ∼500 kV/cm in 0.1 mm gas gap. Operation of the detector at a high over-pressure of the gas

(∼12 bar) ensured a very good detection efficiency (close to 100%)[2][8]. The major limitations of the Pestov counter were the gas pressure, component of the gas mixture (butadiene) and the lack of availability of suitable electrodes[8].

5.2.3 Parallel Plate Avalanche Chambers

Generally gaseous detectors exploit the avalanche multiplication phenomenon. These detectors are easy to build and operate. Parallel Plate Avalanche Chamber (PPAC) is also a kind of gaseous detector which uses this phenomenon and is very similar to spark counter. The electrodes in a PPAC are made up of materials like metalized ceramic or metals or plastics. The gas gap varies from 500 μm to 2 mm and is maintained by precise spacers. These detectors are operated in avalanche mode and hence streamers or discharges are the unwanted side effects. These detectors were in use during 1990's. The advantages of PPAC were

1. A proper choice of gas mixture helps in minimizing the streamer formation which results into improved rate handling capability up to 10 MHz/cm^2 [12].

2. With proper gas mixture, one can increase the gas gain to $10^3 - 10^4$ with a very low discharge probability (down to 10^{-5}) for Minimum Ionizing Particles (MIP)[2].

3. A time resolution of ∼100 - 250 ps can be achieved[13][14].

The major disadvantages were

1. The PPAC signals were small. The average charge content being ∼(1 - 10) fC [14], resulting into a low signal to noise ratio which affected the detector efficiency.

2. The electronics had to be of very low noise, fast and sensitive for timing purposes[2]

3. The major limitation being their tendency to discharge when attempting to reach high gas gain resulting to a spark and causing damage to both the detector and the read out electronics[9].

4. The fabrication of PPAC was non trivial.

Because of these disadvantages, the use of PPACs for large experiments and applications was questionable[15]. Acknowledging the limitations of the previous parallel plate gaseous counters, R.Santonico and R. Cardarelli came up with the idea of using high resistive materials for both the electrodes and hence the birth of **Resistive Plate Chamber** or **RPC**.

5.3 Resistive Plate Chamber

Resistive plate chamber is a parallel plate gas filled detector which utilizes a constant and uniform electric filed maintained between two high resistive electrodes. It is an evolved form of parallel plate chamber. It works on the principle of gas ionization due to the interaction of the incoming particles (charged particles) with the gas molecules present in between the electrodes. RPC was first introduced in the year 1981 by R.Santonico and R. Cardarelli [1]. Figure 5.1 shows the schematic of a single gap RPC. Basically a RPC is made up of two parallel plates of

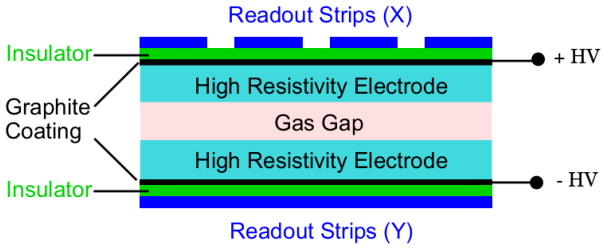

Figure 5.1: *[Colour online] Schematic diagram of a RPC [2].*

high resistive ($\sim 10^9 - 10^{14}\ \Omega cm$) material, like glass or bakelite, separated by a uniform gap which is maintained by spacers. Hence, they are called high resistive electrodes. The spacers are made up of even higher resistive materials. The outer side of the resistive plates are coated with graphite or conducting paint in order to apply high voltages. The uniformity of the conductive coating defines the uniformity of the potential distribution and hence the electric field in the gap between the electrodes. For a single gap RPC, the typical electric field produced in the

gap is $50kV/cm$. A certain mixture of gases having specific properties, is flown through the gap between the electrodes. The mixture of the gas depends on the operation of the RPC. The most important property of the gas mixture is ionization i.e when a charged particle like muon, passes through the gas gap, it ionizes the gas molecules. The ionization produces electron-ion pairs whose number gets enhanced further in the presence of high electric field by secondary and tertiary ionizations and creates an "avalanche"or a large collection(s) of electron-ion pairs. This avalanche is then detected in the form of induced signal(s) on read out strips kept on both the sides (top and bottom) of the RPC. The read out strips are kept orthogonal to each other so as to get the X-Y positions of the particle that passed through.

5.3.1 Working Principle of Resistive Plate Chamber

When a charged particle like μ^+, μ^- having sufficient energy, traverses through the gap, it creates several primary electron-ion pairs during its course of travel. Under intense electric field, the primary electrons cause further secondary, tertiary, quaternary and further multiple ionizations. This multiplication mechanism results in a distribution of free charge in the gas which has the characteristic shape of an avalanche as shown in Figure 5.2. These charges then travel towards

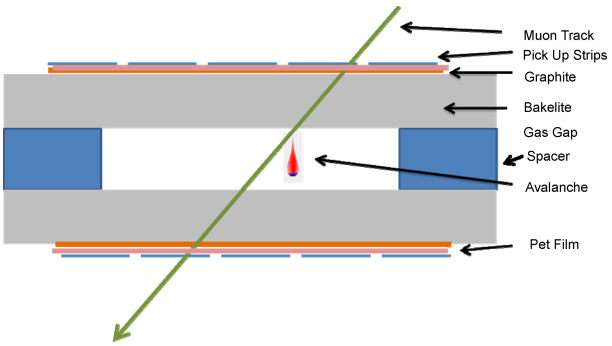

Figure 5.2: *[Colour online] Schematic diagram of a RPC with with a muon passing through the gas gap which creates an avalanche[16].*

the respective electrodes. As the drift velocity of electrons is much more than those of the ions, the avalanche takes the shape of a "liquid drop"with the electrons at the head and the ions

at the tail of the drop. During the process of avalanche formation, several photons are also generated due to the recombination process, excitation and de-excitation of the electrons during ionization. Along with the electrons, these photons also contribute significantly to the formation and size of multiple avalanches which forms the streamers. Based on the size and number of these space charge clusters created, the operation of RPC is divided into two - Avalanche and Streamer mode of operation. The next section discusses the details about these two modes. Moreover, if the ion-electron plasma is so large as to connect the two electrodes, then the so called "spark" is created between the two electrodes. An avalanche distorts the applied electric field inside the gas gap. Figure 5.3 demonstrates in a very simple way, how an avalanche affects the electric field in the gas gap. The avalanche charge carriers influence the electric field in the gas gap which affects their own propagation and multiplication. This phenomenon is known as **space-charge effect**. However, phenomenon of the actual physical processes inside a RPC is very complex and one can look into ref. [17] for the details.

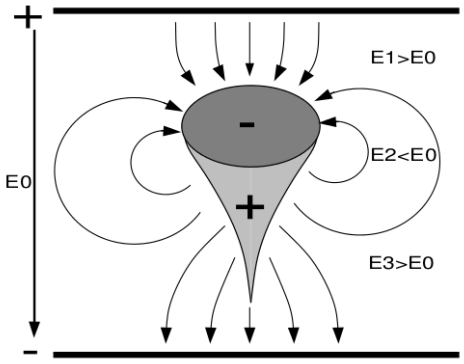

Figure 5.3: *[Colour online] Illustration of the effect on the electric field inside a RPC gas gap in presence of an avalanche. E_0 is the applied electric field. E_2 is the electric field of a created avalanche. E_1 and E_3 are the resultant electric field in the gas gap near the head and tail of the avalanche.[17].*

The dynamic behaviour of the growing number of space charges induces a signal on the external read out panels. As the resistivity of the electrodes are very high, they are completely transparent to these charges. The details of the generation of the signals can be explained by the Shockley-Ramo theorem[11][34] for induced charges and has been well explained in ref. [10].

High resistivity of the electrodes prevents high voltage supply from providing the electric charge that would be necessary to maintain the discharge between the electrodes. Therefore the electric field drops drastically in the region of the discharge causing it to extinguish with the typical duration of the discharge of ∼10 nano-seconds. The charge-up time after each discharge is independent of the detector surface dimensions but depends on the time constant of the RPC which comes out to be ∼2 s for a RPC wih electrode resistivity $\sim 5 \times 10^{12}$ Ωcm[24][35]. Hence, the charge-up time is much higher compared to the discharge time. During the charge-up time the detector behaves as an insulator and remains inactive. But as the area of the detector affected by the discharge is limited to ∼0.1 cm^2 (called dead area), the remaining area of the detector, is unaffected and retains its sensitivity to the incoming charged particles. This property of resistive electrodes vastly improves their rate capability. The resistivity and thickness of the electrodes and modes of operation of the RPC determines the rate handling capability of the RPC[36].

5.3.2 Modes of Operation of Resistive Plate chamber

There are two modes of operation of a RPC viz. "avalanche mode"and "streamer mode". The mode of operation is decided by the gas gain of the detector which is further decided by the mixture of the gas and the applied high voltage or electric field. Because of the high gas gain, a change occurs in the avalanche dynamics. The total number of charge carriers in an avalanche determines the detectability of the signal and hence that of the penetrating charged particle. As the gas gain of the RPC is increased further, the photons start to contribute to the avalanche dynamics and streamers or weak sparks are created. The details about the modes of operations has been discussed below.

Let n_0 be the number of electrons in a cluster at any particular point inside the gas gap. The number of electrons reaching the anode is given by [10], [11]

$$n = n_0 e^{(\alpha - \beta)x} \tag{5.1}$$

where,

α is the number of ionizations per unit length, also known as the first Townsend coefficient.

β is the number of electrons captured by the gas per unit length, also known as the attachment coefficient, and

x is the distance between the anode plate and the point where the cluster is produced.

The gas gain of the detector is defined as

$$M = \frac{n}{n_0} \tag{5.2}$$

The mode of operation of a RPC is decided by Raether limit which is the physical limiting value of the gas gain (M) or multiplication factor. If M is much lower than 10^8, then formation of additional secondary avalanches is prevented and simple charge multiplication phenomenon occurs, whereas if M is greater than 10^8 , then primary ionizations will give rise to streamers with high probability. Hence, if M $> 10^8$, the mode is called the streamer mode and if $M << 10^8$ the mode is avalanche mode. Figure 5.4 and Figure 5.5 show a schematic description of the phenomenon in avalanche and streamer mode of operation of a RPC respectively.

The modes of operation of a RPC can also be explained by another notion. As propounded by Yu. N. Pestov, a planar detector with resistive electrodes can be modeled as a set of discharge cells which to the first order can be considered independent of each other. The expression for capacitance of a planar condenser leads to the fact that the area of such cells is proportional to the total average charge Q, that is produced in the gas gap, as governed by the equation below

$$S = \frac{Qd}{\epsilon V} \tag{5.3}$$

where,

d is the gap thickness,

V is the voltage applied to the electrodes and

ϵ is the permitivity of the gas.

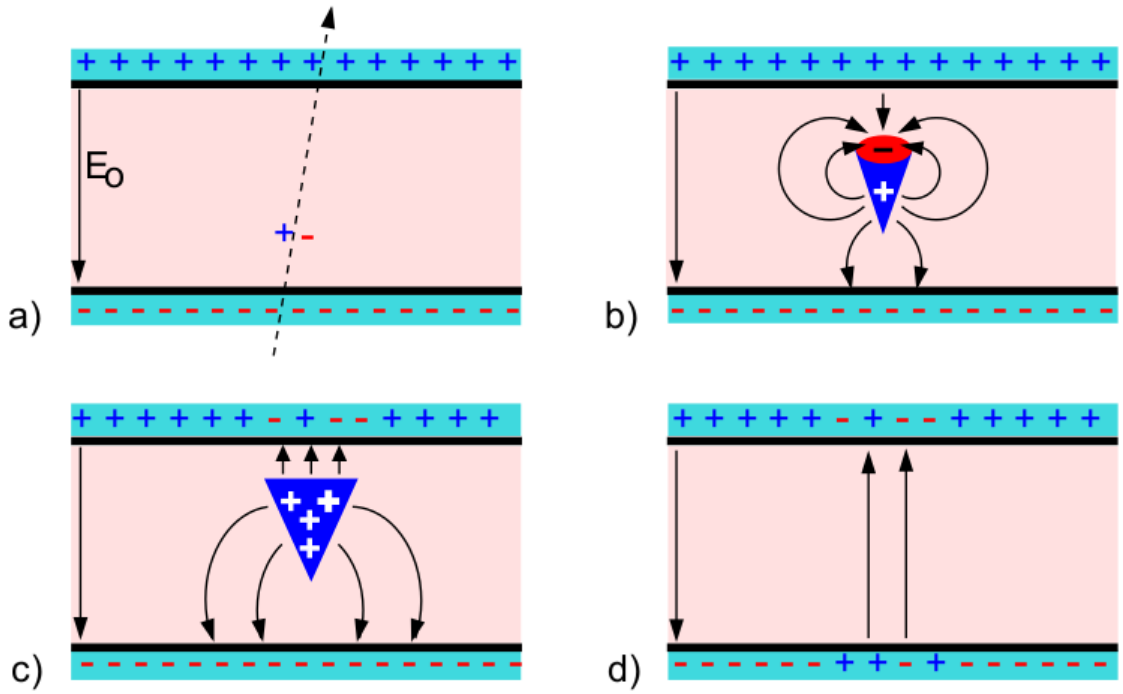

Figure 5.4: *[Colour online] Schematic description of the phenomenon in avalanche mode of operation of a RPC. a) Primary ionization of gas atoms by through-going radiation culminating in a Townsend Avalanche in an electric field E_0 b) Avalanche dynamics starting to influence the electric field c) Owing to the large differences in mass, electron drift velocity is considerably higher than ions and the electrons and ions reach respective electrodes at different times. d) When ions finally reach the cathode, the discharge affects a small area of the electrodes due to its high resistivity, around the region of avalanche development [2].*

From the above equation, it can be concluded that the smaller the Q, the smaller the surface of the discharge cells and therefore the higher the rate capability. In the streamer mode of operation, the average charge produced in the gas gap is between 50 pC[37] and a few nC[38], hence, no pre-amplification is required as the signals are quite large. This makes the read-out technique simple. Whereas, in the avalanche mode of operation the average charge produced is $\sim$1 pC, resulting a need for the amplification of the signal. Depending on the experiment requirements, RPC can be operated in either of the modes. The mode of operation can be controlled by the two most important factors - the electric field and the mixture of gases inside the gas gap. A sufficiently high electric field increases the kinetic energy of the electrons sufficient

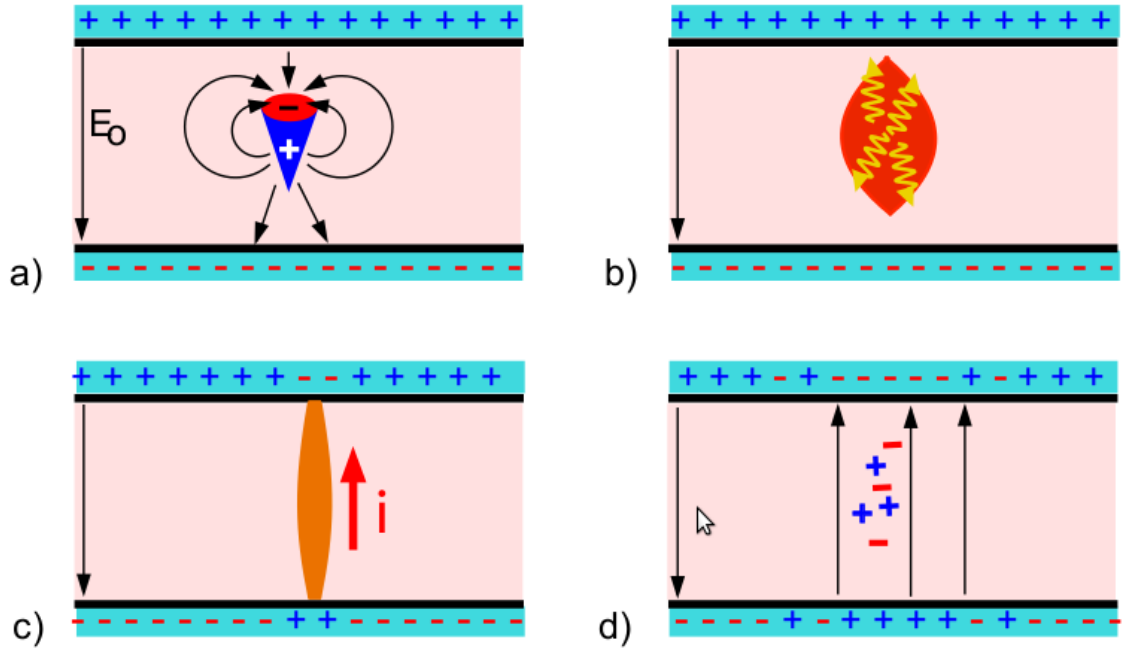

Figure 5.5: *[Colour online]]Schematic description of the development of a streamer in a RPC a) A Townsend avalanche developing after the passage of radiation b) At very high values of gas gain, enormous charge in the sensitive volume of the detector modifies the external electric field strongly. Photons also play a major role in spreading the avalanche and streamer evolution c) Formation of a conductive channel between the electrodes leads to sparks and discharge of wider regions of the electrodes d) The discharge causes a reduction of the electric field at the avalanche spot creating a dead area [2].*

enough to create more and more multiple ionizations and avalanches resulting into streamer formations. The electric field can be further controlled by either optimizing the thickness of the gas gap or by the applied high voltage. The role of the gas mixture has been discussed below.

5.3.3 Role of RPC Gases

In any gaseous detector, the gas mixture flown, is the heart of it as the mixture undergoes ionization and the gas gap acts as the sensitive medium. Hence the choice of a gas or mixture is very critical for any gaseous detector. Ideally, the process of ionization, avalanche formation and multiplication can happen in any gas or gas-mixture provided sufficient energy is deposited in the gas volume in presence of suitable electric field. However large size experiments with a

stable performance of the gaseous detectors, require to satisfy certain criteria. Those being

- High gas gain or easily ionizable gas
- Chemically inactive or inert
- Swift recovery
- Extended life time or stable over a longer period
- Easy availability
- Low cost
- Operation at low electric field

Among all the gases, Argon fits properly with all the above conditions and serves as a perfect choice as an ionizing agent. Ionization and excitation of Argon atoms occurs simultaneously due to the interaction of the argon atoms with an incoming particle. The excitation of argon atoms leads to the generation of photons which result into undesirable secondary ionizations within the gas gap, enhancing the avalanche to streamer transition probability. So, detectors operating with only Argon has the disadvantage of transition to the discharge mode at gas gains $\sim 10^3$ - 10^4. It is necessary to dissipate the photon energy via non-radiative processes. The polyatomic gas molecules having rotational or vibrational degrees of freedom may serve the purpose. These gases are known as *photon quenchers*, the examples being methane (CH_4), Iso-butane (i-C_4H_{10}), carbon dioxide (CO_2). In order to restrict the probability of avalanche to streamer transition and formation of multiple avalanches in the sensitive gas gap, it is also necessary to quench the energetic electrons. This purpose is served by introducing an electronegative additive in the gas mixture. Freon and SF_6 are such examples. They act as *electron quenchers* in gas detector's gas mixtures, especially in RPC's. One more advantage of using Freon is that due to its high atomic mass and cluster density, it is a suitable ionizing gas for small sized gaps in avalanche mode of operation. In my thesis work, a gas mixture containing Argon, eco-friendly freon (R134A) and iso-butane in the ratio of 34:57:9 has been used for the streamer mode of operation of the RPCs.

5.3.4 Classifications of Resistive Plate Chamber

I. Based on application

Based on the application of RPCs in several experiments, they can be divided into following types:-

A. Timing RPC

RPCs are known to have very good time resolution. The time resolution of a typical single gap RPC with a gas gap of 2 mm is of the order of 1 nano-second, whereas in multi-gap configuration, the same can go down to $\leq$50 pico-seconds. The gas-gap maintained in multi-gap configuration is 0.2 mm to 0.3 mm with an electric field of $\sim$100 kV/cm in the gas gap. Large area ($\sim$ m^2) multi-gap RPCs (MRPCs) are widely used in several experiments for Time-Of-Flight (TOF) measurements. These RPCs are operated in avalanche mode.

The basic principle of operation of timing RPCs may be described as follows. The initial current, due to the avalanche or space charge created, grows exponentially in time until the discriminating level is reached. The time delay between the primary ionization and the signal detection is independent from the position occupied by the initial charges in the gas gap, resulting excellent timing. The observed timing jitter depends only on the variation of the initial current (which is due to avalanche and cluster statistics) and inversely on the current growth rate αv, where α is the first Townsend coefficient and v is the electron drift velocity[18],[35]. It can also be concluded that in the first approximation, the timing resolution should be independent of the discriminator level. Both this effect and the inverse dependence on αv have been experimentally confirmed [18].

B. Triggering RPC

The RPCs which are used for triggering the Minimum Ionizing Particles (MIPs) such as muons in the muon detector systems are referred as the Trigger RPC. RPCs are used for triggering

purposes over large areas because of its fast response time and its robustness. These RPCs are of large area with 2 mm single or double gas gap configuration. These are operated either in avalanche or streamer mode depending on the particle flux rate. In avalanche mode of operation, they can handle a particle flux of several kHz/cm^2 with detection efficiency of ∼98% and time resolution (σ) of ∼1 nano-second.

II. Based on design

A. Single gap RPC

The original RPC design, developed by R. Santonico and R. Cardarelli, was a single gap detector. Since then a number of improvements have taken place. The first RPC used bakelite sheets having a bulk resistivity of the order of $10^{10} - 10^{11}$ Ωcm, as electrodes. The two electrodes were separated by 1.5 mm thick rectangular frame of PVC. Hence the gas gap was 1.5 mm. Nowadays, most of the single gap RPC has a gas gap of 2 mm. The electric potential to the electrodes is applied through a semi-conductive layer smeared on the outer surface of these electrodes which remains transparent to the induced signals. This allows one to operate the pick-up panels at ground potential, saving the utilization of high-voltage capacitors and avoiding the need for high-voltage insulation of the strips. These RPCs have a detection efficiency of ≥95% with a time resolution (σ) of 1 - 1.5 ns. A schematic of single gap RPC is shown in Figure 5.1.

B. Double gap RPC

The design of the first double gap RPC[19] was introduced by R. Cardarelli, R. Santonico, A. Di Biagio and A. Lucci in 1988 to improve the detection efficiency along with the avalanche mode of operation increasing its counting rate capability. Double gap RPCs allow for more varied structures compared to the single gap RPCs as they have a larger number of elements (gap gaps, electrodes, pickup panels). Figure 5.6 shows the schematic of a double gap RPC. Several experiments like CMS, BELLE, L3 uses double gap RPCs. Double gap RPCs are also made by sandwiching two independent gas gaps with a common pick-up panel in the middle.

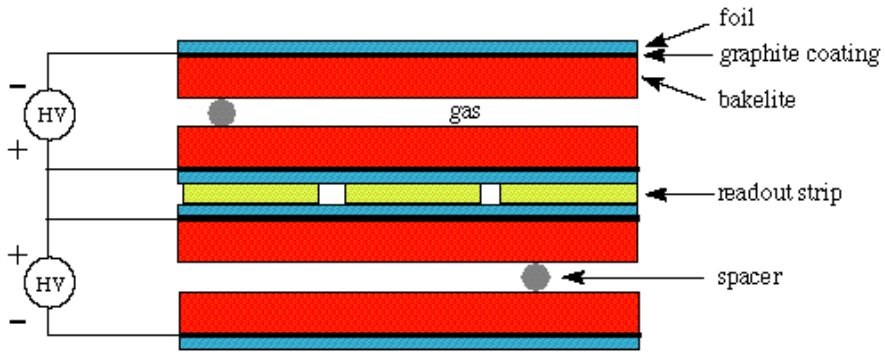

Figure 5.6: *[Colour online] Schematic diagram of a double gap RPC.*

The avalanches produced in either or both of the gas gaps induce signals in the common pick-up strips. CMS uses independent gas gaps with a common pickup panel while BELLE uses two single gap RPCs stacked one over the other.

C. Multi-gap RPC

The Multi-gap Resistive Plate Chambers (MRPCs) are advanced form of RPC detectors where the gas gap of a single gap RPC is divided into multiple gas sub–gaps with highly resistive electrodes to improve the time resolution of the later without sacrificing its other good qualities like efficiency. The first MRPC was introduced in the year 1996[20]. The high voltages (HV) are applied only to the external surfaces of top and bottom electrodes and the intermediate electrodes are electrically floating. Each of these electrodes are well separated from each other by very thin ($\sim$0.250 mm) spacers. The readout panels or electrodes are located outside the stack and are well insulated from the high voltage electrodes. A passing charged particle may create an avalanche in any one or more than one or all gas gaps. The avalanches in different gaps have the same time development. As the intermediate plates are transparent to the avalanche signals, thus induced signals on external anode and cathode are analogue sum of avalanches in all gaps. The time jitter in the rise time of the signal is expected to reduce due to smaller sub gaps, resulting into a much better time resolution than single gap RPC. From the simulation

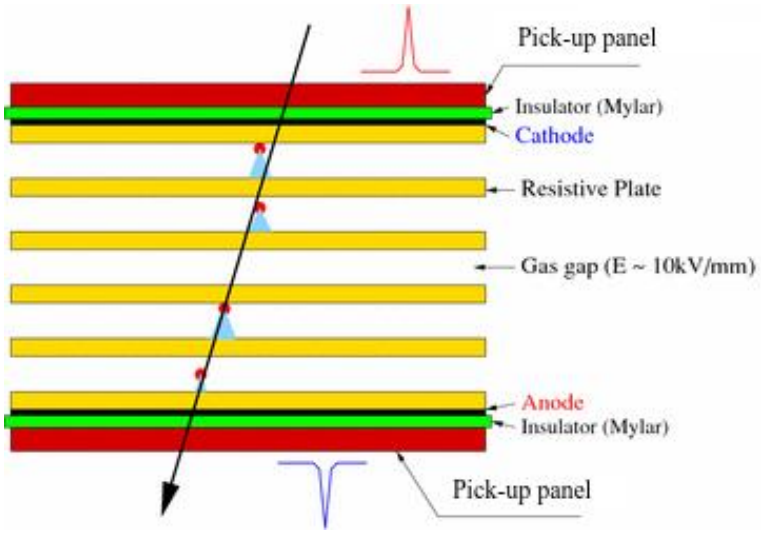

Figure 5.7: *[Colour online] Schematic diagram of a multi gap RPC[21].*

studies, it has been shown that the efficiency increases and time resolution improves with the increase of number of gaps[22]. If the gas gap of a single gap RPC is divided into n number of gaps to form a MRPC, then, it can been shown that the time resolution scales with $\sigma_t/\sqrt{n}$, however, the efficiency does scale with expected scaling law of 1-(1-ε)^n , where σ_t and ε are the time resolution and efficiency respectively of the single gap RPC [22]. The best time resolution from MRPC is ∼15.8 ps[23].

D. Wide gap RPC

The gas gap in a RPC is the heart of the detector. It has two purposes viz. to produce the primary ionization cluster which later on gives an avalanche or streamer and to provide suitable gas gain to provide detectable signals. Hence the accumulated charge in a signal depends on the gas gap, the gas mixture and the electric field inside the gas gap. Depending on the application, two types of RPC detector can be chosen, the first one is single (gas gap: ∼ 2 mm) gap RPC (also referred as narrow gap RPC) as discussed earlier and the second one is **wide gap RPC**[20] (gas gap: 8 mm or 9 mm). The main advantage of the wide gap RPC is the lower dynamic

range of gain which leads to the smaller current flowing through the gas gap and resistive plates. The time resolution for wide gap RPC is poor as the larger path produces larger fluctuation in signal arrival time[24].

E. Hybrid RPC

In hybrid RPCs[25], the electrodes are a combination of resistive and metallic plates and still retain the main property of a RPC : the absence of heavy discharges. Figure 5.8 shows a schematic of an hybrid RPC. It is a pair of identical double gap RPCs with a 3 mm thick high

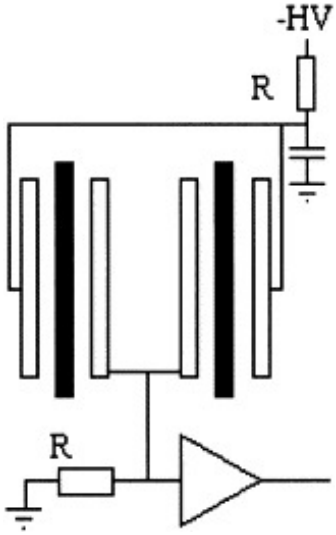

Figure 5.8: *[Colour online] Schematic diagram of a hybrid RPC. The long white rectangles represent the aluminum electrodes and the black ones the resistive glass electrodes[25].*

resistive glass electrode sandwiched between two 2 mm thick aluminum electrodes in each pair. These RPCs can provide a time resolution (σ) $\leq$80 ps with a detection efficiency >95%. These RPCs are easy to construct and mechanically stable. They can be used in TOF and Positron Emission Tomography (PET) imaging as they have good time resolution.

F. Micro RPC

A standard RPC is known to have a good time resolution whereas the position resolution is ∼1 cm as the majority of RPC applications do not require a very good position resolution. However, several attempts have been made to optimize their position resolution. Micro RPC[26] is a special type of RPC which has shown a position resolution of few tens of μm. Figure 5.9 shows a 0.1

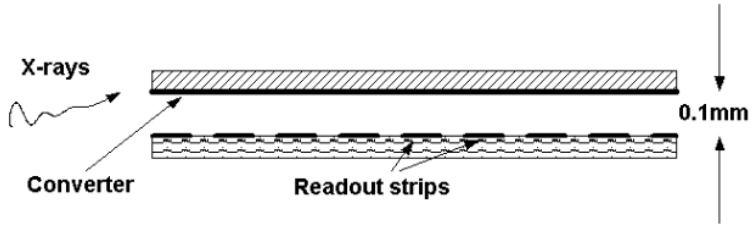

Figure 5.9: *[Colour online] Schematic diagram of a micro RPC[27].*

mm gap RPC equipped with a solid X-ray converter and anodic strips placed at a pitch of 30 μm which has shown a position resolution (FWHM) of at least 30 μm. The reasons being the good localization of the primary charge given by the solid converter and the fact that most of the charge in the avalanche is developed very close to the anode. Due to its exponential growth in space, the avalanche yields a very narrow induced charge profile[27].

5.4 Application of Resistive Plate Chambers

Resistive Plate Chambers are one of the most successful and extensively used gas detectors in high energy physics experiments. The major advantages of using RPCs are as follows

1. They are low cost detectors and easy to fabricate.
2. They can be developed over a large area (∼m^2).
3. They provide good time resolution (∼1 ns in the case of single gap RPC and ∼20 ps in the case of multi-gap RPC).

Experiment	Application	Area covered (m^2)	Electrode material	Electrode bulk resistivity (Ωcm)	No. of gas gaps	Gas gap thickness (mm)	Operation mode
ALICE-Muon	Trigger	140	Bakelite	3×10^9	1	2	Streamer
ALICE-TOF	Timing	150	Glass	10^{13}	10	0.25	Avalanche
ATLAS	Trigger	6550	Bakelite	$(1 - 4)\times10^{10}$	1	2	Avalanche
BaBar	Trigger	2000	Bakelite	10^{11} - 10^{12}	1	2	Streamer
Belle	Trigger	2200	Glass	$> 10^{12}$	2	2	Streamer
BES III	Trigger	1200	Bakelite	10^9 - 10^{13}	2	2	Streamer
CBM-TOF	Timing	120	Glass	$(3 - 4)\times10^{10}$	10	0.25	Avalanche
CMS	Trigger	2953	Bakelite	$\sim10^{10}$	2	2	Avalanche
COVER-PLASTEX	Timing	16	Bakelite	10^{10}–10^{12}	1	2	Streamer
EAS-TOP	Timing	40	Bakelite	-	1	2	Streamer
FOPI	Timing	6	Glass	10^{12}	4	0.3	Avalanche
HADES	Timing	8	Glass	5×10^{12}	4	0.3	Avalanche
HARP	Timing	10	Glass	10^{13}	4	0.3	Avalanche
L3	Trigger	300	Bakelite	10^{11}	2	2	Streamer
OPERA	Trigger	3200	Bakelite	$>5\times10^{11}$	1	2	Streamer
PHENIX	Trigger	-	Bakelite	10^{10}	2	2	Avalanche
STAR	Timing	50	Glass	10^{12} - 10^{13}	6	0.22	Avalanche
YBJ-ARGO	Trigger	5630	Bakelite	$(0.5 - 1)\times10^{12}$	1	2	Streamer

Table 5.1: Summary of RPC application in some past, present and future experiments [24], [35]

4. They are very robust detectors.

5. They provide good position resolution ($\sim$1 cm in the case of standard RPCs and $\sim$30 μm in the case of micro RPCs).

6. Depending upon the need of an experiment, the design and construction of RPCs can be tuned.

Because of the above mentioned advantages of RPCs, they are increasingly preferred over the other competing technologies for the accelerator, cosmic ray, neutrino and application based experiments for timing or triggering or both purposes. Table 5.1 summarizes the deployment of RPCs in various configurations, modes of operation and application in past, current and

future experiments. Several neutrino physics experiments like OPERA [28], DAYA BAY[29] are using RPCs. RPCs may also find applications in the future neutrino experiments like INO[2], DUNE[3]. Apart from these, the RPCs are also being explored for the detection of γ-rays[30] and neutrons[31] over a large area. The multi-gap RPC may find potential application in medical physics like Positron Emission Tomography (PET) by Time Of Flight (TOF) technique[32]. The details has been discussed in the Chapter 7. RPCs may also find application in muon tomography for cargo containers[33].

In the proposed ICAL experiment in INO in Southern India, the atmospheric neutrino oscillation parameters will be studied. ICAL will consist of a stack of $\sim$151 horizontal layers of $\sim$5.6 cm thick magnetized iron plates separated by $\sim$4 cm gaps which will house the active detector layers. The total size of the ICAL will be $\sim$16 m $\times$ 16 m $\times$ 14.5 m. The overall active detector area will be $\sim$97,500 m^2. Hence, it is desirable that the active detector should be of low cost, modular in construction with elements of a size suitable for mass production, robust, having a time resolution $\sim$ 1 ns and spatial resolution 1 cm. Considering all these factors, the resistive plate chamber (RPC) seems to be the most appropriate choice as the active detector medium in INO-ICAL.

5.5 Towards the development of oil-free bakelite Resistive plate Chamber

In the last few decades, several developmental works has been done with RPCs. We have achieved $\sim$15 ps of time resolution with MRPCs and about a few tens of μm of position resolution with micro-strip RPCs. RPCs are one of the front runners in the usage of gas detectors in large volume experiments. Several high resistive materials have been tried out for their suitability of RPC electrodes, the most successful being glass and bakelite or high pressure paper laminate. Bakelite, also referred as High Pressure Paper Laminate (HPL), sheets are extensively used as RPC electrodes because of the fact that their bulk resistivity can be varied from $\sim 10^8$to $\sim 10^{13}$

Ωcm during the process of manufacturing. There are several other advantages of using bakelite sheets as electrodes like, bakelite RPCs can be operated in both avalanche and streamer mode, depending on the experiment requirement. But the major point of concern of using bakelite sheets is their surface finish. The surface smoothness of the electrodes is a major concern as to develop RPCs as uneven surface can lead to localized intense high electric field which may cause discharges and may lead into serious damage of the electrodes. Coating the inner surface of the electrodes with polymerized oil like, linseed or silicone solved the problem. On the other hand, experiment like BES III has done immense R&D to develop oil-free (without any kind of coating on the electrode surface) bakelite RPCs. We have also taken an initiative to develop oil-free bakelite RPCs for the upcoming INO-ICAL detector. The next Chapter reports the detailed developmental procedure.

5.6 Summary

RPCs, developed in 1981 by R.Santonico and R. Cardarelli, are gaseous detectors extensively used in several high energy physics experiments. They are made up of two high resistive electrodes seperated by a certain distance (gas gap). They work on the principle of gas ionization. They are known for their excellent time resolution, good position resolution, low cost, robust in nature and can be developed over a large area. The electrodes of RPCs are mostly made of either glass or bakelite, each having their own advantages and disadvantages. Based on the charge collected in each signal, there are two modes of operation - avalanche mode and streamer mode. Based on the purpose, they can be classified either as trigger or timing RPCs. Based on the number of gaps, they are classified as single gap, double gap and multi-gap RPCs. They will find application in the upcoming ICAL experiment in INO as both triggering and timing purposes.

Bibliography

[1] R. Santonico, R. Cardarelli, *Development of Resistive Plate Counters*, *Nucl. Instr. and Meth.* **187** (1981) 377.

[2] Thesis of Christian Lippmann, *Detector Physics of Resistive Plate Chambers.*

[3] G. Charpak, *The use of multi wire proportional counters to select and localise charged particles*, *Nucl. Instr. and Meth.* **62** (1968) 262.

[4] J. Keuffel, *Parallel-plate counters and the measurement of very small time intervals*, *Phys. Rev.* **73** (1948) 531.

[5] J. Keuffel, *Parallel plate counters*, *The Review of Scientific Instruments.* **20(3)** (1949) 202-208.

[6] V. Parchomchuk,*A spark counter with large area*, *Nucl. Instr. and Meth.* **93** (1971) 269-276.

[7] Yu. Pestov, *A picosecond time of flight spectrometer for the VEPP-2M based on local-discharge spark counter*, *IYAF-77-78-trans-E.* **20(3)** (1978) SLAC-TRANS-184.

[8] M C S Williams, *Particle identification using time of flight*, *J. Phys. G: Nucl. Part. Phys.* **39** (2012) 123001.

[9] Fabio Sauli, *Gaseous Radiation Detectors, Fundamentals and Applications*, **Cambridge University Press**.

[10] W. R. Leo, *Techniques for Nuclear and Particle Physics Experiments*, **2nd Edition, Springer-Verlag Berlin Heidelberg, 1994**.

[11] G. F. Knoll, *Radiation Detection and Measurement*, **3rd Edition, John Wiley**& **Sons, Inc**.

[12] A. Akimov, *Ceramic PPC technology and performance*, *Nucl. Instr. and Meth. A*, **344** (1994) 120.

[13] A. Arefiev, *Parallel plate chambers: a fast detector for ionizing particles*, *Nucl. Instr. and Meth. A*, **348**, (1994) , 318.

[14] ALICE-TDR-8, *ALICE Time-Of-Flight Technical Design Report*, *CERN/LHCC 2000-012*, **ALICE TDR 8, 2000**.

[15] V. A. Akimov, *A parallel-plate chamber as a detector for time-of-flight measurements Instrum. Exp. Tech.*, **45**, (2002), 493-500.

[16] Archana Sharma, *Summary of RPC 2007 the IX International Workshop Nucl. Instr. and Meth.* **602** (2009) 854.

[17] Christian Lippmann et. al., *Space charge effects in Resistive Plate Chambers Nucl. Instr. and Meth.* **517** (2004) 54 - 76.

[18] P. Fonte et. al., *Applications and New Developments in Resistive Plate Chambers IEEE transactions on nuclear science.* **49** (2002) 881.

[19] R. Santonico, R. Cardarelli, *Progress in resistive plate counters*, *Nucl. Instr. and Meth.* **263**, (1988), 20-25.

[20] E. Cerron Zeballos et. al., *A new type of resistive plate chamber: The multigap RPC* , *Nucl. Instr. and Meth. A* **374**, (1996), 132-135.

[21] E. Cerron Zeballos et. al., *Simulation study on the operation of a multi-gap resistive plate chamber*, *Measurement Science and Technology* **17**, (2006), Number 1.

[22] Werner Riegler et. al., *Detector physics and simulation of resistive plate chambers* , *Nucl. Instr. and Meth. A* **500**, (2003), 144-162.

[23] Crispin Williams, *Latest results from MRPC time resolution*, **http://www.pas.va/content/dam/accademia/pdf/sv119/sv119-williams.pdf**

[24] PhD thesis of Saikat Biswas, *Development of high resolution gas filled detector for high energy physics experiments.*

[25] P. Fonte et. al., *High-resolution RPCs for large TOF systems* , *Nucl. Instr. and Meth. A* **449**, (2000), 295-301.

[26] V.Peskov and P. Fonte, *Applications and New Developments in Resistive Plate Chambers* , *Proc. Intl. Conf. on Position-Sensitive Detectors, London,England, (1999)*

[27] P. Fonte, *Applications and New Developments in Resistive Plate Chambers* , *IEEE Transactions on Nuclear Science* **49**, (2002), 3.

[28] Alessandro Paoloni, *The OPERA RPC system*, *Journal of Instrumentation* **9**, (2014), C10003.

[29] Liehua Ma et. al., *The mass production and quality control of RPCs for the Daya Bay experiment*, *Nucl. Instr. and Meth.* **659**, (2011), 154-160.

[30] P. Camarri et. al., *Performance of the resistive plate chambers in the ARGO-YBJ experiment*, *Nucl. Instr. and Meth.* **572**, (2007), 476-478.

[31] M. Abbrescia et. al., *Resistive plate chamber neutron and gamma sensitivity measurement with a* ^{252}*Cf source*, *Nucl. Instr. and Meth.* **506**, (2003), 101-109.

[32] M. Couceiro et. al., *RPC–PET : Status and perspectives*, *Nucl. Instr. and Meth.* **580**, (2007), 915-918.

[33] P. Baesso, *Toward a RPC-based muon tomography system for cargo containers*, *Journal of Instrumentation* **9**, (2014), C10041.

[34] Zhong He, *Review of the Shockley-Ramo theorem and its application i semicoductor gamma-ray detectors*, *Nucl. Instr. and Meth.* **463**, (2001), 250-267.

[35] PhD thesis of Satyanarayana Bheesette, *Design and Characterisation Studies of Resistive Plate Chambers.*

[36] G. Aielli et. al., *Improving the RPC rate capability*, *Journal of Instrumentation* **11**, (2016).

[37] R. Arnaldi et. al., *Study of resistive plate chambers for the ALICE dimuon spec- trometer*, *Nucl. Phys. B - Proc. Suppl.* **78**, (1999), 84-89.

[38] C. Bacci et. al., *High altitude test of RPCs for the ARGO YBJ experiment*, *Nucl. Instr. Meth. A.* **443**, (2000), 342-345

Chapter 6

Development of Oil-Free Bakelite Resistive Plate Chambers for INO-ICAL[1]

There are two ways to slide easily through life; to believe everything or to doubt everything. Both ways save us from thinking.

A. Korzybski

6.1 Introduction

The Resistive Plate Chamber (RPC)[1], introduced in 1981 by R. Santonico and R. Cardarelli, is a gaseous particle detector based on the principle of "Spark Chamber", utilizing a constant and uniform electric field produced by two parallel electrode plates which are made up of a material with high bulk resistivity. Smooth surface of the electrodes plays an important role in steady operation of the RPC [2]. Surface roughness of RPC electrode is very important towards the production of the electric field after applying the high potential as the sharp pin like edge

[1]The major contents of this chapter are results of the works published in [27], [28], [29].

in the surface morphological structure may vary the electric field significantly. Roughness of the electrode surfaces increases the dark or leakage current and noise or counting rate of the detector. This also causes the aging effect of RPCs. This has been a major problem for bakelite RPCs. In order to avoid this problem, the inner surface of the bakelite electrodes are coated with polymerized linseed or silicone oil. At the same time there has been several efforts in the past few decades to develop bakelite RPCs without any kind of coating by developing suitable bakelite surfaces. We have also put an effort to develop bakelite surfaces without any kind of oil coating. This chapter descibes the detailed development of such a RPC which may be used for the future neutrino experiments like INO-ICAL and DUNE.

6.2 Historical development of oil-free bakelite RPCs :-

RPCs were first introduced in the world of gas detectors in the year 1981 by R. Santonico and R. Cardarelli. The electrodes used in the development of the first RPC were made up of high pressure laminate or commonly referred as bakelite. Ever since, several other high resistive materials have been tried out as electrodes of RPCs. Now a days, the most common materials which are used as RPC electrodes are glass and bakelite. Among the experiments world-wide which use bakelite RPCs, most of them use electrodes treated with linseed oil for their optimum performance. This process has been an essential part and common practice as the physical features like roughness, defects on the uncoated inner surface of the RPC electrodes may cause high leakage current, high noise rate [2] which may result into breakdown of the electrodes [3]. It has been observed that a thin layer of linseed [13] or silicone oil [14] coated on the inner surface of the bakelite electrodes can significantly improve the surface smoothness, thereby greatly improving the performance of the RPCs including the long term stability of the RPC modules.

The surface smoothness of the bakelite electrodes can be controlled during the process of manufacturing of bakelite sheets. A few details of these steps can be found in ref.[3],[18]. As it is very difficult to control the surface morphological structure of the bakelite sheets during their fabrication, coating the inner surface of the electrodes is a suitable solution to optimize the

RPC performance. Treating the inner surfaces of the electrodes, following steps are followed.

1. The RPC gas gaps are filled with a liquid containing linseed oil.
2. The liquid is then drained slowly leaving behind a thin layer of linseed oil on all surfaces inside the gap.
3. The oil layer is then cured by flowing dry air through the gaps of RPCs for tens of hours.

In order to get best results, the above processes are repeated up to three times. But there is a possibility that incompletely uncured linseed oil is left behind inside the gas gap which may cause serious operational problems in RPC, as observed by BaBar RPC system in late 1990's[4],[5]. As the resistivity of the uncured oil is much lower than that of cured oil, the accumulation of uncured oil around the spacers shortens the gas gap. Also, whiskers can grow from regions of incompletely cured linseed oil. These phenomenon may cause heavy discharges under high electric field. In the case of oil-treated RPCs, uncured oil droplets in the form of "stalagmites" [15] have been observed on the inner surface of the bakelite plates. These droplets offer a suitable path to the current through the gas gap leading to high leakage current. The chance of accumulation of these droplets is very high around the spacers of the chamber. It has also been observed that the surface resistivity of the oil-treated bakelite changes during its course of operation. The disadvantages of surface treatment of the electrodes with oil are well documented in [15]. However, these problems have been solved by the use of minimal cured linseed oil [16].

Since 1990's several R&Ds have been done to develop bakelite RPCs without any kind of oil treatment on its surface[17], [3]. These R&Ds were mainly focused to improve the surface quality of the bakelite sheets by using fine paper and melamine resins [3]. However, even after that, the noise rate of the uncoated RPCs were considerably higher compared to the coated RPCs [18]. Hence, in most of the cases it has been noted that the attempts to eliminate the oiling did not give satisfactory results mainly due to significant increase in the noise level of the RPCs [18], [19].

Application of uniform coating on the electrodes adds several complexities in the fabrication procedure. Additionally, the adverse effects of coating on the properties of electrodes are completely eliminated with the use of uncoated surface. Keeping these aspects in mind, we put an effort to develop an oil-free bakelite RPC. This work is a parallel effort towards constructing a large-sized bakelite RPC without any surface treatment.

6.3 Development of oil-free bakelite RPC in VECC, Kolkata

This thesis aims at the development of large sized oil-free bakelite RPC for large neutrino experiments like INO-ICAL. In order to do so, suitable bakelite sheets have to be developed with proper smooth surface quality as the surface morphological structure plays a very important role in the operation of a RPC. A smooth electrode surface not only limits the heavy discharges but also reduces the ageing effect of the detector. For this work, several bakelite samples have been tested for their properties like bulk resistivity, surface resistivity, capability to sustain high voltages. The first criterion that makes the suitability of a high resistive material for development of RPC is its electrical properties like bulk and surface resistivity. The electrical properties should remain constant with the variation of applied high voltage in the operating region. Among the chosen samples, most of them failed in the test. Those samples have shown a significant change in their electrical properties with applied high voltage. Hence, those samples were rejected for the development of RPC. The next section reports the failures and successes of such an effort.

6.3.1 Search for suitable bakelite sample

The electrical properties like bulk and surface resistivities are the first important parameters that define the suitability of any high resistive material towards the development of a RPC [20],[21]. The failure has been reported for a particular sample which has shown consistent behaviour in the electrical properties with the applied high voltage. High resistivity controls the rate capability of the chamber and helps to localize the avalanche. As INO-ICAL will be

using a large number of RPCs, it is important to find a suitable bakelite sample that can make a RPC as well as it should be easily available. We have tested several bakelite samples provided by an Indian company called **Lamtuf Plastics Ltd** for their bulk resistivities as listed in table 6.1. The average thickness of these bakelite sheets were 3 mm. The resistivities have been measured by inserting the sample in between two copper plates of certain dimensions connected to the opposite terminals of the power supply [22]. Table 6.1 summarizes the variation of bulk resistivity with applied high voltage for those samples. Among the tested samples, P100, P200 and P201 grade bakelite sheets had shown a significant drop in the bulk resistivity with high voltage. Hence, these samples were rejected in the first step. Only P301 grade sample was found suitable for the initial development of oil free RPC as the variation was minimal. The bulk and surface resistivity of P301 sample were measured and are shown in Figure 6.1. As seen from the figure, the variation in the electrical properties of the sample is minimal.

Sample (grade)	Variation of high voltage (V)	Change in bulk resistivity (Ωcm)	Result
LPP01 (P100)	100 to 8000	$\sim 10^{9}$ - 10^{6}	Failed
LPP02 (P200)	100 to 8000	$\sim 10^{10}$ - 10^{8}	Failed
LPP02 (P201)	100 to 8000	$\sim 10^{11}$ - 10^{9}	Failed
LPP03 (P301)	100 to 8000	$\sim 10^{13}$ - 10^{12}	Passed

Table 6.1: Change in the bulk resistivity of P-100, P-200, P-201 and P-301 bakelite samples as a function of applied high voltage.

After the successful measurement of the electrical properties of the P301 sample, a small prototype RPC (30 cm $\times$ 30 cm) with a gas gap of 0.2 cm was fabricated, as shown in Figure 6.2. In the first module, the inner surface of the electrodes were not treated with any kind of oil. After the successful fabrication, a gas mixture of Freon:Iso-butane (avalanche mode of operation) in the volume ratio of 95:5 was flown through the detector for $\sim$1 day. The high voltage connections were made to apply high voltages on the respective electrodes and the I-V characteristics had been studied.

Figure 6.3 shows the first I-V curve of the detector. The current readings were noted down

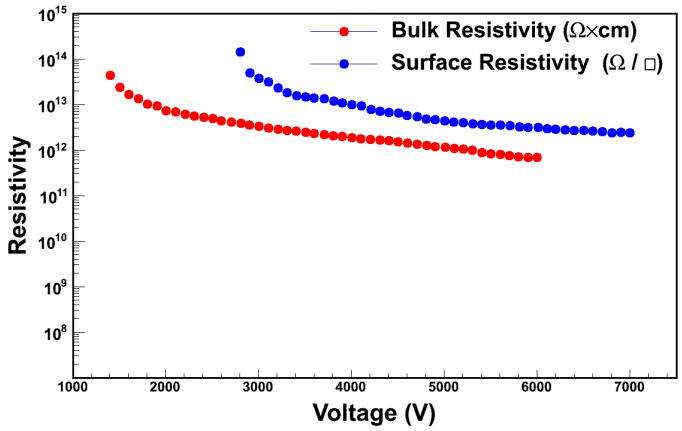

Figure 6.1: *[Colour online] Electrical properties of the P301 bakelite sample as a function of the applied voltage*

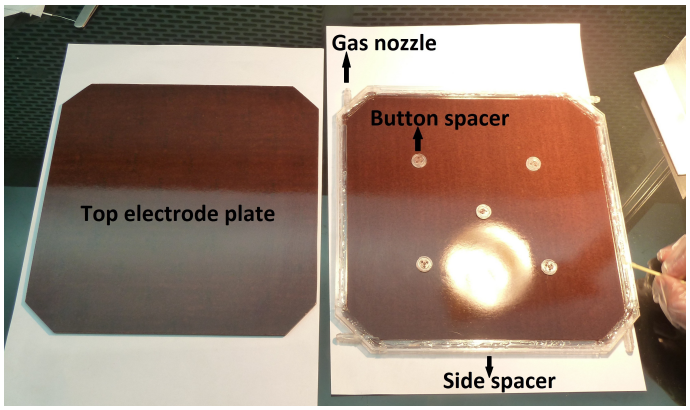

Figure 6.2: *[Colour online] Fabrication of a small (30 cm × 30 cm) bakelite RPC with P301 bakelite sample.*

while ramping up and ramping down of the detector. It is clearly seen that the current values do not match in both the cases and a hysteresis loop is formed. The breakdown voltages also differ from each other by ∼5500 V. The area under this hysteresis loop signifies that the detector stores the applied potential in the form of energy and does not come back to its previous state and the voltage is decreased. The roughness of the electrode surface is a major reason for this kind of effect. Similar effect in I-V test was observed with a gas mixture of Argon:Freon:Iso-butane in a volume ratio of 55:40:5 (streamer mode of operation). Figure 6.4 shows the I-V curve for this

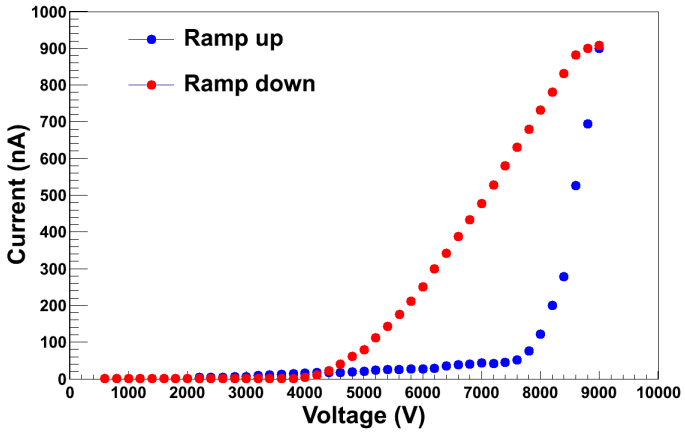

Figure 6.3: *[Colour online] I-V characteristics of small prototype RPC in avalanche mode of operation. This RPC had been fabricated from failed bakelite sample. No silicone oil or any kind of lubricant were applied on the inner surface of the electrodes.*

particular gas mixture.

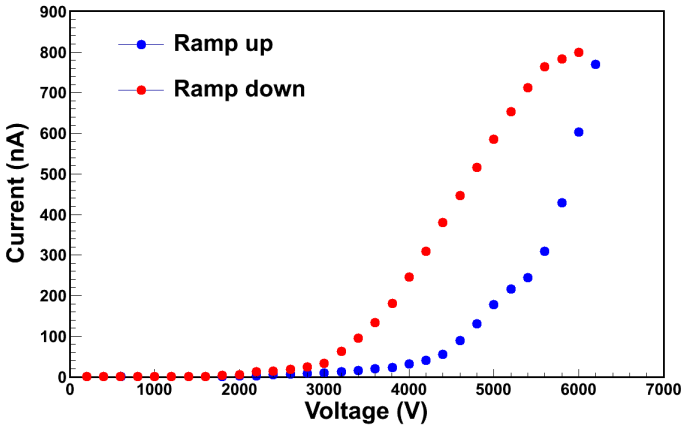

Figure 6.4: *[Colour online] I-V characteristics of small prototype RPC in streamer mode of operation. This RPC had been fabricated from P-301 sample. No silicone oil or any kind of lubricant were applied on the inner surface of the electrodes.*

After it was realized that the surface of the P301 sample was rough, a fresh RPC was fabricated with fresh P301 sample by coating the inner surface of the RPC with a thin layer of silicone oil. Similar procedure was followed and the I-V characteristic of the RPC was studied with a gas mixture of Argon:Freon:Isobutane in a volume ratio of 55:40:5. The I-V curve has been

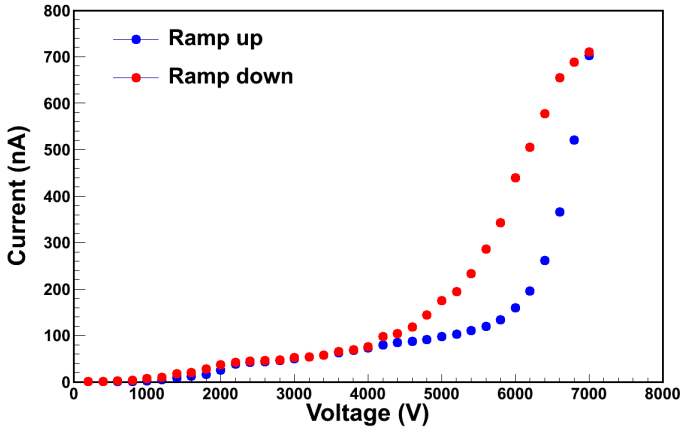

Figure 6.5: *[Colour online] I-V characteristics of small prototype RPC in streamer mode of operation. This RPC had been fabricated from failed bakelite sample. The inner surface of the RPC electrodes were coated with silicone oil.*

shown in Figure 6.5. Similar effect was obtained but with a slight improvement. If Figure 6.4 and 6.5 are compared, then it can be concluded that the area under the hysteresis loop decreased after oil coating. This confirms the fact that the surface roughness of the electrodes may be a major reason for the observed hysteresis loop as oil coating improves the surface quality. Nevertheless, oil coating does not remove the roughness completely and leaves a possibility of producing uncured oil droplets as mentioned in before. Hence, it reduces the area under the hysteresis loop but does not eliminate it completely for this particular bakelite sample.

After the failures of the samples mentioned in Table 6.1 for the development of RPC, the company was approached by providing with the necessary reasons for the failures and was requested to improve the surface morphological structure. After several R&D, the company provided with a new sample (P302 OLTC grade) with improved surface quality. A new 30 cm $\times$ 30 cm RPC was fabricated with the sample. In order to improve the surface finishing, a special grade of paper was used by the company. The following subsection explains the detailed fabrication and test results with cosmic rays of the new RPC.

6.3.2 Fabrication and testing of small (30 cm × 30 cm × 0.2 cm) oil free bakelite RPC

Electrical properties of the bakelite sample and fabrication of small prototype RPC

The electrical properties like bulk resistivity and surface resistivity play an important role for the performance of a RPC which has been well explained in reference [22]. They also determine the rate handling capability of a RPC. For the P302 OLTC grade bakelite, the bulk resistivity was measured as described in reference [22] and the surface resistivity was measure as described in reference [26]. Figure 6.6 shows the measured bulk and surface resistivities of the bakelite sample as a function of the applied high voltage. The average value of the bulk resistivity of the bakelite sample was found to be $\sim 9 \times 10^{11}$ Ωcm whereas the surface resistivity was measured to be $\sim 3 \times 10^{12}$ Ω/□. The values are found to suit the requirements of RPC electrodes [22].

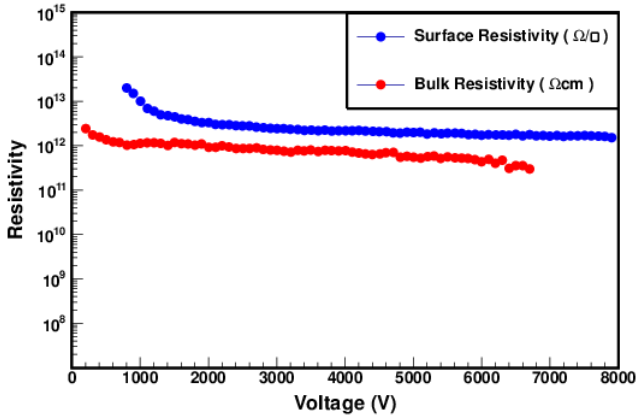

Figure 6.6: *[Colour online] Electrical properties of the bakelite sample as a function of the applied voltage [28].*

A single gap 30 cm × 30 cm × 0.2 cm bakelite RPC from 0.3 cm thick P302 OLTC grade bakelite sheets was fabricated. A gap of 0.2 cm was maintained between these electrodes with the help of 4 button spacers, each of diameter 1 cm and height 0.2 cm and 4 side spacers of length 28 cm and height 0.2 cm along with two gas nozzles. The side spacers, button spacers and gas nozzles were made of polycarbonate material. The outer surfaces of both the electrodes

were painted with conducting black graphite paint mixed with special thinner in 1:1 ratio in order to apply uniform electric field across the plates. Figure 6.7 shows the different components of the fabricated RPC.

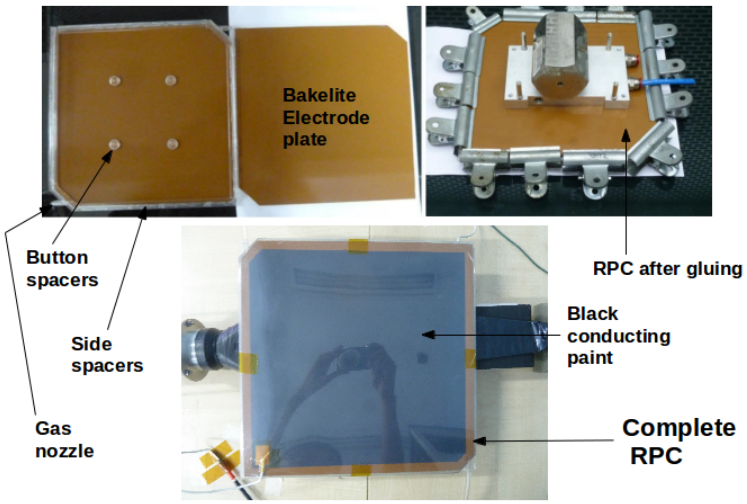

Figure 6.7: *Components and different stages of fabrication of small size (30 cm × 30 cm × 0.2 cm) RPC*

The surface resistance of the painted surfaces of both the electrodes were measured with the help of a 5 cm × 5 cm Aluminum zig. Figure 6.8 and 6.9 shows the resistance profile of both the surfaces. It can be seen form both the above figures that the semi-conductive coating was

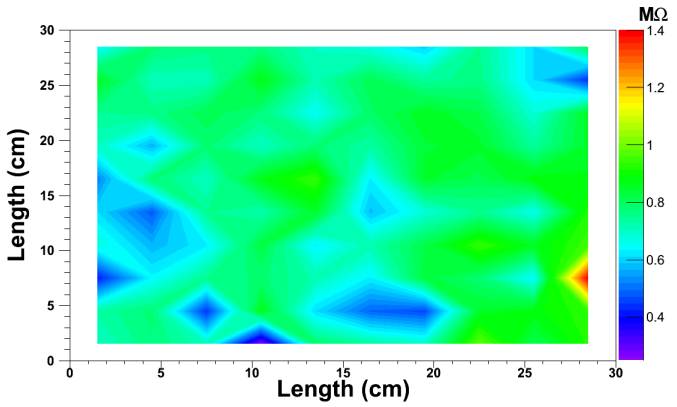

Figure 6.8: *Surface resistance profile of the painted surface of the top electrode.*

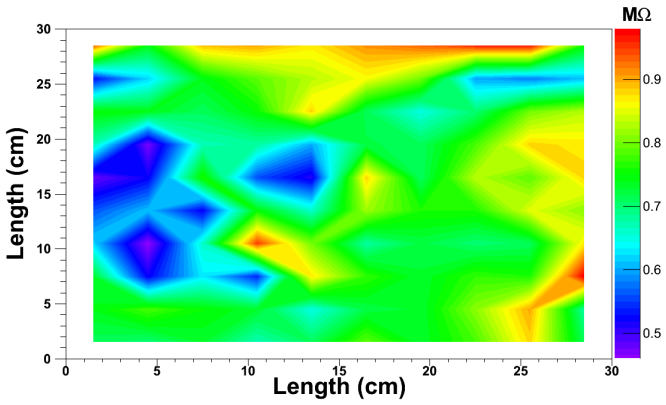

Figure 6.9: *Surface resistance profile of the painted surface of the bottom electrode.*

quite uniform with some variations around the edges of the electrodes. As the painting was done manually with spray gun hence it is quite difficult to remove these variations. After the successful fabrication of the small prototype RPC, it was tested with cosmic rays in a standard cosmic ray test set-up. We have used three plastic scintillators - two paddle scintillators (20 cm $\times$ 8.5 cm) and one finger scintillator (7 cm $\times$ 1.5 cm). The overlap area between the scintillators has been used to obtain the cosmic ray efficiency for a particular set-up.

High voltage (HV) was applied to the chamber using the CAEN N471A module. The current was monitored from the display of the HV supply. The signal from the chamber was tapped with the help of the copper strips of the pick-up panel. The pick up panel consisted of 30 cm $\times$ 3 cm copper strips with a gap of 0.2 cm between them, pasted on a 30 cm $\times$ 30 cm $\times$ 1 cm plate made up of foam and thermocol. A CAEN N841 16 channel Leading Edge Discriminator (LED) has been used to convert the signals from the scintillatos and RPC into logic signals. The coincidence of the three scintillator logic signals form the 3-fold master trigger. Further coincidence with the RPC logic signal forms the four-fold signal. The efficiency is defined as the ratio of the 4-fold counts to the 3-fold counts during a fixed time interval. The average master trigger rate was $\sim$ 0.008 Hz/cm^2. The following subsections discusses the test results.

I-V characteristics and current stability of RPC

The I-V test is the first and important test of a RPC which tells about the health of the detector. This test shows a common feature that the current-voltage curve has two distinctly different slopes. The reason can be explained by the equivalent circuit of RPC, as shown in Figure 6.10.

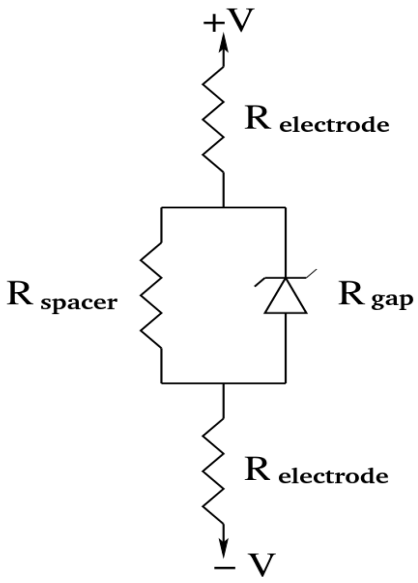

Figure 6.10: *Equivalent electrical circuit of a RPC[24].*

At low voltage region i.e voltages below discharge, the gas gap behaves as an insulator as no avalanches or streamers are formed,

$$R_{gap} \simeq \infty, \qquad and \qquad R_{spacer} \gg R_{electrode} \tag{6.1}$$

Hence,

$$\left.\frac{dV}{dI}\right|_{low\ voltage} = R_{spacer} \tag{6.2}$$

So, the slope of the I-V curve at low voltage region gives the conductance of the spacers. Whereas, at very high voltage region i.e voltages above discharge, the gas gap behaves as a conductor as

large avalanches or streamers are formed,

$$R_{gap} \simeq 0 \tag{6.3}$$

Giving,

$$\left.\frac{dV}{dI}\right|_{high\ voltage} = R_{electrode} \tag{6.4}$$

Hence, the slope of the I-V curve at high voltage region gives the conductance of the electrodes of the RPC.

The variation in the current through the RPC as a function of the applied high voltage was studied. The current values were noted down while ramping up and also ramping down the RPC. Figure 6.11 shows the variation in the current with respect to the applied voltage. It is very clear from the figure that there is no hysteresis loop, as obtained in the I-V curve of RPCs developed from previous bakelite samples (P-301). This signifies that the surface morphological structure of P-302 bakelite sample is suitable for the development of a RPC. The I-V characteristics of the fabricated bakelite RPC has been studied in streamer mode of operation with a gas composition of Argon:Freon(R134a):Iso-butane::55:40:5 as shown in Figure 6.12. The gas flow rate was maintained at ∼12 Standard Cubic Centimeter per Minute (SCCM) giving 1 volume change in ∼15 minutes. Two distinct slopes in the I-V characteristics have been obtained with a breakdown voltage at ∼7000 V (± 3500 V). The RPC has been tested for current stability for ∼50 hrs at 12,000 V (± 6000 V) as shown in Figure 6.13. The current of the chamber was found to be stable over the time period and also thereafter. Prior to observe the current stability, the detector was kept in gas flow with high voltage ramped up, for ∼2 days giving sufficient time for it to stabilize.

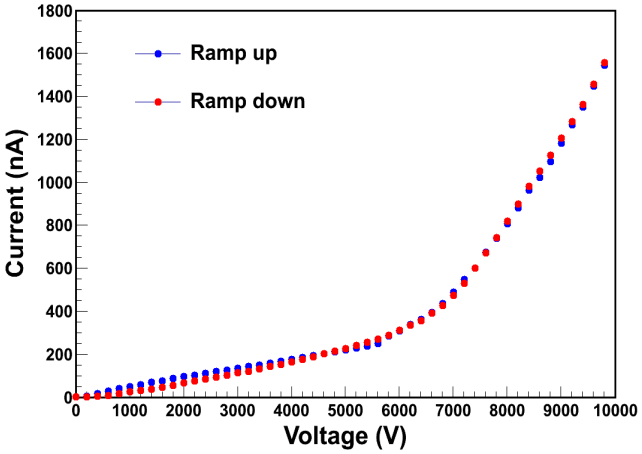

Figure 6.11: *Variation in the current of the RPC as a function of the applied volatge while ramping up and ramping down of the RPC.*

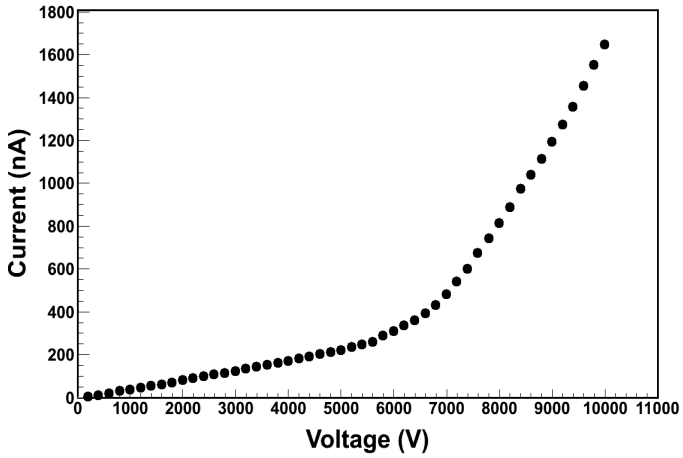

Figure 6.12: *Shows the I-V characteristics of the bakelite RPC.*

Efficiency and noise rate

The efficiency and noise rate of the RPC with cosmic rays have been measured. A signal threshold of 20 mV was applied to all the three scintillators and the RPC. An efficiency plateau was obtained for the RPC beyond 8000 V. The efficiency, as shown in Figure 6.14 was found to be ∼98%. During this test, noise rate of the RPC was also calculated and was found to be ∼1.7 Hz/cm^2 at 9000 V. A linearly varying behaviour of the noise rate with the applied

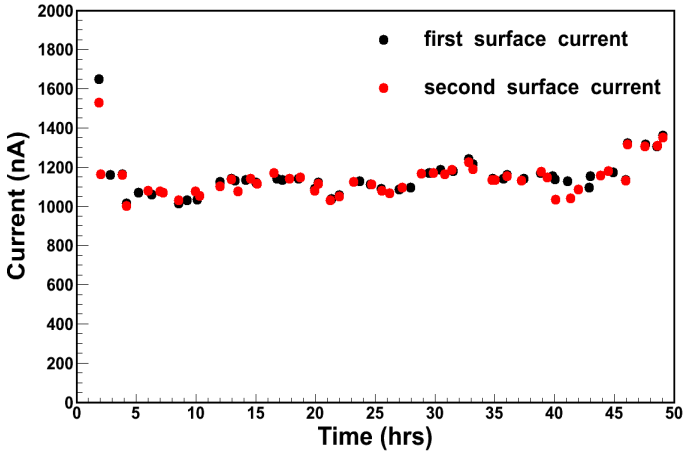

Figure 6.13: *Shows the current stability of the bakelite RPC at ± 6000 V.*

voltage is shown in Figure 6.15. The noise rate is nearly twice than the RPC modules used in existing neutrino experiments [30] due to large argon content in the gas mixture, low threshold and absence of electron quencher in the gas mixture.

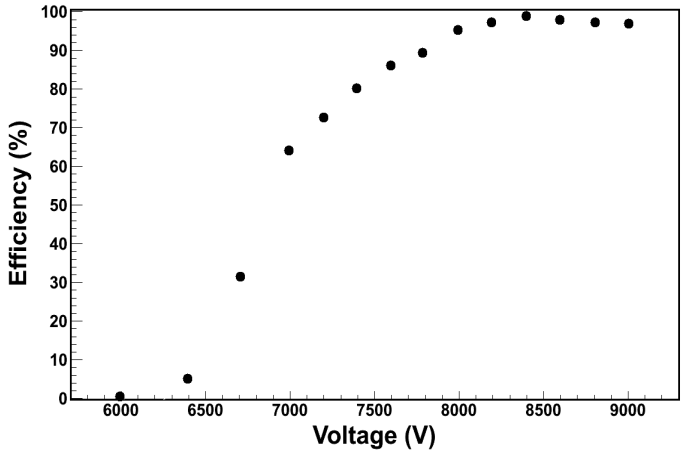

Figure 6.14: *Shows the variation of efficiency with applied high voltage of the fabricated bakelite RPC.*

With the successful results of the small (30 cm × 30 cm × 0.2 cm) bakelite RPC and acceptable values of bulk and surface resistivity of the bakelite sample, we started to develop large size (240 cm × 120 cm × 0.2 cm) bakelite RPC. For this purpose, two bakelite sheets of the same grade (P302 OLTC) of dimension ∼240 cm × 120 cm × 0.3 cm were procured. The

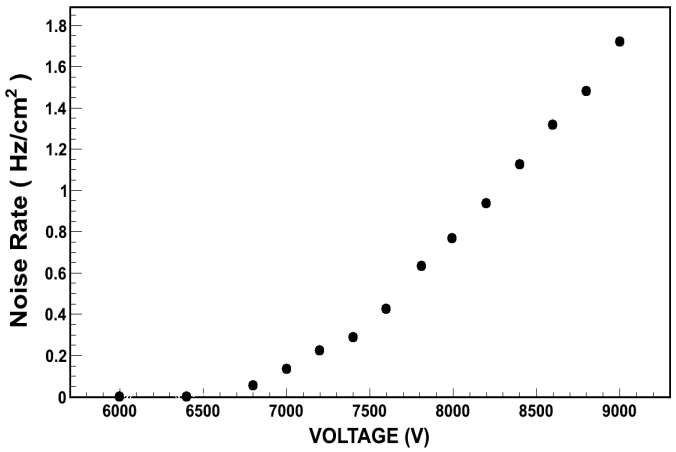

Figure 6.15: *Shows the variation of the noise rate with applied high voltage of the fabricated bakelite RPC.*

following section discusses the development and various test results of the large RPC in details.

6.3.3 Development and testing of large-size (240 cm × 120 cm × 0.2 cm) oil free bakelite RPC

The bakelite electrodes used in the development of a large-size oil-free bakelite RPC are of the same grade and quality as that of the small prototype, discussed in the previous section. The dimensions of the sheets are ∼ 240 cm × 120 cm with a thickness of 0.3 cm. This is the largest dimension of bakelite sheets available in Indian market. Several obstacle were faced during the initial development of such a RPC like improper glue, dimensions and number of button spacers, number of gas nozzles to be used, painting of the electrode surface with semi-conductive paint and so on. These problems led us to carry out further investigations in the respective areas. It so happened that the initial fabrication was unacceptable and the RPC had to be dismantled. Further investigations led to the problems mentioned below.

- How to paint such a large surface area with semi-conductive paint with acceptable uniformity in painting ?

- It was found that the gas flow through the chamber was not proper which led to optimize the number and size of button spacers as well as the number of gas nozzles to be used.
- What about the conductivity of the glue which is used to stick the button spacers, side spacers and gas nozzles ?
- It was experienced that a large and well leveled platform was needed where the RPC had to be fabricated.
- How to provide sufficient mechanical strength to the chamber ?

The following subsections discusses the solutions and detailed development procedure along with the cosmic ray test results.

Electrical properties of different glue samples

The glue applied on top of the spacers while fabricating the chamber primarily provides required mechanical strength at the joints, however, the electrical properties of the glue plays an important role in deciding the chamber properties. Since the glue contributes to leakage current of the RPC, the conductivity of the glue used should be much less than that of the electrodes.

Table 6.2 shows the resin and hardener specifications used in preparing six different glue samples. The bulk resistivity of the glue samples have been measured. Figure 6.16 shows the variation of the bulk resistivity of the samples with the applied voltage. It is seen that the resistivity of most of the glue samples are higher compared to that of the electrodes.

Glue sample	Resin Specifications	Hardener Specifications
Sample-1	Dobekot 520F	Hardener 758
Sample-2	Araldite	Araldite hardener
Sample-3	Dobekot 520F	Hardener 758
Sample-4	Dobekot 520F	Fevitite hardener
Sample-5	Bicron BC-600	Hardener 758
Sample-6	BC-600:Araldite::1:1	BC-600 hardener

Table 6.2: Resin and hardener specifications of different glue samples[28].

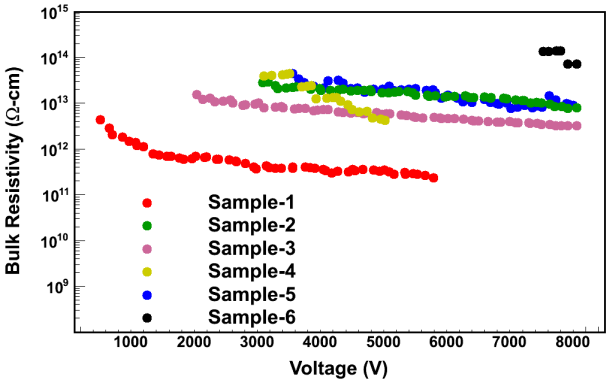

Figure 6.16: *[Colour online] Bulk resistivity of different glue samples as a function of the applied voltage[28].*

Table 6.3 summarizes the mixing proportions (by mass) of the resin and hardener for different glue samples and their respective bulk resistivities. The bulk resistivity of Sample-6 ($\sim 10^{14}$ Ωcm) has been found to be $\sim$100 times higher than that of the bakelite electrode ($\sim 10^{12}$ Ωcm). Hence this particular glue has been used to fabricate the chamber.

Glue sample	Resin:Hardener (by mass)	Average ρ (Ωcm)
Sample-1	1.0 : 0.8	$\sim 6.773 \times 10^{11}$
Sample-2	1.0 : 1.0	$\sim 2.164 \times 10^{13}$
Sample-3	11.0 : 1.0	$\sim 8.376 \times 10^{12}$
Sample-4	21.0 : 2.0	$\sim 2.014 \times 10^{13}$
Sample-5	1 : 1	$\sim 6.62 \times 10^{12}$
Sample-6	4:1	$\sim 1.157 \times 10^{14}$

Table 6.3: Mixing ratio and bulk resistivity (ρ) of different glue samples[28].

Fabrication of the chamber

The fabrication of such a large-sized oil-free chamber has several challenges which include

(a) maintaining the planarity of such large-sized electrodes (b) uniformity in coating the surface with semi-conducting paint (c) preventing the electrodes from sagging by using spacers at proper locations (d) ensuring continuous and uniform gas flow through the detector (e) proper

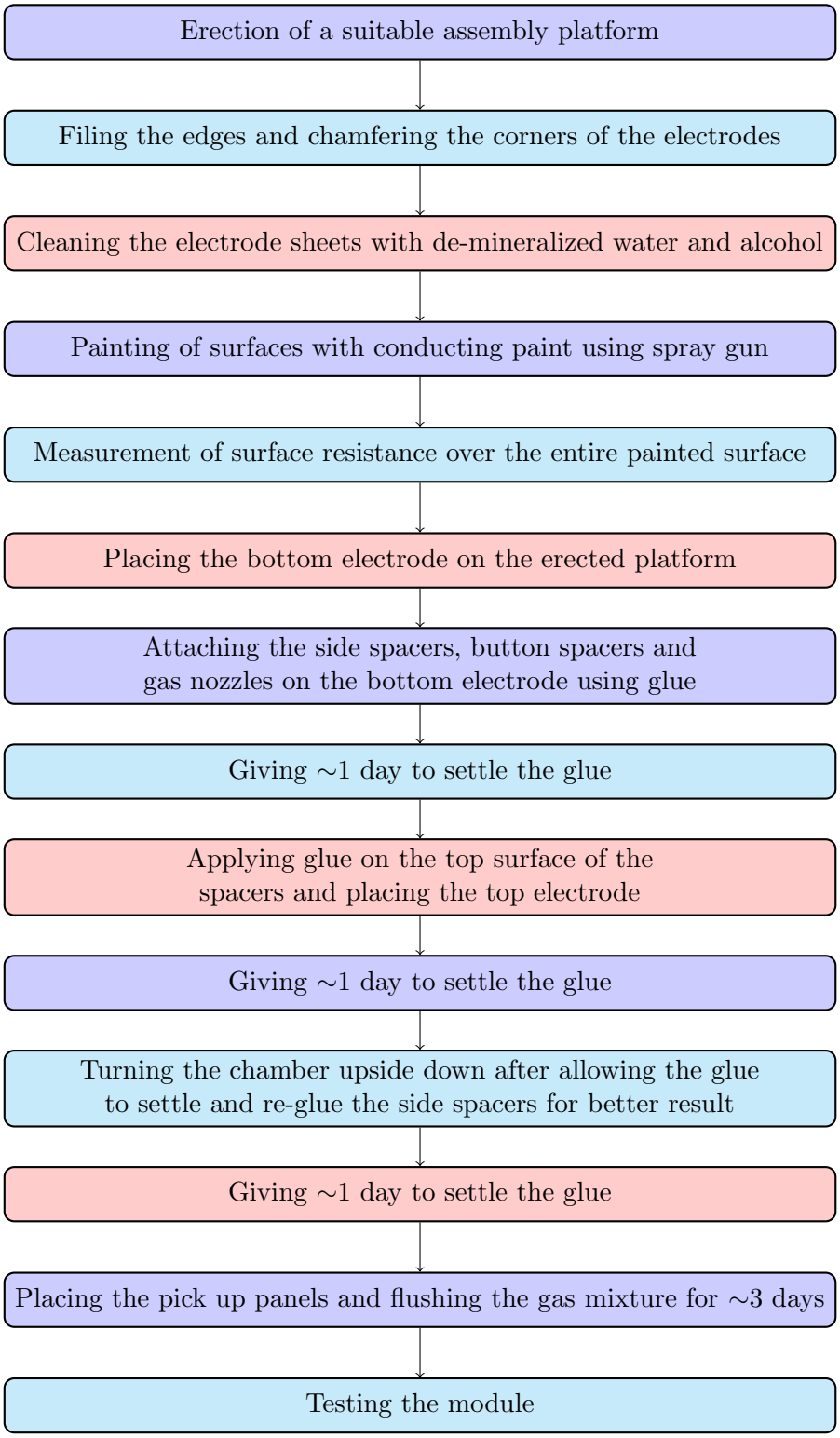

Figure 6.17: *Flow-chart of steps followed during fabricating of large RPC*

sealing of the chamber to ensure the detector is gas-tight. In this section how these challenges were overcome during the fabrication procedure have been discussed. The fabrication procedure consisted of the following steps (a) erection of a suitable assembly platform (b) filing the edges and chamfering the corners of the electrodes (c) cleaning of the electrodes (d) painting of the electrodes with semi-conducting paint (e) measurement of leveling of the electrodes (f) pasting the spacers on the lower electrode and application of glue (g) installation of the upper electrode. For the procedure of oil coating the electrodes, a step is likely to be added in between (c) and (d). For uniform oil coating of such a large surface, a specialized jig was to be made and specialized coating procedure required to be adopted. This becomes an additional step which we avoided by not using any kind of oil. Figure 6.17 shows various steps involved in the fabrication procedure of the RPC in the form of a flow chart. During the fabrication of the RPC, the electrode sheets have been kept on a well leveled platform. In order to maintain a constant gas gap, we used two types of spacers- side spacers and button spacers. These spacers have been fixed on the bakelite sheets with the help of the chosen glue. The button spacers helped to maintain the gas gap while the side spacers additionally helped to seal the chamber from all sides. For such a large-sized RPC, the spacers served the important purpose of providing mechanical support along with defining the gas gap. The surface area of the spacers in contact with the electrodes should be adequate enough to provide excellent mechanical strength to the RPC. The option was to increase either the number or the surface area of the button spacers. Initially, the number of button spacers was increased which led to the accumulation of gas in certain regions of the chamber. The enhanced gas pressure in these regions led to the popping out of the button spacers. Therefore, it has been decided to increase the area of each button spacer. A similar problem, bulging of the chamber due to accumulation of gas was seen initially when there were two gas inlets and two gas outlets. A change in the number of gas inlets and outlets from two to four helped to solve the problem. Also, 1.5 cm broad polycarbonate strips of proper length were pasted along the edges of the electrodes to ensure sufficient mechanical support to the chamber.

In the discussions to follow, some of the steps of fabrication have been described in detail.

Leveling measurement

In order to fabricate such a large RPC, a platform of good planarity and of comparable dimensions as that of the chamber was needed. A good, plane platform ensures that the bakelite sheets do not sag and the spacers stick properly onto both the electrodes. We built a special platform placing cardboard sheets, foam and a thick (2 cm) glass plate of dimensions ∼(240 cm × 120 cm) on top of each other. These components ensured a well leveled surface for the assembly of the chamber. 128 different locations were marked on the bottom electrode in the form a (16 × 8) matrix and the local heights of the electrode at those positions were measured with the help of a dial gauge indicator. After gluing the button spacers on those 128 locations, the local heights of the glued buttons pasted on the bottom electrode were measured, the distribution of which is illustrated in Figure 6.19. It is seen from Figure 6.19 that the gap thickness remains uniform.

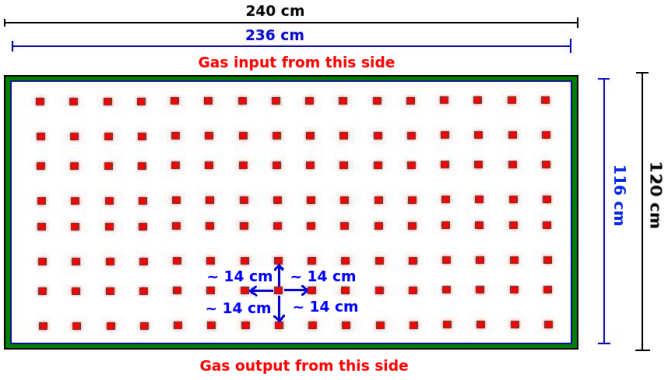

Figure 6.18: *[Colour online][Not to scale] A schematic view of the side spacers and button spacers pasted on the bottom electrode. The green coloured boundary and the small red rectangles show the locartions of the side and button spacers respectively. There are 4 gas input and 4 gas output channels.*

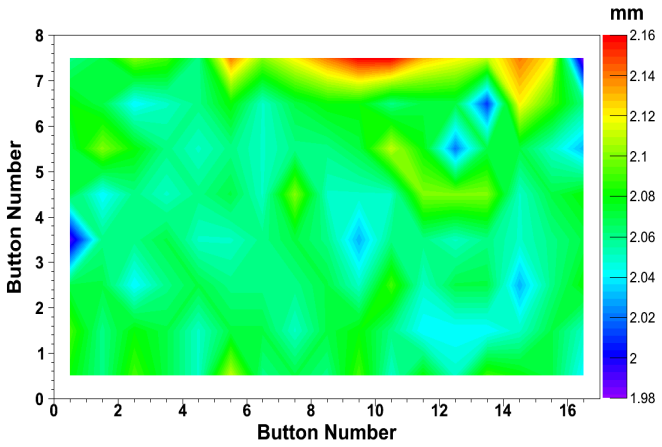

Figure 6.19: *[Colour online] Variation of local height (mm) of glue and button spacers pasted on the lower bakelite sheet[28].*

Assembly of the chamber

As a first step of the preparation of the electrodes, all the edges of both the bakelite sheets were filed properly for smoothening. All the surfaces of both the sheets were then properly cleaned with de-mineralized water and alcohol. After cleaning the sheets, one surface of each sheet was spray-painted with a black semi-conducting paint mixed in the ratio 1:1 by volume with a special dry thinner, both manufactured by Kansai Nerolac, India. The resistance profile of the painted surfaces was measured with the help of a jig made of two brass rods of 9 cm length, separated by a distance of 9 cm from each other. Figure 6.20 and Figure 6.21 show the surface resistivity profile of the painted surfaces of the two electrodes.

Figure 6.22 and Figure 6.23 show the uniformity of painting on the two surfaces in terms of the distribution of the measured resistivities. Even though the RMS values of the two distributions (31% and 25%) indicate relatively larger variation, the deviations are mostly at the edges where the paints are relatively non-uniform at the end of the spray-gun runs. The RMS widths are ∼5% and ∼6% after excluding the tails. The applied field is therefore expected to be uniform over the entire area.

Two copper tapes each of dimension (16 cm × 2.5 cm) were pasted at the edges of the

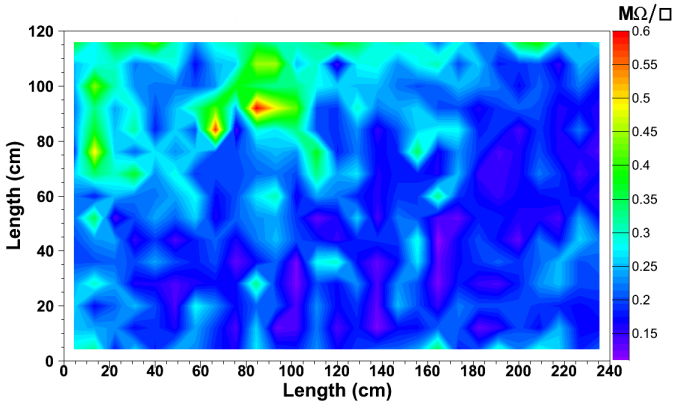

Figure 6.20: *[Colour online] Surface resistivity profile of the painted surface of the lower electrode[28].*

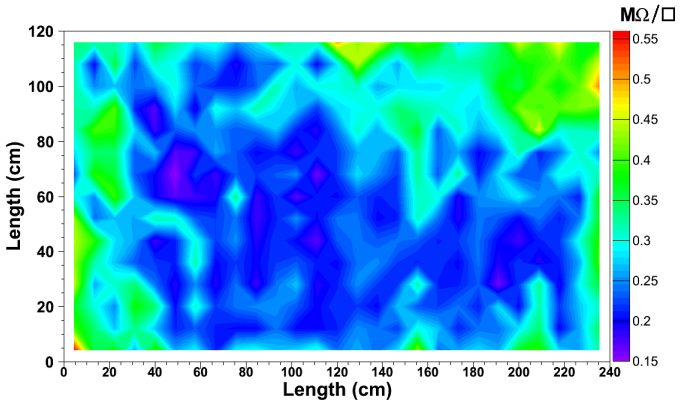

Figure 6.21: *[Colour online] Surface resistivity profile of the painted surface of the upper electrode[28].*

painted surfaces of the electrodes. The tapes are used to apply high voltages on the surfaces. The painted surfaces were then isolated properly with mylar sheets and kapton tapes. The side spacers, button spacers and the gas nozzles were glued subsequently. A total of 128 button spacers each of size 1.5 cm $\times$ 1 cm , 6 side spacers each of $\sim$80 cm in length, 8 gas nozzles (4 for gas input and 4 for gas output) and 2 side spacers each of $\sim$120 cm in length have been used. The distance between any two button spacer is $\sim$14 cm. Some of the components have been illustrated in Figure 6.24.

The upper electrode was installed after the application of glue on top of all the spacers. A

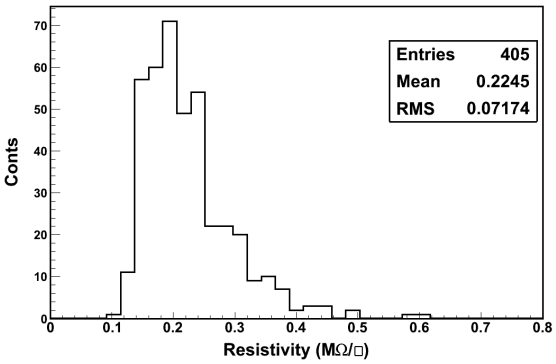

Figure 6.22: *Surface resistivity distribution of the lower bakelite surface[28].*

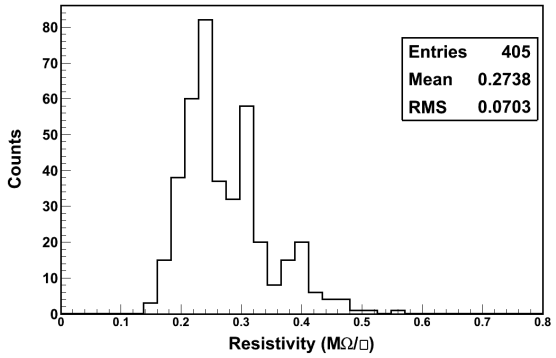

Figure 6.23: *Surface resistivity distribution of the upper bakelite surface[28].*

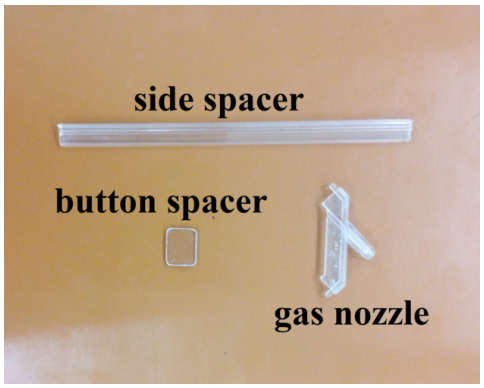

Figure 6.24: *[Colour online] Components (not to scale) used in the fabrication of large bakelite RPC. The side spacer is a sample piece of the large side spacers used[28].*

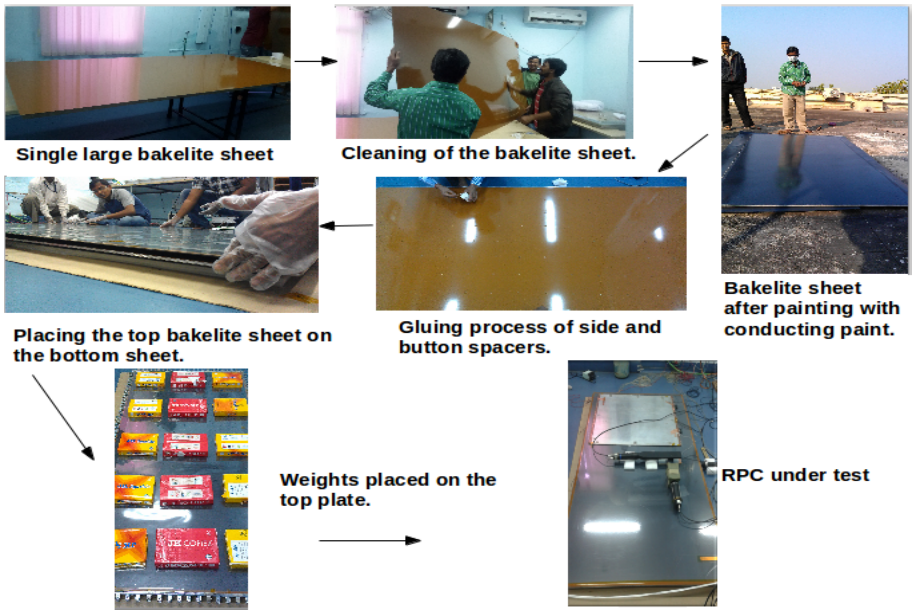

Figure 6.25: *[Colour online] Various steps involved during the development of large oil-free bakelite RPC.*

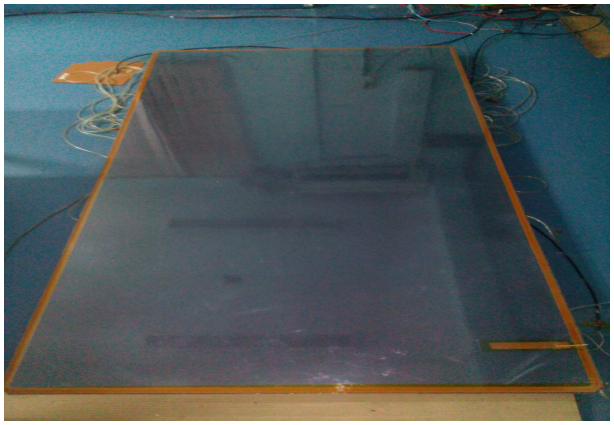

Figure 6.26: *[Colour online] Photograph of the large bakelite RPC[28].*

number of weights (12) each of $\sim$ 2.350 kg, placed over the mylar surface on the top electrode and kept for one day to ensure better clinging. We then re-glued the side spacers to ensure gas-tightness of the chamber. The chamber was then ready for testing with gas and High Voltage. Figure 6.25 pictorially shows the steps involved in the development of the RPC. Figure 6.26

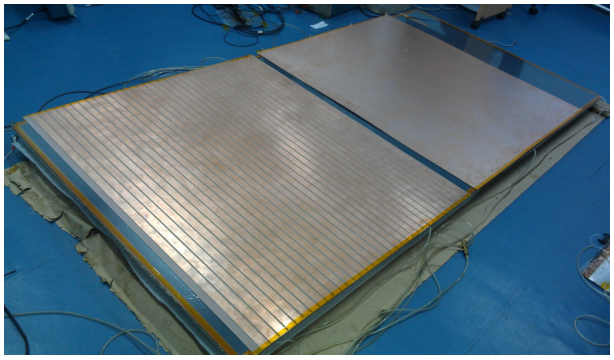

Figure 6.27: *[Colour online] Photograph of the large bakelite RPC with pick-up panel[28].*

shows the photograph of the complete RPC and Figure 6.27 shows the complete RPC with the pick-up panels on it. The pick-up panels are made of ∼(125 cm × 105 cm × 0.15 cm) FR4 sheet sandwiched between ∼(125 cm × 105 cm × 0.0035 cm) copper sheets. The copper pick-up strips are 2.5 cm in width, with a gap of 0.2 cm between adjacent strips.

Cosmic ray Test set-up

The RPC has been tested with cosmic rays in a standard test set-up. We have used three plastic scintillators - two paddle scintillators (20 cm × 8.5 cm) and one finger scintillator (7 cm × 1.5 cm). The overlap area between the scintillators has been used to obtain the cosmic ray efficiency for a particular set-up.

High voltage (HV) was applied to the chamber using the CAEN A1832PE and A1832NE modules in the CAEN SY1527 crate. The current was monitored from the panel of the HV supply. The signal from the chamber was tapped with the help of LEMO connectors soldered on the copper strips of the pick-up panel. A CANBERRA QUAD CFD 454 constant fraction discriminator (CFD) has been used to digitize the signals from the scintillators with a threshold of -20 mV and the RPC. The coincidence of the three scintillator logic signals form the 3-fold master trigger. Further coincidence with the RPC logic signal forms the four-fold signal. The efficiency is defined as the ratio of the 4-fold counts to the 3-fold counts during a fixed time

interval. For timing measurements, the master trigger i.e. 3-fold was connected to the TDC-START and the RPC logic signal was sent to the TDC-STOP after a fixed delay. A CAMAC based data acquisition system has been used in our setup. The average master trigger rate was $\sim$ 0.008 Hz/cm^2.

Test results and discussions

During the entire testing period, the laboratory temperature has been maintained at $\sim$ 20°C and the relative humidity has been maintained at $\sim$45% - 55%. All the tests have been done in the streamer mode of operation of the RPC with a gas composition of Argon:Freon(R134a):Isobutane::34:57:9 by volume. A typical gas flow rate of $\sim$0.75 liters/hour has been maintained over the entire test period resulting in $\sim$3 changes of gas volume per day. The current of the detector has remained stable over the period of $\sim$120 days during which the chamber has remained in operation.

I-V characteristics

The I-V characteristics of the fabricated bakelite RPC is shown in Figure 6.28. Two distinct slopes in the I-V characteristics have been obtained with a breakdown voltage at $\sim$7000 V. From the Ohmic part, the calculated bulk resistivity of the chamber was found to be 1.72×10^{13} Ωcm.

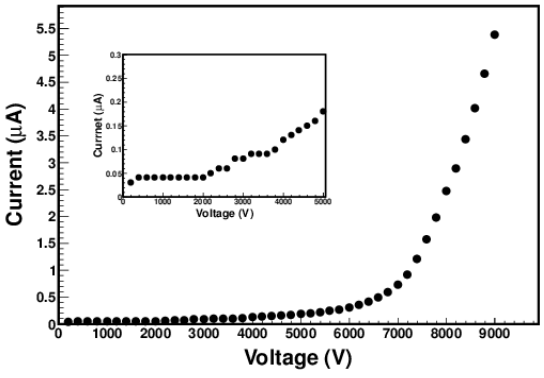

Figure 6.28: *I-V characteristics of the chamber. The figure in the inset shows the I-V characteristics at low voltage region[28].*

Efficiency and noise rate

We have studied the efficiency and the noise rate of the chamber at a signal threshold of -20 mV. Figure 6.29 shows the variation of efficiency with the total applied voltage showing a plateau of >95% above 8400 V. The noise rate variation as a function of the applied voltage is shown in Figure 6.30. During this test, the noise rate of the RPC has been found to be $\sim$0.75 Hz/cm^2 at 9000 V. The noise rate is comparable to the value reported in [14].

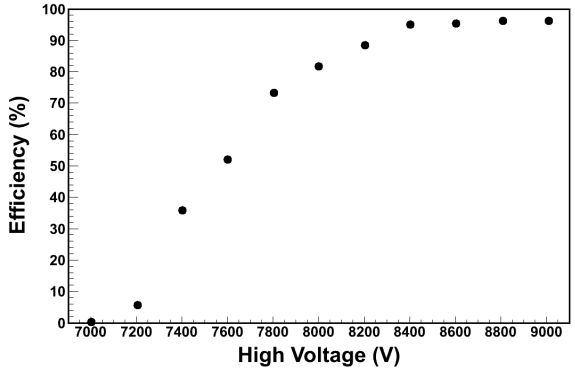

Figure 6.29: *Efficiency of the chamber as a function of the applied voltage. The error bars are within the marker size[28].*

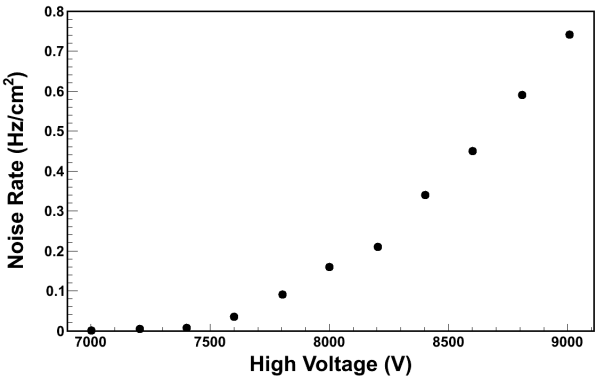

Figure 6.30: *Noise rate of the chamber as a function of the applied voltage. The error bars are within the marker size[28].*

The efficiency of the chamber has been measured at 16 different locations of the detector at 9000 V, 8 at the edges of the RPC and 8 away from the edges. Figure 6.31 shows these locations

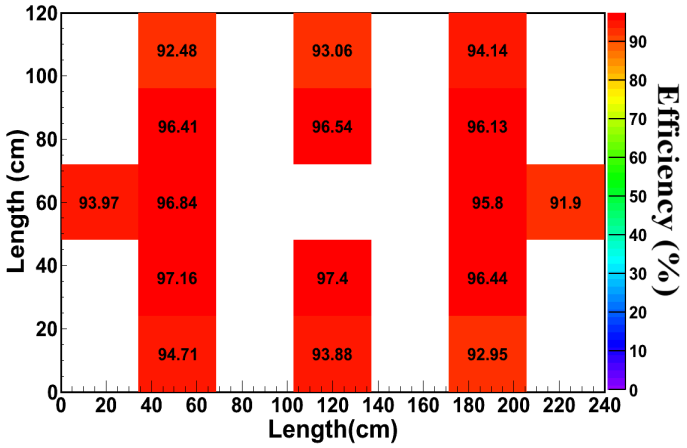

Figure 6.31: *[Colour online] Locations on the RPC plane where efficiencies have been measured, with the measured efficiency values[28].*

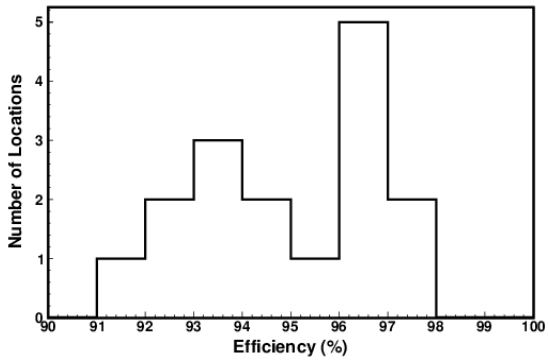

Figure 6.32: *Efficiency measurement at various locations on the RPC surface[28].*

over the RPC surface with the measured efficiency values and Figure 6.32 shows the distribution of efficiency measured at these locations. The figure clearly shows two distinct groups, the edges of the RPC are relatively low efficient as the probability of distortion of the electric field and the non-uniformity of gas-flow are higher at these regions. The average efficiency is found to be >95%.

Time resolution

The time resolution of the RPC has been measured only at a central location of the chamber with the 16 channel PHILIPS SCIENTIFIC 7186 TDC module. Figure 6.33 shows the uncorrected time spectra of the RPC at 9000 V.

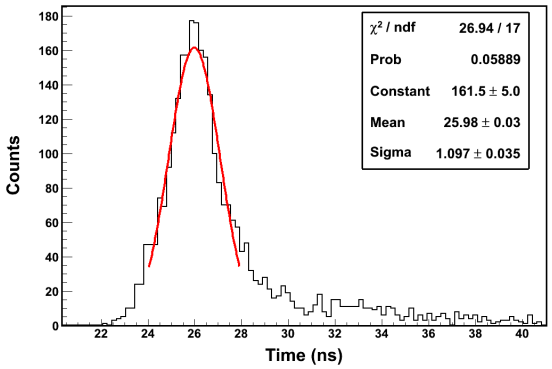

Figure 6.33: *[Colour online] Raw TDC spectra of the RPC at 9000 V. The red curve shows the Gaussian fit[28].*

The final RPC time resolution ($\sigma_{RPC}^{corrected}$) has been extracted from the Gaussian fit after removing the contribution of the three scintillators [23]. Figure 6.34 shows the variation of time resolution ($\sigma_{RPC}^{corrected}$) of the large RPC as a function of the applied voltage. The best value of the time resolution has been found to be ∼0.83 ns at 9000 V which is comparable to the values reported in [1],[25]. From Figure 6.34 it is clearly seen that the time resolution of the RPC improves with increasing high voltage, as expected. But further increase of the high voltage may worsen the time resolution.

The above tests were done within a period of ∼ 1 month. During the entire testing period the current of the chamber was monitored. The bulk resistivity of the chamber was calculated from the monitored current. An abrupt behaviour in the chamber current results in sudden change in the chamber bulk resistivity. Figure 6.35 shows the variation of bulk resistivity of the chamber during the testing period. The variation of efficiency, temperature and relative humidity during the testing period is shown in Figure 6.36.

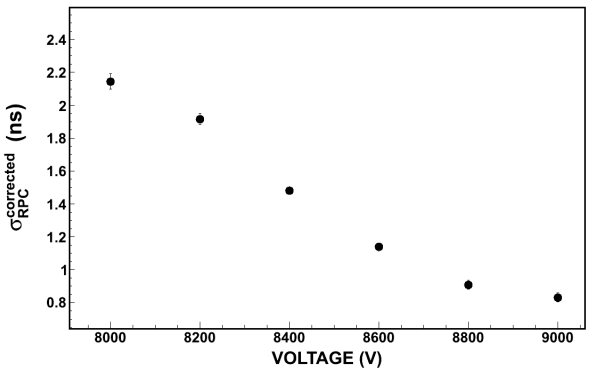

Figure 6.34: *Time resolution ($\sigma_{RPC}^{corrected}$) as a function of the applied voltage[28].*

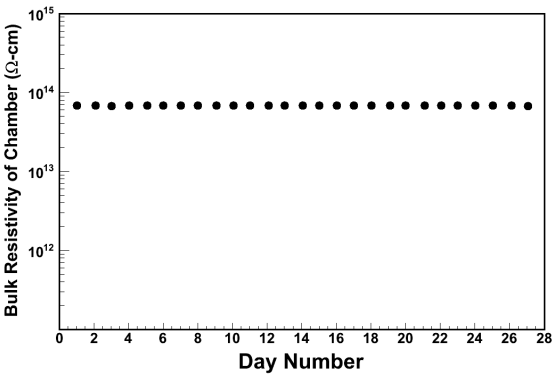

Figure 6.35: *[Colour online] Variation of bulk resistivity of the chamber with time.*

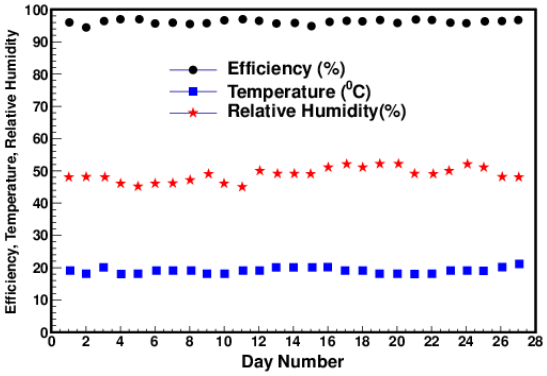

Figure 6.36: *[Colour online] variation of efficiency, temperature and relative humidity with time. The error bars of efficiencies are within the marker size.*

6.3.4 Long term performance testing of large oil-free bakelite RPC :-

After the successful development of the large sized oil-free bakelite RPC, the long term performance of its various parameters were also studied. The long term operation of a RPC may cause ageing problems in the detector due to several reasons like the variation of the electrode resistivity, the integrated charge. In general there are three reasons of ageing effects in a RPC - ageing of the electrode material, aging due to the integrated charge generated in the gas gap which results in the increase in current in the detector and ageing due to irradiation on the detector. However, for low rate neutrino experiments like INO, ageing due to irradiation might not be significant but ageing due to the others remain a major issue. Increase in the leakage current, bulk resistivity of the chamber, reduction in efficiency are the prominent symptoms of an aged RPC. It is therefore important to perform the long term test of the detector as in an upcoming large underground neutrino experiment like INO-ICAL, the RPCs will run for several years.

After the RPC was initially tested for its various parameters like I-V characteristics, efficiency, time resolution, noise rate and so on, the detector was kept in gas flow with high voltage ON at overall 9000 V ($\pm$ 4500 V) for $\sim$ 8 months i.e from May-2015 to December-2015. Then, for the next two months the long term performance of the RPC was monitored continuously. The same scintillator based cosmic ray test set up was used for the test. All the electronics and gas flow configuration was the same as discussed before. During the entire testing period, the laboratory temperature has been maintained at $\sim$ 10°C and the relative humidity has been maintained at $\sim$35% - 40%. For long term performance studies, the chamber was operated at 9000 V with a signal threshold of -20 mV. The following subsections discuss the same starting with the current stability followed by the bulk resistivity, efficiency, noise rate and time resolution measurement of the chamber.

Before starting the long term performance test, the variation of efficiency and noise rate of the chamber as a function of applied high voltage was established but at different signal threshold and compared with the previous results.

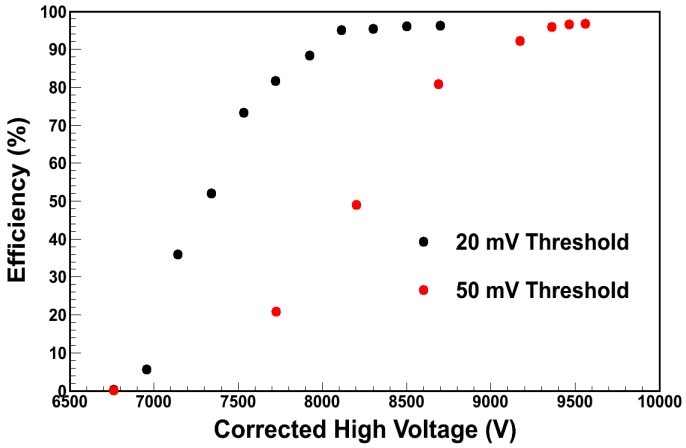

Figure 6.37: *[Colour online] Comparison of cosmic ray detection efficiency of the RPC at different thresholds. The error bars are within the marker size [29].*

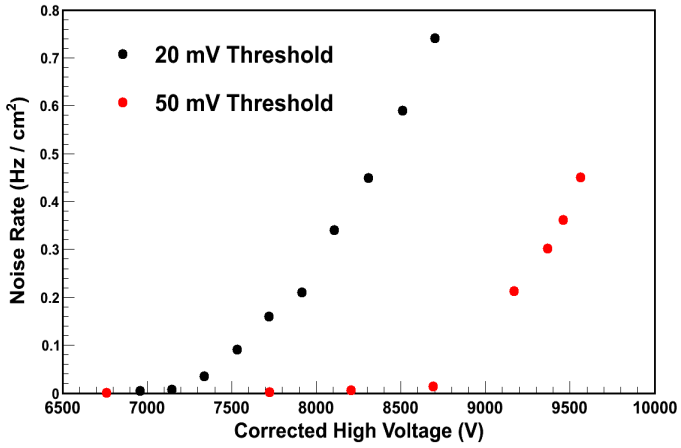

Figure 6.38: *[Colour online] Comparison of noise rate of the RPC at different thresholds. The error bars are within the marker size [29].*

From Figure 6.37, it is seen that the plateau was reached at >8400 V and ≥9700 V with an efficiency value of >95% with a threshold of -20 mV and -50 mV respectively. Figure 6.38 shows that the noise rates of the chamber were found to be ∼0.75 Hz/cm^2 and ∼0.40 Hz/cm^2 with a threshold of -20 mV and -50 mV respectively. From both the figures, it is quite clear that the efficiency and noise rate curves shift to the right with an increase in the threshold, which is as expected, as the genuine but low amplitude signals are being cut off.

Current stability

Figure 6.39 shows the variation in the electrode current for both the electrodes. The top and middle figures show the current variation for the first and second electrodes respectively whereas the bottom figure shows the average current of both the electrodes. The bulk resistivity of the chamber was calculated from the average current values which is shown in Figure 6.40. The bulk resistivity of the chamber was found to be $\sim 9 \times 10^{13}$ Ωcm.

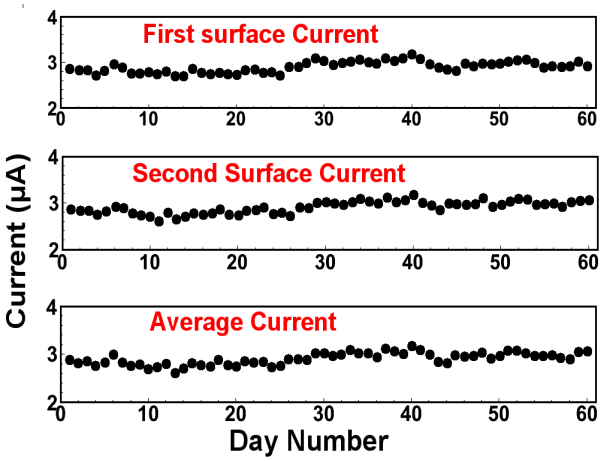

Figure 6.39: *Current stability of the electrodes of the chamber over a peroid of 60 days [29].*

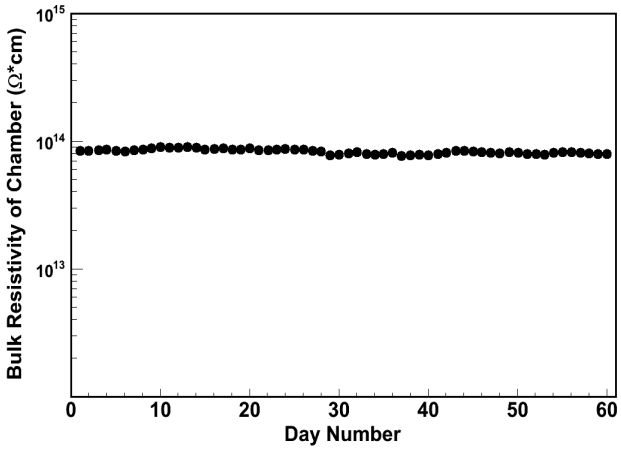

Figure 6.40: *[Colour online] Variation of bulk resistivity of the chamber with time [29].*

Efficiency and noise rate

The efficiency and noise rate of the chamber were also monitored for 60 days. The values of efficiency and noise rate have been shown in Figure 6.41 and Figure 6.42 respectively. The efficiency and noise rate of the chamber was found to be >95% and $\sim$ 0.75 Hz/cm^2 respectively. Both remained quite stable over the entire testing period.

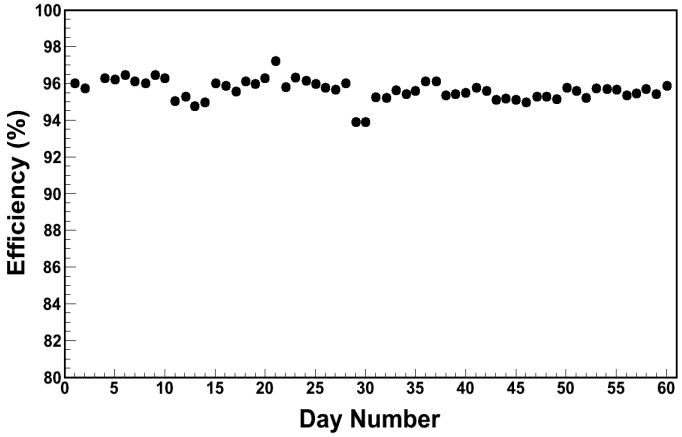

Figure 6.41: *Efficiency of the chamber over a period of 60 days. The error bars are within the marker size [29].*

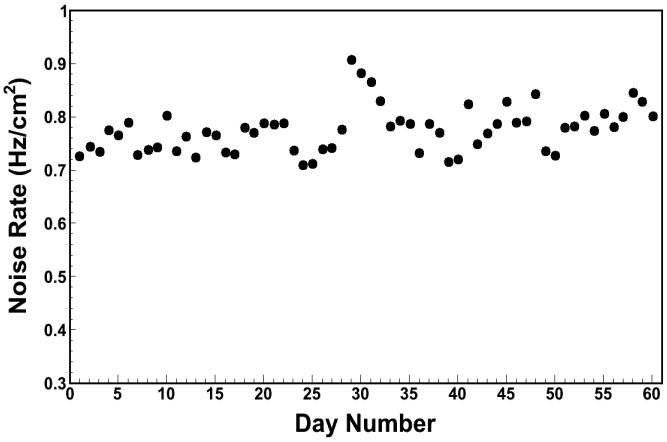

Figure 6.42: *[Colour online] Noise rate of the chamber over a period of 60 days. The error bars are within the marker size [29].*

Time resolution

Figure 6.43 shows the variation of time resolution (σ) over the entire testing period. We have taken one TDC spectra in a week. The details of the time resolution (σ) calculations have been discussed in reference [28]. The average time resolution of the chamber was found to be $\sim$ 0.83 ns.

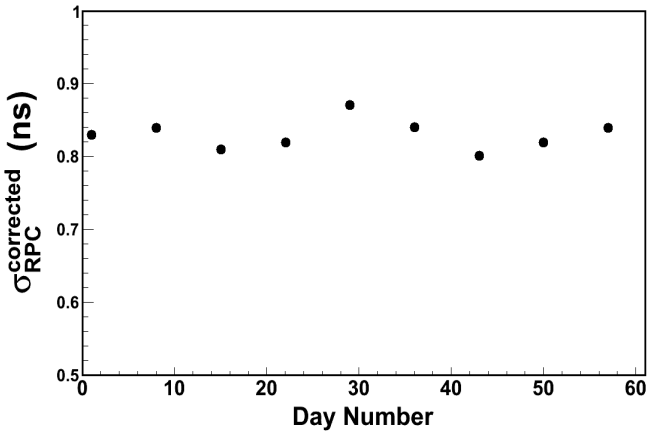

Figure 6.43: *[Colour online] Time resolution (σ) of the chamber over a period of 60 days [29].*

6.4 Summary

A suitable bakelite sample was found for the development of a RPC. A small prototype (30 cm $\times$ 30 cm) single gap RPC with 2 mm gas gap was successfully developed without using any kind of oil on the inner surface of the electrode plates. This prototype RPC showed an efficiency of $\sim$98% in the operating region when tested with cosmic rays in streamer mode of operation. Afterwards, A large sized (240 cm $\times$ 120 cm) oil-free RPC with a gas gap of 2 mm was developed which might find its application in ICAL experiment. Special care was taken during the fabrication process of the RPC. Several glue samples were made and tested in order to find the suitable glue for the development of the RPC. On testing with cosmic rays, it showed an efficiency >95%, noise rate of $\sim$0.75 Hz/cm^2 and time resolution of $\sim$0.830 nano-seconds at

a signal threshold of -20 mV in its central region in streamer mode of operation. The efficiencies at different locations of the RPC were also measured. The detector parameters like current, bulk resistivity, efficiency and time resolution were monitored continuously over a period of 60 days and were found to be stable.

Bibliography

[1] R. Santonico, R. Cardarelli, *Development of Resistive Plate Counters*, *Nucl. Instr. and Meth.* **187** (1981) 377.

[2] Changguo Lu et. al., *RPC electrode material study*, *Nucl. Instr. and Meth.* **602** (2009) 761.

[3] ZHANG J et al., *A new surface treatment for the prototype RPCs of the BESIII spectrometer*, *Nucl. Instrum. Methods A*, **540** (2005), 102.

[4] F. Anulli et al., *The BaBar instrumented flux return performance: lessons learned*, *Nucl. Instr. and Meth. A*, **494** ,(2002), 455.

[5] F. Anulli et al., *Resistive Plate Chamber Performance in the BaBar IFR System*, *IEEE Trans. Nucl. Sci.*, **49** ,(2002), 3.

[6] The Muon Project, Technical Design Report, CMS, CERN/LHCC 97-32, CMS TDR-3.

[7] ATLAS Muon Spectrometer, Technical Design Report, ATLAS, CERN/LHCC 97-22.

[8] Belle-II Technical Design Report, KEK Report 2010-1, October 2010-1.

[9] A. Zallo et al., *The BaBar RPC system*, *Nucl. Instr. and Meth. A*, **456**, (2000), 117-120, F. Anulli et al., *Performances of RPCs in the BaBar experiment*, *Nucl. Instr. and Meth. A*, **515** ,(2003), 322-327.

[10] M. Ablikim et al., *Design and construction of the BESIII detector*, *Nucl. Instr. and Meth. A*, **614**, (2010), 345-399.

[11] INO Project Report, INO/2006/01, http://www.ino.tifr.res.in/ino//OpenReports/INOReport.pdf

[12] http://www.dunescience.org/

[13] M. Abbrescia, et al., *Effect of the linseed oil surface treatment on the performance of resistive plate chambers*, *Nucl. Instrum. Methods A*, **394**, (1997), 13-20.

[14] S. Biswas, et al, *Development of linseed oil-free bakelite resistive plate chambers*, *Nucl. Instr. and Meth. A*, **604**, (2009), 310–313.

[15] F. Anulli et al., *Mechanisms affecting performance of the BaBar resistive plate chambers and searches for remediation*, *Nucl. Instr. and Meth. A*, **508**, (2003), 128.

[16] F. Anulli et al., *Performance of second generation BABAR resistive plate chambers*, *Nucl. Instr. and Meth. A*, **552**, (2005), 276-291. F. Ferroni et al., *The second generation BaBar RPCs: Final evaluation of performances*, *Nucl. Instr. and Meth. A*, **602**, (2009), 649-652.

[17] S. Biswas, et al, *Performances of linseed oil-free bakelite RPC prototypes with cosmic ray muons*, *Nucl. Instr. and Meth. A*, **602**, (2009), 749.

[18] P. Vitulo, IV International Workshop on Resistive Plate Chambers and Related Detectors, Applications in Particle Physics and Astrophysics, October 15–16, 1997, Napoli, Italy; M.Abbrescia et al., International Conference on High Energy Physics of the European Physical Society, Jerusalem, Israel, August, 1997.

[19] B. Bruno, CMS Conference Report, CMS CR-2004-001, presented at International Europhysics Conference on High Energy Physics, Aachen, Germany, July 17–23, 2003.

[20] G. Aielli, et al., *Electrical conduction properties of phenolic–melaminic laminates*, *Nucl. Instr. and Meth. A*, **533**, (2004), 86.

[21] G. Bencivenni, et al., *A glass spark counter for high rate environments*, *Nucl. Instr. and Meth. A*, **332**, (1993), 368.

[22] K. K. Meghna, et al., *Measurement of electrical properties of electrode materials for the bakelite Resistive Plate Chambers*, *JINST 7 P10003*, **2012**.

[23] P. Fonte, et al., *High-resolution RPCs for large TOF systems*, *Nucl. Instr. and Meth. A*, **449**, (2000), 295.

[24] Daniel Marlow, *Rice University Seminar*, **July 9, (1999)**, `http://www.hep.princeton.edu/~marlow/talks/rice/rice.pdf`

[25] S. Biswas, et al., *Study of timing properties of single gap high-resistive bakelite RPC*, *Nucl. Instr. and Meth. A*, **617**, (2010), 138-140.

[26] Trek Application Note, *http://www.trekinc.com/pdf/1005_Resistivity_Resistance.pdf*

[27] R. Ganai, et al., *Study of Performance of Bakelite Resistive Plate Chamber (RPC)*, *Springer Proc. Phys*, **174**, (2016), 547.

[28] R. Ganai, et al., *Fabrication and Characterization of Oil-Free Large High Pressure Laminate Resistive Plate Chamber*, *Journal of Instrumentation*, **JINST 11 P04026**, (2016).

[29] R. Ganai, et al., *Long term performance studies of large oil-free bakelite resistive plate chamber*, *Journal of Instrumentation*, **JINST 11 C09010**, (2016).

[30] Liehua Ma et. al., *The mass production and quality control of RPCs for the Daya Bay experiment*, *Nucl. Instr. and Meth.* **659**, (2011), 154-160.

Chapter 7

A Proof-of Principle for TOF-PET Imaging using MRPCs

It doesn't matter how beautiful your theory is, it doesn't matter how smart you are. If it doesn't agree with experiment, it's wrong.

Richard P. Feynman

7.1 Introduction

Positron Emission Tomography (PET)[1], [2] is a nuclear medicinal imaging technique that is used to observe metabolic processes in the body by the basic principle of detecting a pair of back to back photons created by annihilation of a positron with an electron. The concept of emission and transmission tomography was introduced by David E. Kuhl, Luke Chapman and Roy Edwards in the late 1950s. Their work later led to the design and construction of several tomographic instruments at the University of Pennsylvania. In 1975 tomographic imaging techniques were further developed by Michel Ter-Pogossian, Michael E. Phelps, Edward J. Hoffman and others at Washington University School of Medicine[3], [4]. Since then, the field of emission tomography has seen many many developments scientifically and technologically. A brief

history of PET can be found in reference [5]. PET is based on the detection of very small (picomolar) quantities of radio-pharmaceuticals labelled with positron emitting radio-nuclides like ^{11}C, ^{15}O, ^{13}N and ^{18}F. Advantages of positron labelled substances are their very high specificity (molecular targeting), the possibility of using biological active substances without changing their behaviour by the label, and fulfillment of the tracer principle. Thus, the process of interest remains unchanged during the measurement. Target structures of these molecules are e.g. glucose metabolism, receptor binding potential, catecholamine transport, amino acid transport, or protein synthesis. All the above mentioned nuclides have very short radioactive half-lives (2 min for O-15, 109 min for F-18), which necessitates a nearby cyclotron and radiochemistry facility. PET is both a medical and research tool. It is used heavily in clinical oncology (medical imaging of tumors and the search for metastases), and for clinical diagnosis of certain diffuse brain diseases such as those causing various types of dementias. PET is also an important research tool to map normal human brain and heart function, and support drug development.

Time of flight (TOF), as the name suggests, is the measurement of the time taken by an object or particle or electromagnetic or other waves to travel a certain distance through a medium. TOF technique has found several applications like TOF mass spectrometry, planar Doppler velocimetry, neutron TOF scattering and so on in various fields. It has become one of the most promising techniques for several R&D's in science in today's date. The application of TOF in PET imaging dates back to 1976 when Louis Lavoie found that the fast response and high scintillation yield of liquid xenon could be applied to PET and suggested the application of TOF in PET imaging [6] [7]. A detailed development of TOF technique for PET imaging can be found in reference [8], [9]. There has been significant development in the scintillator detectors for TOF-PET systems. The evolution of scintillating crystals like Lutetium Oxyorthosilicate, LSO and , Lutetium-Yttrium Oxyorthosilicate, LYSO crystals having good time resolution, fast and reliable PMT's along with the advancements in reconstruction algorithms have made the use of TOF a realistic and reliable choice for PET imaging. The PET imaging technique is based on the coincident detection of the two 511 keV gamma rays that are emitted in opposite directions

as a result of annihilation of a positron emitted by the administered radio tracer nuclide with an electron. The two gamma-ray interaction points define a so-called line-of-response (LOR) on which the annihilation must have taken place. A precise measurement of the arrival times of the coincident photons along with the time difference in flight-time of the two photons helps to localize the annihilation event on the LOR. Figure 7.1 illustrates the basic working and detection principle of any TOF-PET system.

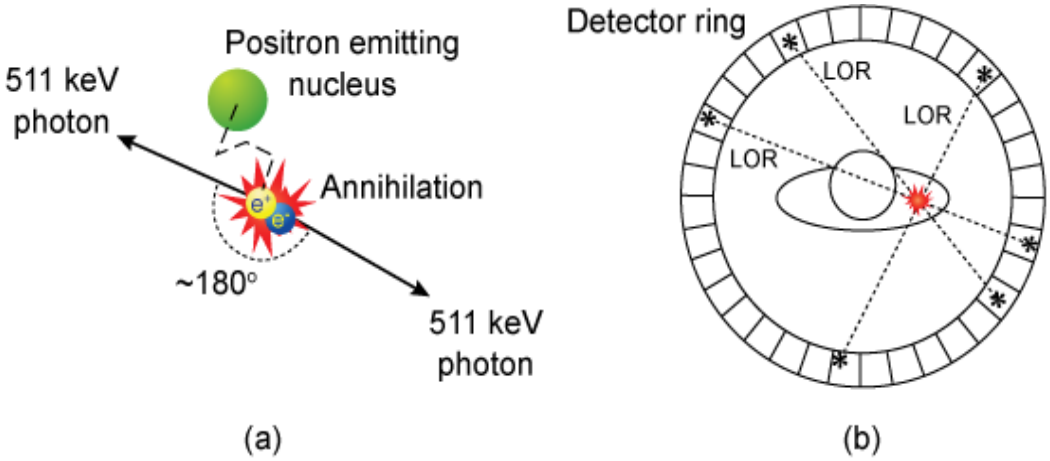

Figure 7.1: *[Colour online] Imaging principle of PET: (a) Two 511 keV photons are emitted in (almost) opposite directions after e^+ annihiliates with e^-; (b) The two photons are simultaneously detected within a ring of detectors surrounding the patient. The line-of-response (LOR) connecting the two photons is recorded. By recording many LORs the activity distribution can be tomographically reconstructed [10].*

It can be shown that the position of the annihilation along the LOR may be identified with an FWHM accuracy ΔL, given by [11]

$$\Delta L(mm) \approx \frac{\sigma_t(ps)}{2} \tag{7.1}$$

where, σ_t is the rms timing resolution of the detecting element. As seen from the equation 7.1, the better the time resolution of the detector (σ_t), the better will be the annihilation point determination. An excellent time resolution of the photon detecting system also minimizes the coincidence window ($4\sigma_t$), reducing the number of random coincidence events [12].

7.2 Development of 5 gap glass MRPCs

The detectors used in TOF-PET imaging should have time resolution in few hundreds of pico-seconds as it exploits the time difference taken by the two back to back photons created by the annihilation of electron and positron to determine the point of annihilation. The recent developments in the present detector system for TOF-PET can be found in reference [13]. MRPCs have much improved timing resolution than the present day scintillator detectors used in PET systems. Over the past several years, there has been attempts to develop RPC or MRPC based PET systems [14], [15], [16]. The advantages of using RPCs or MRPCs to develop a PET system are as follows [17]

- The MRPCs have excellent time resolution ($\sim$20 pico-seconds for charged particles [18] and $\sim$90 pico-seconds for 511 keV photon pairs [11]) which may result into better determination of the annihilation point than the scintillators.
- For the case of RPC-PET, a position resolution in sub-millimeter region is achievable [15] which may result into better determination of the Line Of Response (LOR).
- RPC's and MRPC's are unaffected by magnetic fields, hence they are compatible with Magnetic Resonance Imaging (MRI) whereas the presence of PMTs in scintillator systems makes them unfit for MRI.
- The fabrication of an MRPC is inexpensive and simpler than the scintillators. Hence, development of large-sized MRPC detectors is quite feasible and the Field-Of-View attainable with RPC's or MRPC's comes at a much lower cost compared to existing crystal based systems.
- MRPC's have naturally layered structure which is suited to photon conversion based on the converter-plate principle [19].
- The particle detection efficiency increases and the time resolution of the MRPCs improve with the increase in the applied high voltage. The applied high voltage has to be optimized

for a good detection efficiency with proper time resolution.

Apart from the above mentioned advantages of RPC or MRPC based PET systems over the present day scintillator based PET system, there are limitations. The major limitation being the **conversion efficiency** of the RPC or MRPC which is defined as the number of 511 keV γ's converted to the original number of γ's incident on the detector. Being a gaseous detector, RPC's or MRPC's have very good charged particle detection efficiency but have much lower photon detection efficiency than that of the scintillators[16]. Hence, to develop a MRPC based PET system, it is a major challenge to increase the photon detection efficiency. In spite of the above fact, the choice of MRPC for TOF-PET imaging seems to be the practical choice for the future as the current existing scintillator-based technology is very expensive increasing the per-scan cost. In order to study the feasibility of using MRPCs in TOF-PET, two identical 5-gap glass MRPCs (Yellow MRPC or MRPC - I and Green MRPC or MRPC - II) have been developed. The details of the development process has been discussed in section 3.7.7 of reference [17]. Figure 7.2 shows the photograph of the two MRPCs developed for the TOF-PET imaging application. Table 5.7 gives a brief summary about the two prototype MRPCs for TOF-PET.

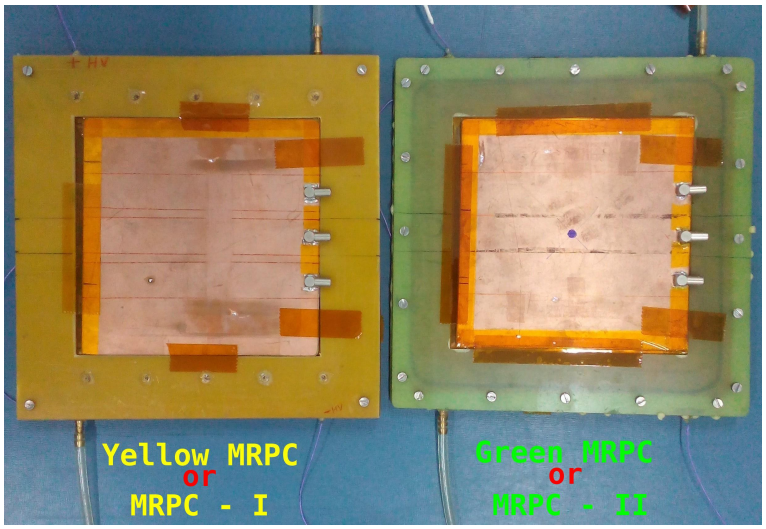

Figure 7.2: *[Colour online] Two identical prototype of 5-gap glass MRPCs with pick up panels developed for TOF-PET imaging.*

MRPC parameters	Yellow MRPC	Green MRPC
Dimension	18 cm × 18 cm	18 cm × 18 cm
Total number of gas gaps	5	5
Electrode thickness	700 μm	700 μm
Each gas gap thickness	250 μm	250 μm
Mean of surface resistivity of top painted electrode surface	∼1.5 MΩ/□	∼0.8 MΩ/□
Mean of surface resistivity of bottom painted electrode surface	∼1.0 MΩ/□	∼0.7 MΩ/□

Table 7.1: *Specifications of the prototype MRPCs. In this thesis, Yellow MRPC has been tagged as MRPC - I and Green MRPC as MRPC - II.*

Both the prototypes have been operated and tested with a gas mixture of Freon (R134a) : Isobutane :: 95 : 5 (by volume), in the avalanche mode. The I-V characteristics and the variation of time resolution with applied high voltage have been studied for the prototypes. The I-V characteristics of Yellow and Green MRPC has been shown in Figure 7.3 and 7.4 respectively. Both the graphs show two distinct slopes with breakdown voltages at 13,000 kV and ∼12,000 kV respectively. The time resolution of the detector is very important to study the feasibility of the same for TOF-PET imaging. Hence, the variation of the time resolution with the applied high voltage was also studied for both the MRPCs. The method followed for the study has been well described in reference [20] and also in section 6.3.3 of this thesis.

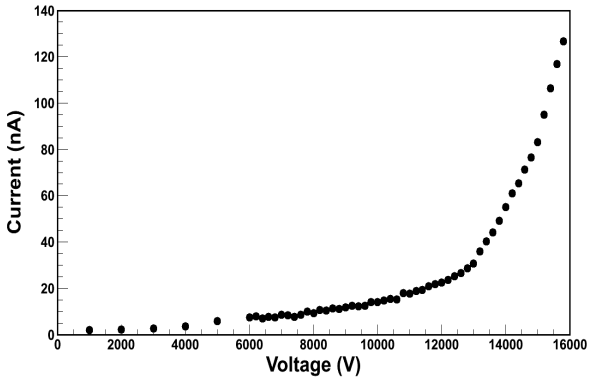

Figure 7.3: *[Colour online] I-V characteristics of Yellow MRPC or MRPC - I.*

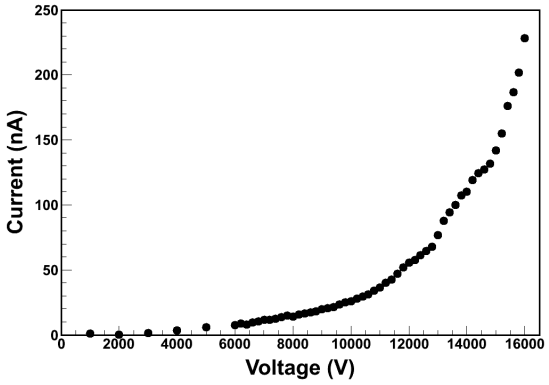

Figure 7.4: *[Colour online] I-V characteristics of Green MRPC or MRPC - II.*

The time resolutions have been measured by a 16 channel PHILIPS SCIENTIFIC 7186 TDC module with scintillator 3-fold as TDC-Start and delayed MRPC logic pulse as TDC-Stop. Figure 7.5 and 7.7 shows the study of time resolution variation with applied high voltage for Yellow MRPC or MRPC - I and Green MRPC or MRPC - II respectively. From both the figures, it can be concluded that the best time resolution obtained for Yellow MRPC is ∼100 ps at 15,800 kV and ∼230 ps at 15,800 kV for the Green MRPC. The values of the time resolution reported in Figure 7.5 and 7.7 have been corrected for the scintillator contributions. Figure 7.6 and 7.8 shows the raw uncorrected TDC spectra of the MRPCs fitted with Gaussian function.

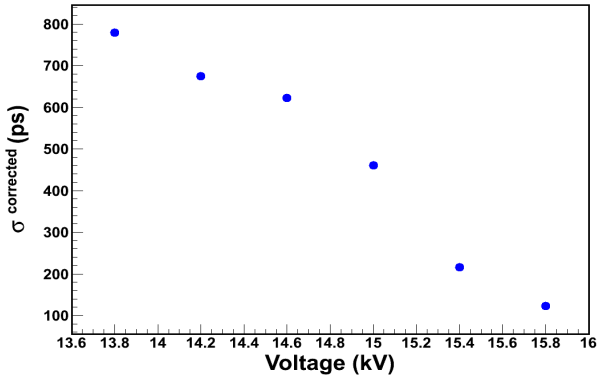

Figure 7.5: *[Colour online] The variation of time resolution of the Yellow MRPC or MRPC-I with applied high voltage. The error bars are within the marker size.*

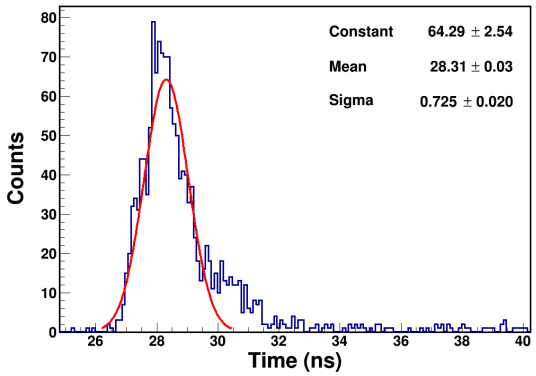

Figure 7.6: *[Colour online] The time resolution spectra of the Yellow MRPC or MRPC-I at 15.8 kV.*

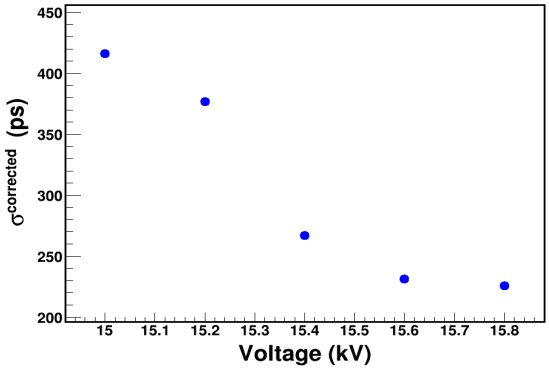

Figure 7.7: *[Colour online] The variation of time resolution of the Green MRPC or MRPC-II with applied high voltage. The error bars are within the marker size.*

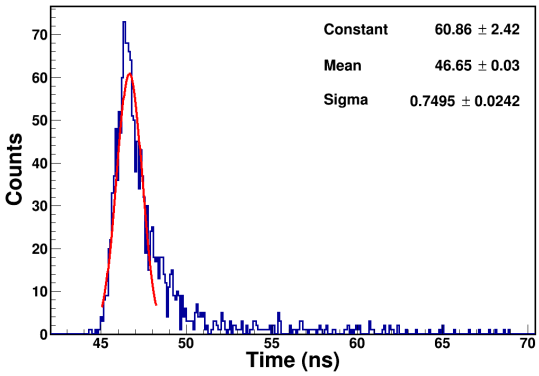

Figure 7.8: *[Colour online] The time resolution spectra of the Green MRPC or MRPC-II at 15.8 kV.*

Encouraged from the time resolution values of both the prototype 5-gap glass MRPCs, a preliminary test to establish the basic proof of principle for TOF-PET imaging with these MPRCs has been performed. The following sections discusses about the experimental set up and test results in details.

7.3 Experimental set-up and test results

In present days, for PET imaging, positron emitting radio nuclides like ^{11}C, ^{15}O, ^{13}N and ^{18}F are used. these radio nuclides have a very short radioactive half lives. For the experiment presented here ^{22}Na was used. ^{22}Na is a β^+ or positron emitter but with a half life of $\sim$2.6 years. It emits positrons with maximum energy of 0.545 MeV accompanied by photons of energy 1.275 MeV. These positrons annihilate immediately with nearby electrons, giving two back to back photons or gammas each of energy 0.511 MeV. The details of the decay scheme of ^{22}Na can be found in reference [21]. The aim was to detect these two back to back gammas with the prototype MRPCs and also to sense a change in the position of the ^{22}Na source. In order to do so, the major challenge was to eliminate the cosmic muon background as MRPCs are known to have very good charged particle detection efficiency and was successfully achieved by **veto** method described as follows.

The two prototype MRPCs were kept horizontally and separated by a known distance as shown schematically in Figure 7.9. One $\sim$ (30 cm $\times$ 30 cm $\times$ 0.5 cm) Aluminium plate was placed on the top of the top MRPC and a second Aluminium sheet of nearly similar dimension was placed at the bottom of the bottom MRPC, covering both the MRPCs completely. Two plastic scintillators each of dimension $\sim$ 50 cm $\times$ 25 cm were also used. Scintillator-I was placed at the top of the top aluminium sheet and scintillator-II was placed at the bottom of the bottom sheet. The ^{22}Na source was placed in between the two MRPCs. For the experiment, the distance between the two prototype MRPCs was kept 17 cm and the source was moved by a distance of 11 cm. The first set of TDC spectra was taken when the source was placed 3 cm away from the bottom or MRPC - II and the second set was taken when the source was kept at 14 cm away

from the bottom MRPC. The actual experimental set up has been shown in Figure 7.10.

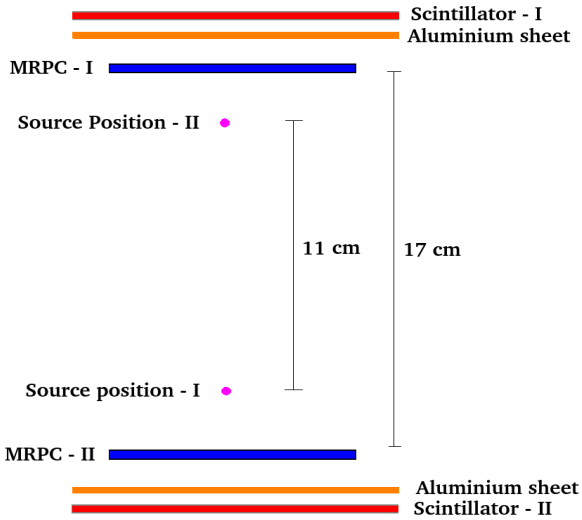

Figure 7.9: *[Colour online] Schematic of the experimental set up for TOF-PET with prototype MRPCs.*

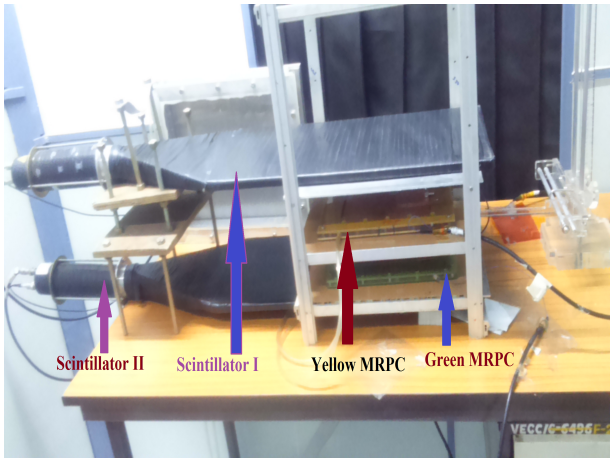

Figure 7.10: *[Colour online] Actual experimental set up for TOF-PET with prototype MRPCs .*

The Aluminium sheets placed between the scintillators and the MRPCs ensured that the back to back photons does not reach the scintillators as scintillators have good detection efficiency for cosmic muons as well as photons. Hence, a suitable choice of the trigger may help to eliminate the cosmic muon background as the interest is to collect the photon events detected by the MRPCs

in coincidence. The chosen trigger will initiate the START of the TDC module. Figure 7.11 shows the electronic block diagram of the set up. The idea behind the trigger to be chosen is the presence of MRPC - I signal when the coincidence of both scintillators is absent. Hence, the presence of a digital ($\overline{(Scintillator-I)\cdot(Scintillator-II)}\cdot$ MRPC - I) logic signal formed the trigger. To ensure this, CAEN N93B dual timer module was used. The coincidence of the scintillators goes to the VETO and the digital output of MRPC - I goes to the INPUT of the dual timer. The OUTPUT of the dual timer generates the trigger and goes to the START of the TDC module. Delayed MRPC - II digital signal then goes to the STOP of the TDC.

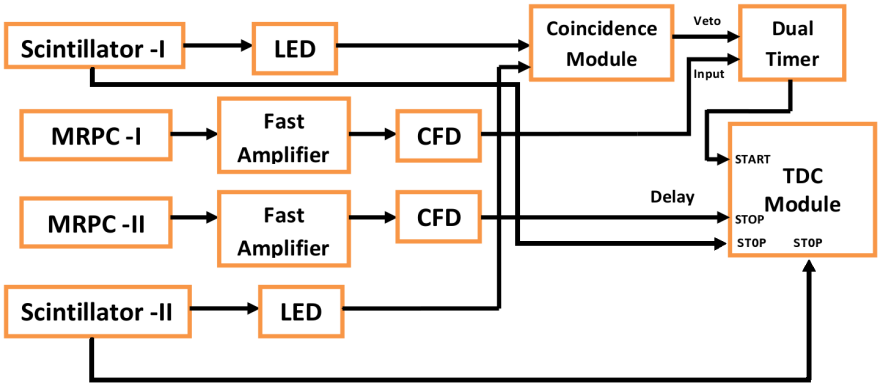

Figure 7.11: *[Colour online] The block diagram of the experimental trigger and time measurement logic.*

As none of the detectors (scintillators and MRPCs) are 100% efficient to detect the cosmic muons, the digital signals of the individual scintillators were also sent to separate STOP channels of the TDC module. This helped to eliminate those cosmic muons which were missed by both the scintillators but were detected by MRPC - I. After selecting the suitable trigger scheme, the ^{22}Na source were kept in positions I and II as shown in Figure 7.9 and the data set were recorded for both the positions. From the event by event timing information, those events which have hits in either of the scintillators have been rejected while analyzing the data set. Figure 7.12 and 7.13 show the TDC spectra of MRPC-II when the source was kept at position-I and position-II

respectively.

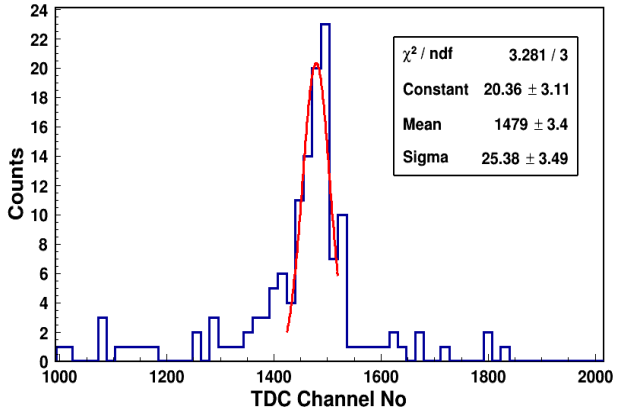

Figure 7.12: *[Colour online] The TDC spectra of MRPC-II when the ^{22}Na source was kept at position-I as shown in Figure 7.9. X axis is the TDC channel number. The resolution of TDC is ∼24.4 ps / channel.*

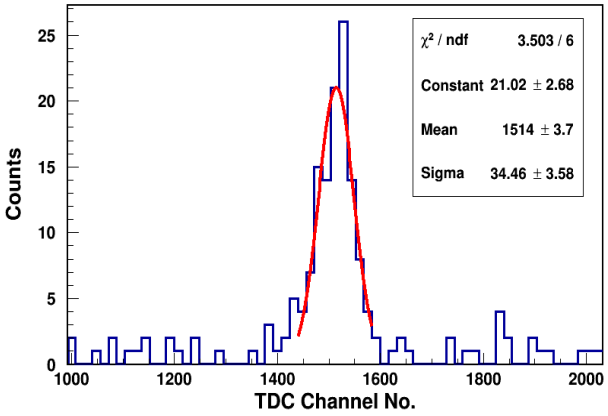

Figure 7.13: *[Colour online] The TDC spectra of MRPC-II when the ^{22}Na source was kept at position-II as shown in Figure 7.9. X axis is the TDC channel number. The resolution of TDC is ∼24.4 ps / channel.*

The mean channel of the TDC spectra after a Gaussian fit was obtained to be 1479 for Figure 7.12 and 1514 for Figure 7.13. Clearly there is a shift in the mean of the TDC spectra, specially in the mean of the spectra by 35 TDC channels as the source was moved from position-I to position-II by 11 cm. Assuming the velocity of photons to be ∼30 cm/ns, a change in source

position by 11 cm should give TDC channel difference of ∼30 channels which is close to to the obtained value of 35 channels. From another way of looking at it, a shift in the mean of the TDC spectra of 35 channels should yield a change in the source position by ∼ 12.8 cm which is close to the actual change in source position by 11 cm.

7.4 Summary

MRPCs are known to have excellent time resolution. Hence, they can be a potential candidate to replace the scintillators in existing PET systems. It is also expected that MRPCs may give more precise results in comparison to scintillator based PET system as they have better time resolution than scintillators. If successful, the cost per scan of PET imaging will reduce drastically as MRPCs are relatively low cost detectors. As a first step towards this noble work, we have successfully developed two 5-gap glass MRPCs with time resolution ∼100 pico-seconds and ∼230 pico-seconds (without time-walk correction) respectively. These MRPCs have been operated in avalanche mode of operation. We have tested these two MRPCs in a two-MRPC coincidence set-up for the detection of back to back photons created by the anhiliation of positron (emitted from Na^{22} source) with a nearby electron. The change in distance in the source position was succesfully estimated from the time spectra obtained by using both the MRPCs.

Bibliography

[1] Sorenson J. A, and Phelps M. E, *Physics in Nuclear Medicine*, *2nd Edition, Orlando, Grune and Stratton Inc.*, **1987**.

[2] Ter-Pogossian M. M et. al., *Positron Emission Tomography*, *Scientific American*, **243**, (1980), 170 - 181.

[3] Ter-Pogossian M. M et. al., *A positron-emission transaxial tomograph for nuclear imaging (PET)*, *Radiology*, **114**, (1975), 89 - 98.

[4] Phelps M. E et. al., *Application of annihilation coincidence detection to transaxial reconstruction tomography*, *Journal of Nuclear Medicine*, **16 (3)**, (1975), 210 - 224.

[5] Dayton A. Rich, *A Brief History of Positron Emission Tomography*, *Journal of Nuclear Medicine Technology*, **25**, (1997), 1.

[6] Louis Lavoie, *Liquid xenon scintillators for imaging of positron emitters*, *Medical Physics*, **3**, (1976), 283.

[7] Doke T. et. al., *Time-of-flight positron emission tomography using liquid xenon scintillation*, *Nucl. Instr. and Meth. A*, **569**, (2006), 863-871.

[8] Lewellen Tom K, *Time-of-Flight PET*, *Semin Nucl Med*, **23 (3)**, (1998), 268-275.

[9] Moses W. W, *Time of flight in PET revisited*, *IEEE Trans Nucl Sci*, **50 (5)**, (2003), 1325-1330.

[10] `https://www.tudelft.nl/en/faculty-of-applied-sciences/about-faculty/departments/radiation-science-technology/denkova-group/research/tof-pet/`

[11] Blanco A, *Perspectives for positron emission tomography with RPCs,Nucl. Instr. and Meth. A*, **508**, (2003), 88.

[12] PhD thesis of Maria Monica Necchi, *Resistive Plate Chambers: from high energy physics to biomedical applications*, **University of Pavia, Italy**, *2008.*

[13] Vandenberghe S. et. al.,, *Recent developments in time-of-flight PET*, *EJNMMI Phys*, **3**, (2016), 3.

[14] G. Georgiev et. al., *Multigap RPC for PET : development and optimization of the detector design* , *Journal of Instrumentation*, **JINST 8 P01011**, (2013).

[15] Blanco A. et. al., *RPC-PET: A New Very High Resolution PET Technology*, *IEEE Transactions on Nuclear Science*, **53**, (2006), 5.

[16] Belli G. et. al., *RPC: From High Energy Physics to Positron Emission Tomography*, *Journal of Physics : Conference series*, **41**, (2006), 555.

[17] PhD thesis of Arindam Roy, *Probing matter created at RHIC heavy-ion collisions by di-muons and photons at mid and forward rapidities.*, **Homi Bhabha National Institute**, *January, 2016.*

[18] Williams M. C. S, *A 20 ps timing device - A Multigap Resistive Plate Chamber with 24 gas gaps,Nucl. Instr. and Meth. A*, **594**, (2008), 39.

[19] Bateman J. E, *X-ray and gamma imaging with multiwire proportional counters,Nucl. Instr. and Meth. A*, **221**, (1984), 131.

[20] R. Ganai, et al., *Fabrication and Characterisation of Oil-Free Large High Pressure Laminate Resistive Plate Chamber*, *Journal of Instrumentation*, **JINST 11 P04026**, (2016).

[21] **http://www.nucleide.org/DDEP_WG/Nuclides/Na-22_tables.pdf**

Chapter 8

Summary and Outlook

8.1 Summary

Neutrinos are strange particles - small but fascinating. They are very much abundant in the universe but elusive as they are very weakly interacting. There are several experiments like Super-Kamiokande, Daya Bay, Ice Cube and so on studying various properties of neutrinos like neutrino oscillations, mass determination and so on. The neutrino physics community in India has taken an initiative to study the neutrino oscillations in the atmospheric sector. INO is an upcoming facility in south of India which will house several experiments like ICAL, NDBD, DINO to study the properties of neutrinos. ICAL, which will be a $\sim$50 kt mangenized detector with RPCs as active detectors, will look for the true mass hierarchy by studying the Earth matter effects experienced by the neutrinos and the antineutrinos separately. ICAL will also contribute in the precise measurement of θ_{23} and $|\Delta m^2_{31}|$ and will look for new physics.

Primarily, ICAL will measure the momentum and direction of the muons produced by the interactions of the incoming atmospheric neutrinos with the iron present in the ICAL. The magnetization of the iron plates and the timing information provided by the RPCs in different layers will help to separate between up-coming and down-going neutrinos and anti-neutrinos. The oscillations in the up-coming atmospheric neutrinos will be more as compared to the down-

going ones as the former will experience matter effects due to the earth enhancing the oscillation. Studying the oscillation of the up-coming neutrinos with respect to the down-going neutrinos as a function of $log[L(km)/E(GeV)]$ proved to be a good tool to probe the density profile of the inner structure of the earth, specially the core of the earth. A model based study by changing the density of the core of the earth, with $Up/Down$ ratio as a function of $log(L/E)$ as an observable has been performed to learn the deviation in the density of the core of the earth from the standard PREM.

RPCs have been chosen as the active detectors in the ICAL experiment because they have a time resolution $\sim$1 nano-second and position resolution $\sim$1 cm. The R&D program for the ICAL is now running at a full pace. As a part of this programme, a large sized single gap oil-free bakelite RPC of dimension 240 cm $\times$ 120 cm with a gas gap of 0.2 cm has been successfully developed. The RPC has been tested in streamer mode of operation in a gas mixture of Argon:Freon:iso-butane::34:57:9 (by volume) for its efficiency, noise rate, time resolution and its long term performances with cosmic rays. Before developing the RPC, several bakelite samples were tested for their bulk and surface resistivities and small prototypes were developed with those. Among them, the suitable sample was chosen and a small (30 cm $\times$ 30 cm) single gap prototype RPC with a gas gap of 0.2 cm was developed successfully. The prototype was also tested for its efficiency and noise rate in streamer mode of operation in a gas mixture of Argon:Freon:iso-butane::55:40:5 (by volume).

Gas detectors like MRPCs may find potential applications in the field of medical physics like PET imaging. Excellent time resolution, low development cost per unit area, robust in nature, easy to operate make the MRPCs a suitable canditate to replace the scintillators in the present day PET imaging systems. In order to establish the basic principle of PET imaging using TOF technique, two nearly identcal 5-gap glass MRPCs have been developed. The I-V characteristics and time resolution of these detectors have been studied in avalanche mode of operation in a gas mixture of Freon:iso-butane::95:5 (by volume) with cosmic rays in a standard set-up. The MRPCs have been used to detect the back to back photons created by the anhiliation of positron

emitted from Na^{22} source with a nearby electron. A change in distance in the source position was succesfully estimated from the time spectra obtained by using both the MRPCs, hence extablishing the principle of TOF-PET imaging.

8.2 Outlook

This thesis work provides quite a few attractive future scopes. The ability of ICAL to probe the inner matter density profile of the earth using atmospheric neutrino oscillations is very unique. In our model based study of the density profile of the earth, the δ_{CP} was taken to be zero along with the ϑ_{23} value to be 45.0°. More precise values of the oscillation parameters along with improved ICAL detector parametrs like direction resolution, energy resolution, charge identification efficiency, detection efficiency and so on will improve the model significantly. The idea of studying the matter density profile of the earth using the oscillation dips may prove to be more fruitful for very long baseline (∼10000 km) experiments using ICAL. This may also help in studying the non-standard interaction of the neutrinos with matter.

From the detector development for ICAL experiment part, the variation of time resoution over the entire RPC surface and with the surface resistance profile will be an interesting area to study. Very long term performance of the oil-free RPC should also be studied in order to get an idea that how long it can perform without any degradation. The performance of the RPC in avalanche mode of operation can also be studied. The variation of its performance with different gas mixing ratios will be an interesting fact to look into. The RPC should also be tested with proper electronics developed for RPCs in ICAL experiment.

The MRPC detectors have shown good time resolution and the proof-of-principle for TOF-PET imaging have been successfully established. The time resolution can be improved further by changing and optimising the gas mixture in order to narrow down the location of the anhiliation point. The LOR has to be identified accurately. A proper MRPC based TOF-PET imaging system has to be developed.